NUMERICAL MODELING OF THE POWER CYLINDER SYSTEM FOR INTERNAL COMBUSTION ENGINE WITH AN EMPHASIS ON RING PACK DESIGN

By

Chao Cheng

A DISSERTATION

Submitted to
Michigan State University
in partial fulfillment of the requirements
for the degree of

Mechanical Engineering – Doctor of Philosophy

2014

ABSTRACT

NUMERICAL MODELING OF THE POWER CYLINDER SYSTEM FOR INTERNAL COMBUSTION ENGINE WITH AN EMPHASIS ON RING PACK DESIGN

By

Chao Cheng

Modeling the piston ring behavior is crucial for the engine power cylinder system. The dynamic and thermal characteristics directly affect engine performance, e.g. frintion loss, wear, blowby loss, etc. This dissertation describes a numerical model of the power cylinder system focusing on the ring pack design.

A three-dimensional piston ring model is developed using finite element method. The model predicts the piston ring conformability with the cylinder wall as well as the separation gap between the interfaces. In addition, the ring model also predicts the interaction between the ring and piston groove sides. This means, the ring axial lift, twist, contact with the groove sides along the circumferential direction are all calculated simultaneously with the radial conformability prediction.

The numerical model is then verified through experiment measurement. This validation includes a ring tension force measurement as well as a light-tightness measurement. Good agreement has been found between the measured and calculated result.

Thermal load is believed having significant influence on the ring pack performance, especially for the top compression ring, which is under the most severe operating condition. The thermal load influences are included in the model. In addition, a new lubrication model is implemented to the existing model with the consideration of flow factor for the ring pack lubrication and tribology analysis.

A simulation study of the second ring dynamics for a modern diesel engine is presented. Two phenomena are focused for this study, one is the second ring fluttering and the other is ring collapse. Both these phenomena are closely related to gas dynamics and could result in engine blowby increase. The mechanism and the conditions at which these phenomena occur are given. The second ring dynamic behavior over an engine cycle is then studied considering 3D effect. The contact forces, in both radial and axial directions, and the twist angles can be found at each engine crank angle.

The piston ring model provides the geometry for three-dimensional gas dynamics analysis. In addition to the gas flow paths that the current two-dimensional models predict, including through the ring end gap, through the ring-groove sides as ring flutters, through the ring front face when ring radially collapses, gas can flow through an additional path across the ring. This gas flow path is formed due to the variance of ring axial displacements along the circumference. The variant lift occurs for rings with asymmetric cross-sections. Even for rings with symmetric cross-section, the ring can also undergo different circumferential lift due to influences like piston secondary motion. When this different circumferential lift occurs, gas can flow from the piston land above the ring, through the crevice between the ring-groove sides, to the volume behind the ring for the ring segment that stays bottom seated. The gas can travel circumferentially through the volume behind the ring, until a point that the ring segments lift and stay top seated against the groove top side. Then the gas can flow from the volume behind the ring, through the crevice between the ring-groove bottom sides, to the piston land below the ring.

To my parents, Shulin and Liqin.
To my wife, Mengyang.

ACKNOWLEDGEMENTS

First, I would like to thank my advisor, Dr. Harold Schock. It is my great honor to work with Dr. Schock at the Energy and Automotive Research Lab at Michigan State University. Dr. Schock has always been supportive and patient with me, providing invaluable motivations through my research. His faith and encouragement have helped me overcome the difficulties during my graduate study.

I would also like to thank Dr. Guoming Zhu, Dr. Elisa Toulson and Dr. Dennis Miller for serving as my committee members of my thesis defence. I would like to express my special thanks to Dr. Zhu for his encouragement and discussions on my research as well as my graduate life. Dr. Toulson and Dr. Miller also deserve special recognitions for their insightful suggestions to improve my research.

I was very fortunate to have the opportunity to work with Mr. Mulyanto Poort from Rescale and Dr. Dan Richardson from Cummins. Mulyanto Poort has helped me get familiar with power cylinder modeling and provided numerous invaluable suggestions for my research. Dr. Dan Richardson has provided numerous supports and invaluable advises on my research that will benefit for my entire career.

It is not possible to complete my research without the support from my friends and colleagues: Dr. Andrew Huijsen, Ali Kharazmi, Ravi Vedula, CJ Maines, Ati Sedigheh Tolou, Nariman Mansouri, James Holly JR., Jenny Higel, Jeff Higel, Tom Stuecken, Brian Rowley, Trevor Ruckle. They have made the lab a fun place to work, especially Ali, whose discussion on the model and the post-processing of the result is highly appreciated. I would like to express my special thanks to Tom, Brian and Trevor for helping me set up the experiment.

I would also thank my friend, Dr. Xiankai Song, for the discussions and so many invaluable suggestions on my numerical modeling.

Finally, I would like to thank and express my gratitude to my wife Mengyang and to my parents, Shulin and Liqin. Although we have been spending considerable amount of time on the two sides of the earth, they are always there, loving, supporting, and being patient with me.

TABLE OF CONTENTS

LIST OF TABLES

LIST OF FIGURES

Chapter 1 NUMERICAL MODELING OF ENGINE POWER CYLINDER SYSTEM

1.1 Motivation

As the reserved crude oil becomes less and less and more tighten emission regulations have been issued by the government over the years, producing an internal combustion engine with great fuel efficiency and low emission without losing its durability and comfortability becomes vital for any automakers to survive nowadays. Computer modeling has proven a powerful way in engine design that considers all the above factors for the automakers because it is rapid and cheap compared with prototypes. Besides, the computer model can also provide valuable data that is not possible to be measured.

The internal combustion engine has been existing for more than a hundred years. However, its physics has not been yet fully understood as the cyclic behavior represents very complex processes as combustion, thermodynamics, heat transfer, dynamics, solid mechanics, fluid mechanics, tribology, et al are all involved simultaneously over engine cycle in a very short time period.

The reciprocating engine power cylinder system consists of piston, ring pack, cylinder bore and cylinder head. The primary function of the piston is to transfer the thermal energy from the combusted gas into mechanical energy that drives the vehicle. The combustion of the gas/air mixture occurs in the combustion chamber which is comprised of the piston head, cylinder bore and the cylinder head. The main purpose of the ring pack is to seal the combustion chamber that prevents gas leaking into the crankcase. In addition, the ring pack also controls the lubrication oil distribution between the rings and the cylinder wall. On one hand, it is desired to have lubrication oil evenly distributed along the circumferential direction between the paths that the piston travels; on the other hand, it is also critical to prevent the oil traveling into the combustion chamber, which may result in severe oil consumption and emission problems.

It is believed that the piston and ring pack together account for as high as 35% of the entire engine mechanical loss. Excessive mechanical loss means not only lower engine efficiency; but also shorter engine lift. In addition, engine emission is also closely related to the piston ring sealing ability. Thus, the piston and piston ring pack are important factors regarding to engine performance.

This focus of the dissertation is the engine power cylinder system modeling with an emphasis on the piston ring pack. A three-dimensional piston ring model is built with finite element method, evaluating the ring deformation and constraint loads in both static and dynamic conditions.

1.2 Objective

As discussed in the previous section, the two major factors driving the modern engine development are the fuel efficiency and engine pollutant emission, which are directly affected by friction, blowby loss and lubrication oil consumption. These factors are directly associated with the performance of the engine ring pack. Thus a thorough understanding of the ring pack behavior is crucial for designing an engine that meets all the requirements.

The existing two dimensional (2D) numerical models of the ring pack are proven to be useful qualitatively. However, the 2D model is limited in providing detailed result as the complex processes are believed to be three-dimensional (3D) phenomena.

Friction occurs between the ring front face and the cylinder liner as the two sliding surfaces have relative movement. Although lubricant oil is provided for the ring pack to reduce the friction, it cannot be eliminated. The friction varies ring to ring, crank angle to crank angle, and also along the circumferential direction due to the non-evenly distributed ring-cylinder bore contact pressure. The cylinder bore distortion due to mechanical bolting and thermal load is another source that makes the ring-cylinder bore interaction a more complex 3D problem.

Wear is generated between the ring front face and the cylinder bore due to the contact and sliding motion. Because of this wear, the piston rings change their geometries as the engine is running, especially during the engine break-in. The change in ring geometries can affect the friction, as well as the sealing capacity of the ring. Thus this needs to be considered for the computational model.

Blowby refers to the gas flowing from the combustion chamber past the ring pack into the crankcase. One of the major gas paths is the ring end gap. However, if the ring front face loses contact with the cylinder bore, a direct path is formed thus a sharp increment in blowby can be found. Besides, as the piston rings moves up and down in the piston grooves, the gas also travels behind the rings. The gas dynamics is highly coupled with the ring dynamics, which is influenced by the piston secondary motion.

All these phenomena mentioned above demand a 3D ring pack model that can provide better understanding of the processes and practical suggestions in design.

1.3 Previous efforts

Numerical models have been widely used to understand the complex phenomena of the internal combustion engine and improve it during its over 100 years' history. The numerical models include variant disciplines: combustion, fluid dynamics, heat transfer, solid mechanics, dynamics, tribology, etc. All these models need to be solved simultaneously in order to obtain high fidelity results.

1.3.1 Piston

In order to model the ring pack behaviors, the piston motion and dynamics are necessity as the compression rings and oil control ring are nested in the piston groove. Over the years, several piston dynamics models were built.

Panayi developed a finite element analysis code that simulates piston dynamics, with the consideration of piston deformation under gas pressure, thermal load, body load and elastohydrodynamic load [1, 2]. Piston secondary motions, including the motion along the wrist pin and piston tilt, are predicted by the code. The model also simulates the lubrication and friction between the piston skirt and the cylinder wall along the piston periphery. Piston skirt wear can also be obtained over one engine cycle.

PISDYN is a similar package for piston dynamics analysis developed by Ricardo [3]. Wong, V., Tian, T., et al., presented a model that calculates piston behavior and the impact force on the cylinder liner which is believed as the source of piston slap excitation [4]. Keribar described a comprehensive piston skirt lubrication model, which is used in parallel with a piston secondary dynamic analyzer to characterize the lubrication oil film's influence on piston motions [5].

Piston skirt lubrication behavior is also investigated by Kim, et al[6], and Malagi, et al[7]. Kageyama, et al, developed an experimental method to measure the piston skirt contact with the cylinder liner and the skirt deformation [8]. First, the relationship between the skirt contact pressure, skirt deformation and the skirt inner strain was determined statically. Then the skirt dynamic contact pressure and the skirt deformation were obtained known the skirt inner strain. Patel, et al, developed a piston secondary dynamics model with an emphasis on the piston to cylinder bore contact [9]. The influences of engine speed, in-cylinder peak pressure timing, nominal piston to cylinder bore cold clearance and the piston pin offset were studied for the piston to bore contact. Taylor, et al[10], measured piston secondary motion and piston temperature from experiment.

1.3.2 Ring pack

Along with the piston dynamics model developments, the modeling of ring pack is also vastly investigated. Coupled with the gas dynamics, constrained by the piston groove and the cylinder wall, the ring pack dynamics become a very complex problem. Several numerical models have been proven predicting the ring dynamics and gas dynamics well [11-15].

CASE-RING [16] is a code for ring pack evaluation and analysis developed by Mid-Michigan Research LLC. The CASE-RING is used for ring pack dynamics, including the ring axial motion, radial motion as well as twist. The code also predicts tribological phenomena between the rings and their interacting counterparts. Both hydrodynamic friction and asperity friction can be obtained. Ring face/cylinder wall wear and the ring/groove sides wear are then found using the wear model. Starved lubrication for the top ring is considered when the lubrication oil is not supplied enough due to oil evaporation. In addition, progressive wear between the ring/cylinder wall and the ring/groove sides are obtained in a progressive and adaptive manner, which is the material removed is considered and the ring is resurfaced gradually during engine operation.

Ejakov simulated the ring pack kinematics and gas dynamics for a deactivated cylinder [17]. The GESIM software was used to model the in-cylinder pressure trace for every cycle considering heat transfer losses and the RING program was used for ring pack kinematics and gas dynamics analysis. The influences of the inter-ring gas pressures and the ring dynamics on engine blowby were then studied since engine blowby is an important factor determining engine efficiency. Furthermore, Ejakov also modeled the three-dimensional ring twist in the piston grooves using space beam elements [18]. The gas flow areas above and below the rings were then obtained for gas dynamics analysis. Associated with ring dynamics, engine blowby is recognized as the gas leaking from the combustion chamber into the crankcase. The engine blowby has been modeled and studied by several researchers [12-14, 19-21].

Liu, et al, developed a three-dimensional (3D) finite beam element ring model for static analysis [22]. The ring/cylinder wall and ring/groove conformabilities were calculated; cylinder bore distortion was considered as well as the ring lapping process. The model assumes half of the piston ring assuming the ring is symmetric about the ring back (opposite to the ring end gap). In addition, Liu also modeled the ring pack dynamics and the gas flow based on the same 3D ring model [23, 24]. A heavy-duty diesel engine was then simulated using the model and variance along the ring circumference was regarding the ring motion and gas flow. Tomanik, et al, [25] built a ring contact force measurement rig and showed similar contact force distribution with the simulation result from Liu [22]. In addition, other ring pack performances were also investigated by Tomanik, including ring conformability to distorted bore, piston ring and ring groove wear as well as a new criterion for ring conformability [26-30].

Ma, et al, computed the piston ring contact force distribution with three different numerical constraint models: gap element, cable element and thermal liner element models [31]. Sun modeled the piston ring and cylinder bore contact based on thermal elastic theory, with the assumption that the ring deflection only takes place at the ring plane and the non-uniform temperature distribution on the ring is neglected [32]. Tejada, et al, showed different ring pack configurations' impacts on oil consumption and engine blowby [33]. The ring dynamics model was adopted for ring/groove wear and ring/cylinder wall wear for a diesel engine by Tian, et al, [13]. The results showed that the worn top ring face profile could scrape up oil on the cylinder wall into the combustion chamber due to the ring dynamic twist and the piston tilt. Chui modeled the elastohydrodynamic lubrication for the ring pack to evaluate its tribological performance [34, 35]. In his model, oil consumption is considered due to evaporation, which is also considered by De Petris [11, 36]. Thus, the top ring is not always in the fully flooded lubrication condition. As a result, starved lubrication could occur for the top ring depending on the operation condition. Other ring pack models also consider oil consumption [15, 37-40].

1.4 Dissertation structure

This dissertation is organized as follows. An overview of the engine power cylinder system is given in Chapter 2. This includes the main components of the power cylinder system and their functions. A 3D finite element model of the piston rings is then presented in Chapter 3. The ring-cylinder wall contact and ring-groove contact analysis is summarized. Thermal load influence on piston rings is discussed in Chapter 4. . In Chapter 5, the lubrication, friction and wear models are shown between the contacting components with examples given. Chapter 6 presents an experimental test to measure the ring-cylinder wall contact pressure/force and the test results are used to validate the numerical model. Simulation analysis of the ring dynamics and the tribological results are discussed in Chapter 7. This includes a second ring dynamic analysis using conventional 2D model as well as a novel 3D simulation study of a scraper ring under dynamic load condition. The dissertation is then concluded in Chapter 8 where the limitations and recommendations for future work are pointed out.

Chapter 2 ENGINE POWER CYLINDER SYSTEM

2.1 Introduction

The internal combustion engine converts thermal energy of the combustible fuel into mechanical energy that moves the piston and eventually the crankshaft. This energy conversion process occurs within the engine power cylinder system. The power cylinder system comprises the following components: piston, piston rings, cylinder liner, wrist pin and connecting rod. The piston is the main component that delivers the mechanical energy through reciprocating motion. And this reciprocating motion is transmitted into rotational motion of the crankshaft to output power through the connecting rod. The connecting rod small end is connected to the piston through the wrist pin, and the rod big end is connected to the crankshaft. Combustion occurs above the piston in the combustion chamber, which is sealed by the ring pack, especially the top compression of the ring pack. Figure 2-1 shows these major components of the power cylinder system.

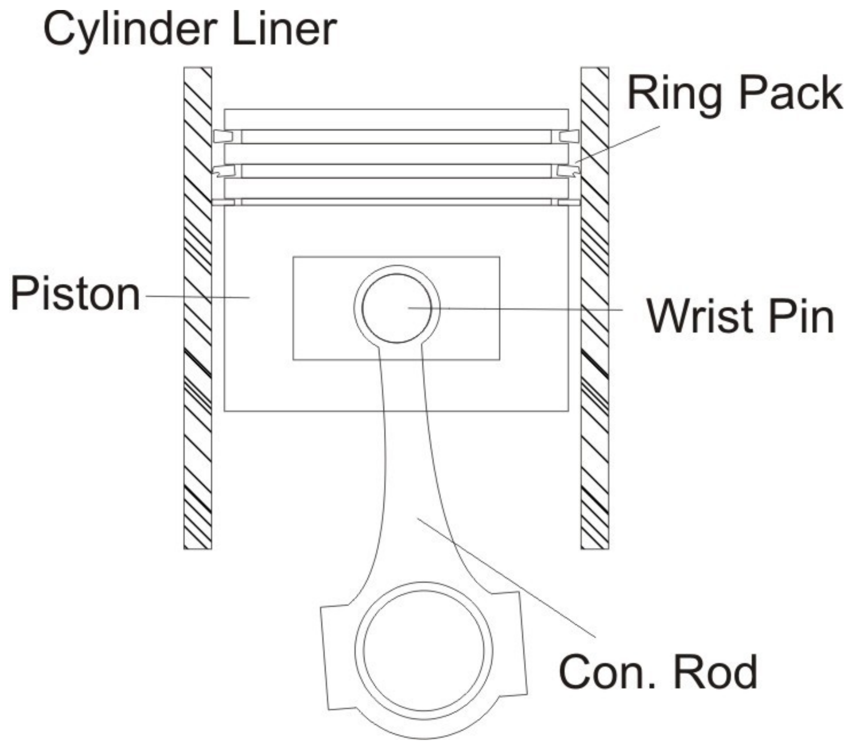

Figure 2-1 Engine power cylinder system

A complete engine cycle consists of 4 different strokes for a 4-stroke engine along with the piston reciprocating motion. These 4 strokes are intake stroke, compression stroke, expansion stroke and exhaust stroke as shown in Figure 2-2.

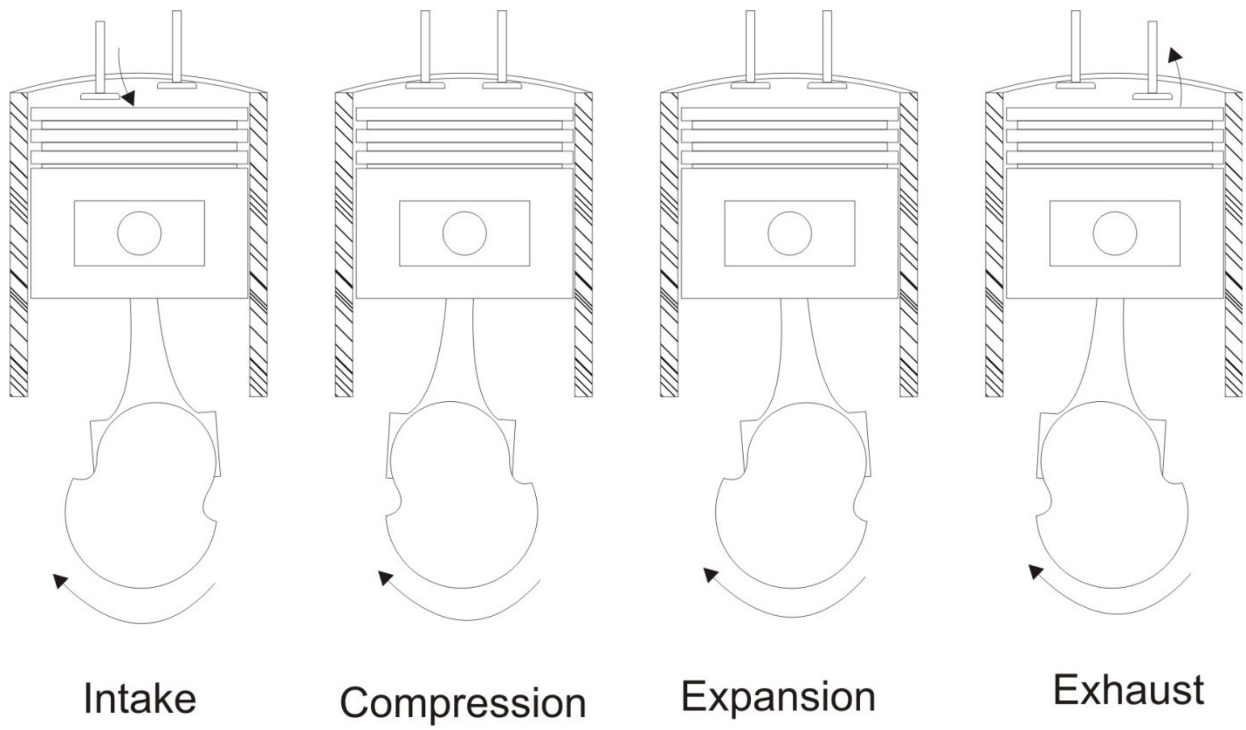

Figure 2-2 Engine strokes for 4-stroke engine

As for a modern diesel engine, which is known for its better efficiency over its gasoline counterpart, only about 40% of the energy produced by the engine is converted to the engine output power. About 4 – 15% of that energy is wasted as mechanical friction loss. And the rest of the energy, which is almost over half of the chemical energy is dissipated as other forms, e.g. heat transfer, blowby loss, etc as shown in Figure 2-3 from the study by Richardson [41].

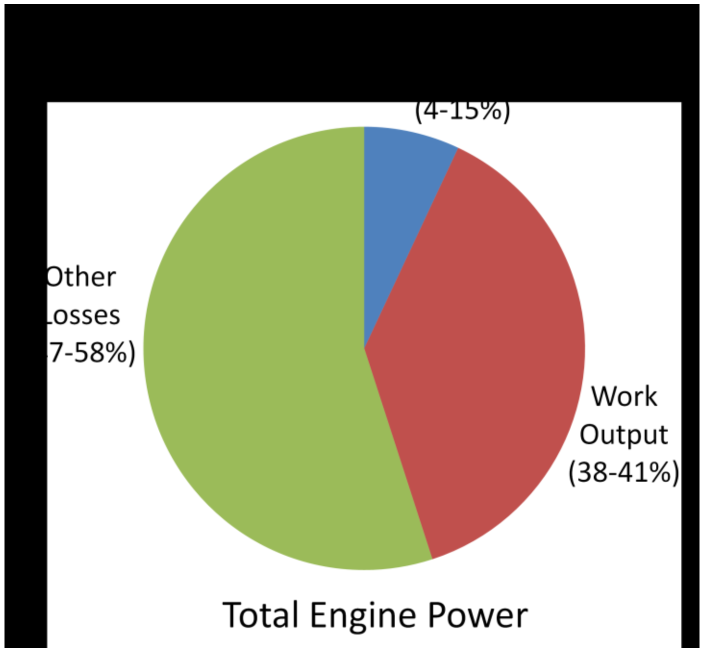

Figure 2-3 Power distribution for diesel engine

And about half of the mechanical friction loss is attributed to the friction in the power cylinder system, including the piston, ring pack and the connecting rod as shown in Figure 2-4 [41]. The other part is due to the friction of other components, e.g. the valve train system, the crankshaft bearings, etc.

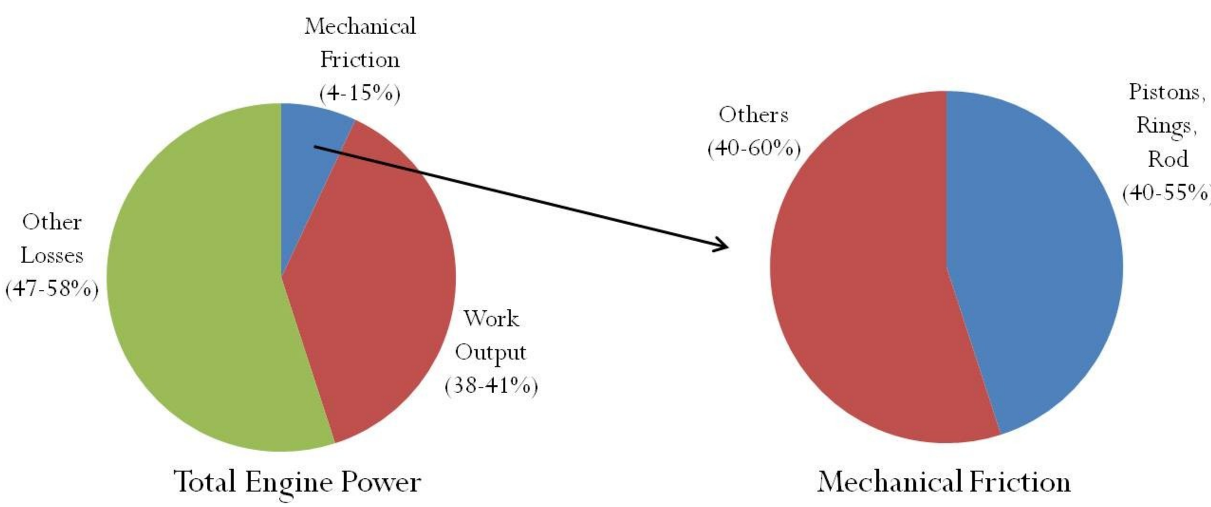

Figure 2-4 Mechanical friction power distribution

The friction loss distribution among piston, piston ring pack and the connecting rod for the power cylinder system can be found in Figure 2-5 [41]. As can be found, the piston and ring pack account for higher friction loss than the connecting rod.

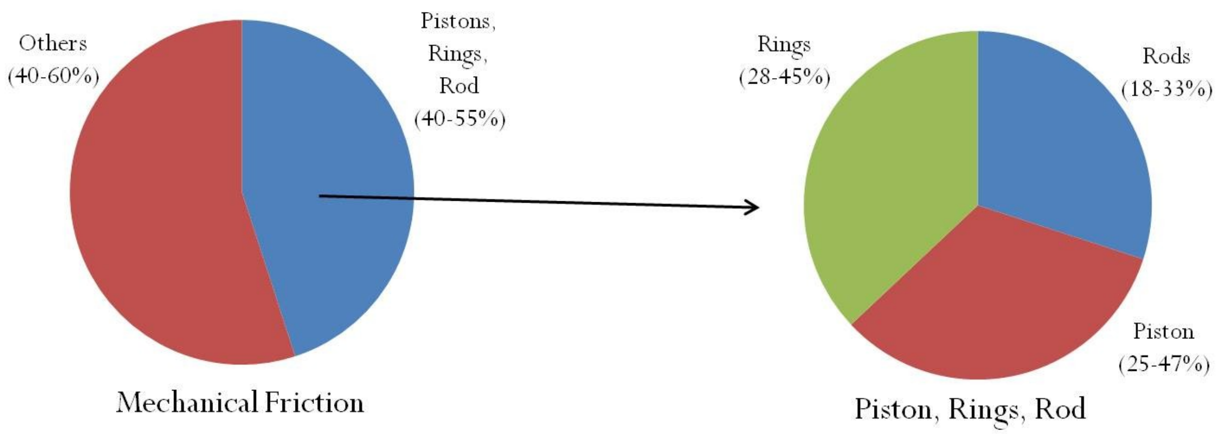

Figure 2-5 Power cylinder system friction distribution

2.2 Piston

The piston of an internal combustion engine is the main component to transmit the thermal energy into mechanical energy. High pressure gas from the combustion of the fuel-air mixture pushes the piston downward to deliver mechanical energy. Thus the working condition for the piston is severe. Pistons in small engines are made of aluminum while for large lower speed applications, the pistons are made of cast iron [42]. Figure 2-6 shows a typical piston for diesel engine with the definitions of the key geometries shown in Table 2-1.

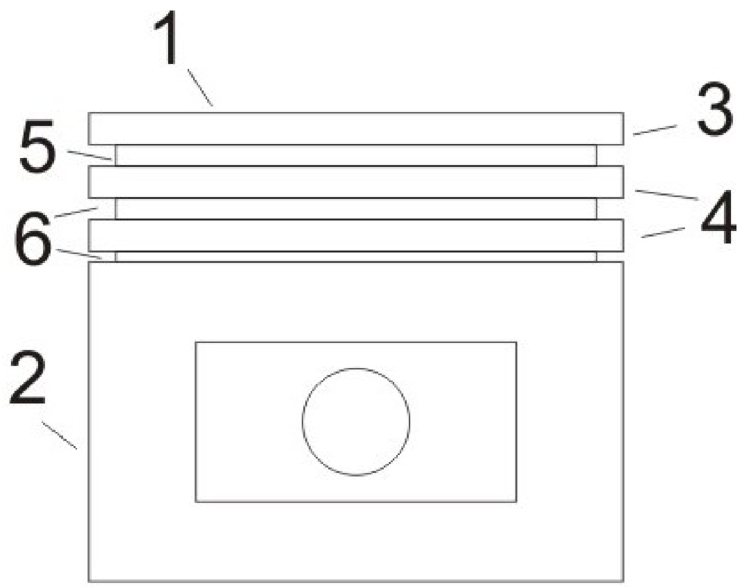

Figure 2-6 Key piston geometries

Table 2-1 Definitions of key piston geometries

No.	Definitions
1	Piston Crown
2	Piston Skirt
3	Top Land
4	Second and Third Land
5	Top Groove
6	Second and Third Groove

The piston skirt generally has a barrel/parabolic profile that promotes hydrodynamic lubrication due to the edge effect (Figure 2-7). This skirt profile needs to be optimized in order to minimize piston friction. Piston skirt also grows outward in the radial direction at high temperature during engine operation.

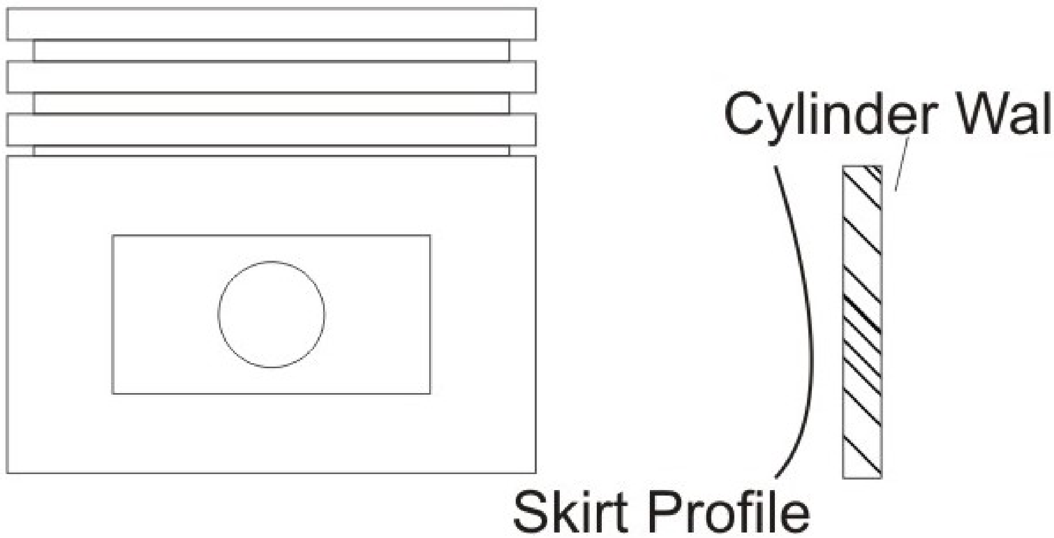

Figure 2-7 Piston skirt profile

2.3 Ring pack

The ring pack is typically comprised with three rings: two compression rings and one oil control ring. The main functions of the ring pack are listed as following:

- To seal the combustion chamber in conjunction with the piston lands and the cylinder wall, in order to prevent the high pressure gas from leaking into the crankcase that is wasted in producing power.
- To control the lubrication oil from getting into the combustion chamber from below the piston as well as to distribute the lubrication oil evenly on the cylinder wall.

- To transfer heat from the piston to the cylinder wall, and eventually to the cooling system. Since the piston crown in exposed to the combustion chamber, it is critical to reduce the piston temperature in order to guarantee the piston's working condition.

Figure 2-8 shows typical ring packs for modern gasoline and diesel engines.

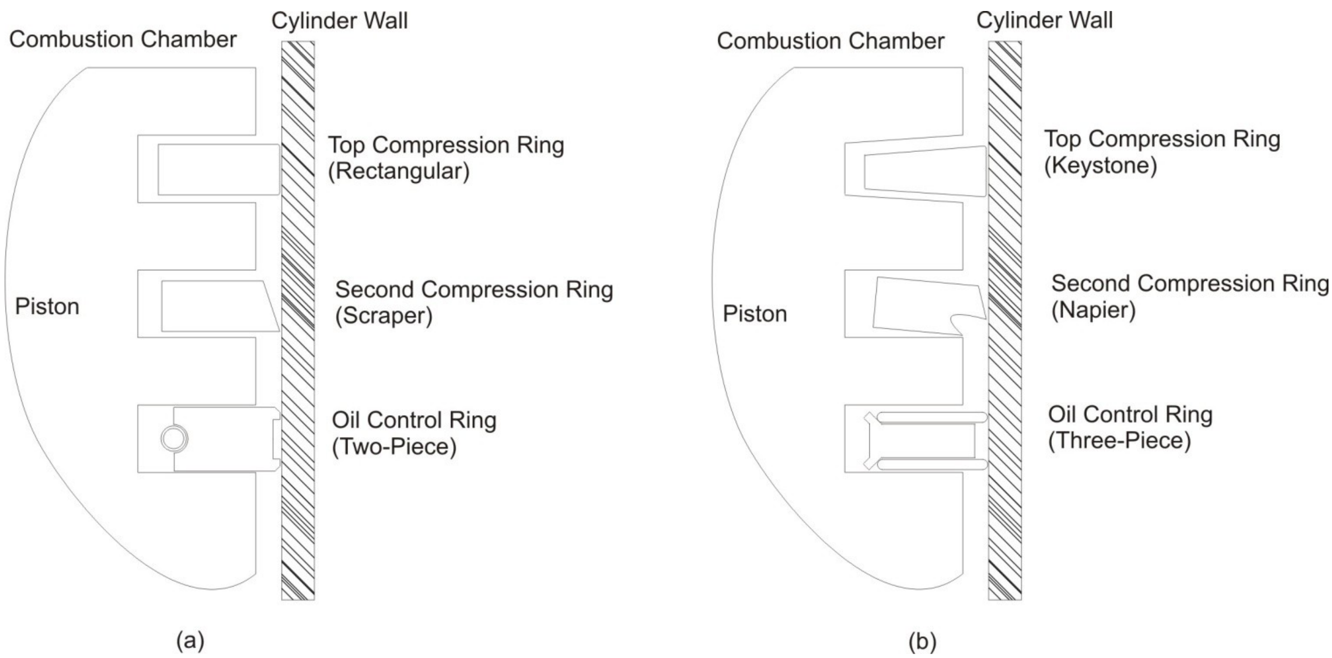

Figure 2-8 IC engine ring pack: (a) gasoline engine and (b) diesel engine

2.3.1 Top compression ring

The top compression ring is the first ring and the main component sealing the combustion chamber for engine blowby control. The top ring is also under the most severe working condition since it is directly exposed to the combustion gas and usually under high pressure and high temperature.

The top compression rings for gasoline engine usually have a rectangular cross-section. However, for diesel engine operation, the top compression rings usually are keystone rings (Figure 2-9) which promotes the break-up of the deposits between the ring and piston groove, thus reduce the possibility of micro-welding between the piston ring and the piston groove. The top compression ring usually has parabolic or barrel profile at its front face in order to enhance the hydrodynamic lubrication between the ring face and the cylinder wall interface (Figure 2-9).

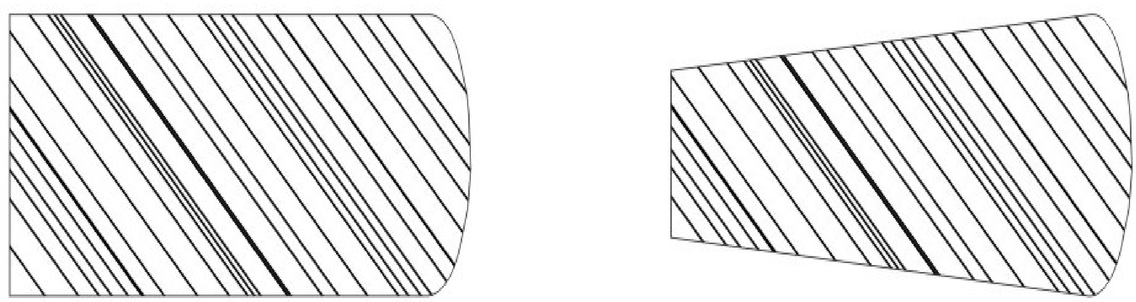

Figure 2-9 Top compression ring

The sealing capability of the top compression ring has significant influence of engine blowby because of the high gas pressure gradient across the top ring. Engine blowby is recognized as the high pressure gas leaking into the crankcase through the ring pack. Thus, the top compression ring is desired to conform to the cylinder wall evenly along the ring circumference. Also due to the high gas pressure gradient across the top ring, the top ring stays against the bottom side of the piston groove most time during the engine cycle.

2.3.2 Second compression ring

The second ring is a scraper ring which is recognized as 80% for scraping the lubrication oil down and 20% for sealing the combustion chamber. Because of the wedge effect, the scraper ring promotes hydrodynamic lubrication during the up-strokes (compression and exhaust strokes) and scrapes oil down during the down-strokes (intake and expansion strokes). Figure 2-10 shows two types of second rings: one is scraper ring and the other is Napier ring. For the second ring, static twist is usually introduced by cutting off the ring material at one of the back corners. If the lower inside corner is cut-off, the ring is a negative static twisted ring; while if the upper inside corner is cut-off, the ring has a positive static twist configuration.

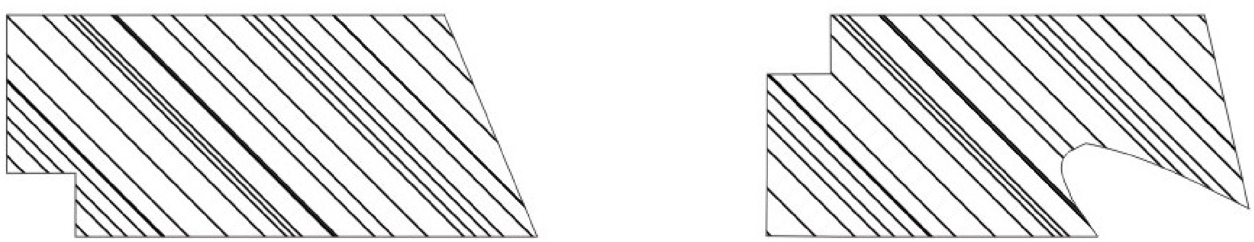

Figure 2-10 Second compression ring

Although the gas pressure gradient across the second compression ring is much lower than that of the top ring, the second ring also has noticeable effect on gas dynamics. Due to this lower pressure gradient across the second ring, the ring inertial force becomes competitive to gas pressure force. The inertial force may lift the second ring up at late compression stroke such that the second ring stays against the top flank of the groove. This process may repeat depending on the pressure build-up above the second ring when it is top seated. This unstable axial in-groove motion is recognized as ring fluttering. The scenario of ring fluttering is shown in

Figure 2-11. When the ring fluttering occurs, another gas flow path between the ring and groove sides is open. As a result, blowby gas may increase.

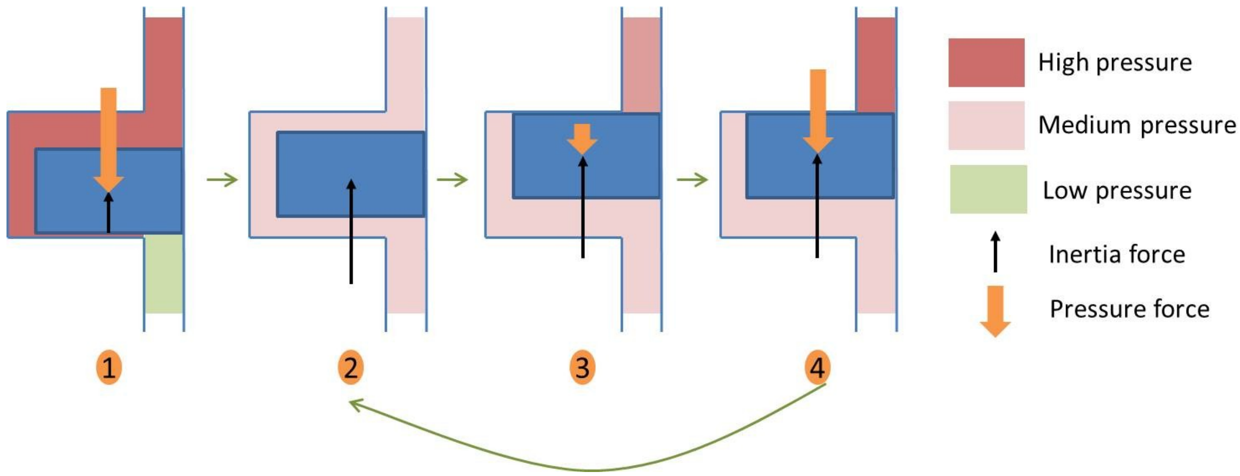

Figure 2-11 Ring fluttering scenario

It is also possible for the second ring to move inward in the radial direction. This radial movement is known as ring radial collapse. The scenario of ring collapse can be found in Figure 2-12. When the ring radial collapse occurs, the gas above the ring can flow past the ring directly between the ring face and the cylinder wall to the lower land. Severe engine blowby can occur at this ring collapse condition. It depends on the ring and piston design which of the two conditions occur, ring fluttering or ring collapse. It is also possible that the two conditions occur simultaneously.

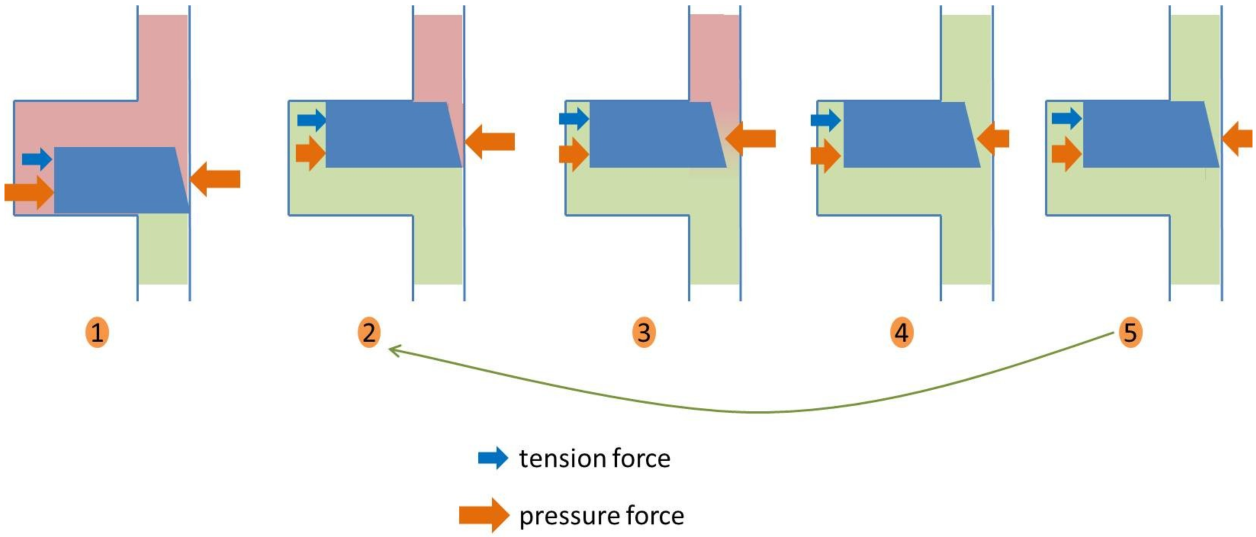

Figure 2-12 Ring collapse scenario

It was found that the static twist has significant influence on the second ring fluttering and radial collapse. Second ring with negative static twist is more likely to flutter than a positive static twist second ring. However, if the second ring is lifted against the top flank of the groove, the positive static twist configuration will be more like to collapse than the negative twist configuration.

2.3.3 Oil control ring

The oil control ring is used to meter and distribute lubrication oil onto the cylinder wall. There are generally two types of oil control rings: 1. two-piece oil control ring and 2. three-piece oil control ring (Figure 2-13). The two-piece oil control ring consists a ring body with two rails and a helical spring on the back providing the ring tension force. The three-piece oil control ring consists of two segments and an expander in between the two segments. The expander provides the radial force to conform the ring to the cylinder wall and also the axial force to push the ring against the top and bottom sides of the groove. The oil control ring is a two-direction scraper ring that scrapes oil in both upward strokes and downward strokes. During the downward strokes, the bottom rail/segment scrapes oil directly back into the crankcase. The top rail/segment scrapes oil back into the groove through the oil control ring expander. Generally, holes at the back of the oil control ring groove can be found along the circumference in order to allow the oil draining to the crankcase. In some piston design, instead of using these holes at the back of the groove, cast slots are introduced at the bottom edge of the groove for oil drain as an easier solution. During the upward strokes, the bottom rail/segment scrapes oil into the groove through the expander. The recovery of oil scraped by the top rail/segment during these upward strokes depends on the external force on the top rail/segment. At times the external axial force on the oil control ring overcomes the expander force. As a result, an oil flow crevice is formed between the oil control ring and the groove sides allowing the oil drain into the groove and eventually back to the crankcase.

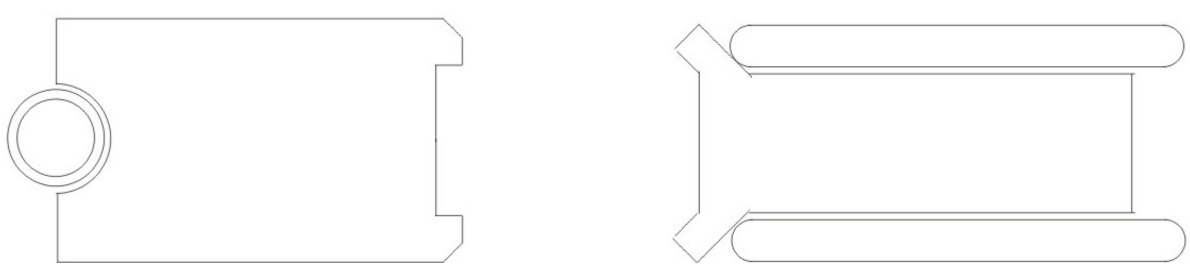

Figure 2-13 Oil control ring: two piece oil control ring (left), three piece oil control ring (right)

2.3.4 Key ring nomenclature

For all three piston rings, the ring tension force is important since The diametral load of the ring is defined as the load acting at the load acting at the locations ±90° from the ring end gap that also closes the ring gap. The tangential load is defined in this way: the piston ring is surrounded by a flexible band, the force at the end of the flexible band that closes the ring end gap when pulling. An empirical relationship between the diametral load and the tangential load is:

$$\boldsymbol{F_{diametral} = 2.1 \cdot F_{tangential}} \tag{2-1}$$

The ring radial pressure distribution is commonly known as defined by the ring ovality. The piston ring ovality is another important property of the ring determining the ring performance. From ISO 6621-2, in the ring ovality measurement test, the ring is enclosed in a flexible steel tension band. The two ends of the flexible band are pulled until the ring end gap is closed. Then the ring ovality is defined as the difference in diameter that through the ring end gap and ring back (0° to 180°) and the diameter perpendicular to this (90° to 270°) as shown in Figure 2-14. Negative ovality rings are widely used to reduce the pressure concentration at the ring tips, especially when the piston rings are under high temperature condition during engine operation.

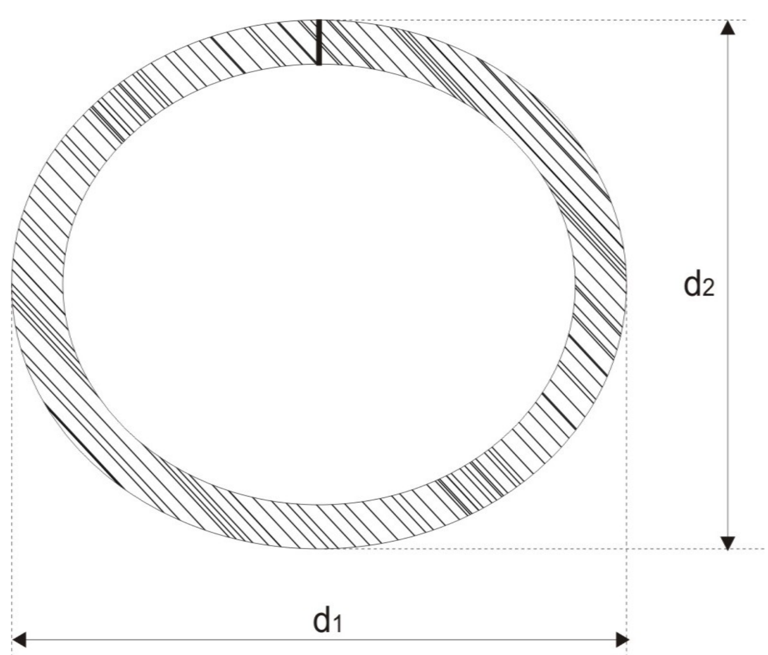

Figure 2-14 Ring ovality

Thus, based on the configuration shown in Figure 2-14, the ring ovality is defined as $d_2 - d_1$.

2.4 Cylinder

The cylinder of a reciprocating engine is the part through which the piston travels. The cylinder may be sleeved or sleeveless depending on the metal used for the engine block. For example, a cast iron engine block generally does not require cylinder sleeve because the iron is hard enough to resist wear between the piston ring and the cylinder wall. However, for aluminum alloy engine blocks that can be found in almost all daily drive cars, cylinder sleeves are required since the aluminum alloy is not hard to enough to resist wear between the piston ring and cylinder wall interface.

Cylinder liners, or cylinder sleeves, are manufactured nowadays using the centrifugal casting process. The centrifugal casting process refers to the technique for casting, which is a permanent mold is spinning continuously along its center line at a constant speed. At the same time, molten metal is poured to the mold and thrown toward to the inside wall of the mold. Then the molten metal is solidified after cooling. The spinning orientation of the casting machine can be either horizontal or vertical, depending on the parts it is producing. Horizontal spin is preferred for long and thin cylinder; while vertical spin is preferred for short and wide cylinders. Aluminum engines without sleeves can also be found. The aluminum cylinders are treated with nickel silicone alloy coating or other plasma coating that help reduce cylinder wear. Other techniques have also been explored by the researchers in order to reduce engine friction. One method is to introduce dimples at the mid-stroke to the cylinder walls [43]. This helps reduce friction because at the mid-stroke, the piston rings are generally under hydrodynamic friction since the piston speed is high. By introducing the dimples to the cylinder wall, the effective area of contact between the ring faces and the cylinder wall has been reduced. This leads to reduction of viscous friction as claimed.

Typical surface roughness for cylinder liner is 0.4~0.5 μm. This roughness has been reduced significantly, which could help reduce engine oil consumption. Rougher cylinder walls can help retain lubrication oil on the liner surface between micro-valleys, which is similar to the dimple-liner [43]. As a result, friction between the ring/cylinder wall and piston skirt/cylinder wall interfaces can be reduced due to the lubrication oil in the micro-valleys. However, this micro-valley retained oil is not scraped from the liner during engine down strokes and can stay exposed to high temperature gases. As a result, more oil is evaporated and the oil consumption increases.

Cylinder liners are no longer circular when the engine is in operation. The deformation results from mechanical distortion from bolting the cylinder block to the cylinder head; thermal distortion when the thermal load on the liner is not uniform; mechanical load when piston and ring pack are slapping into the liner; etc. Cylinder bore distortion is measured from experiment by researchers [44]. For modeling concern, the cylinder bore distortion is usually defined by a Fourier series [30, 44]:

$$\boldsymbol{\delta R} = \sum_{\boldsymbol{i=0}}^{\boldsymbol{i=4}} (\boldsymbol{A_i} \cos(\boldsymbol{i\theta}) + \boldsymbol{B_i} \sin(\boldsymbol{i\theta})) \qquad (2\text{-}2)$$

where δR is the deviation from roundness, A_i and B_i are Fourier coefficients and i is the order of the series.

The orders of the distortion are recognized as:

0 order	Change in bore diameter
1st order	Bore eccentricity
2nd order	Oval deformation
3rd order	3 lobe deformation
4th order	4 lobe deformation

Figure Figure **2-15** shows a piston bore deformation. The blue curve shows the ideal round bore without distortion. The green, red and yellow curves are bore shape under different distortion conditions.

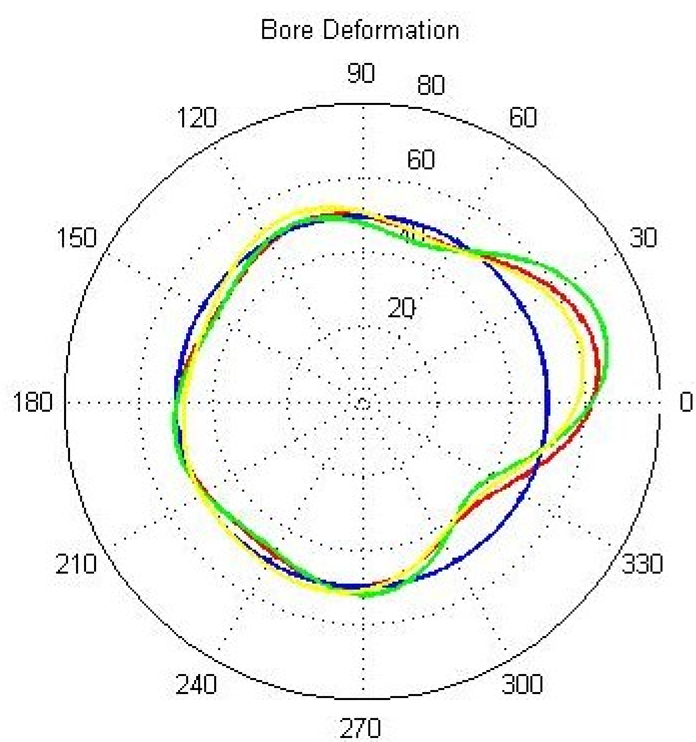

Figure 2-15 Cylinder bore distortion

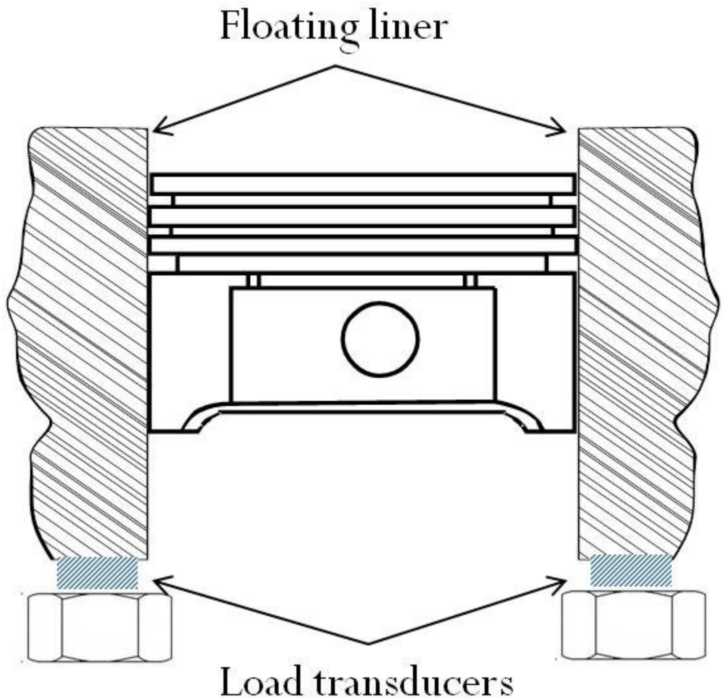

Figure 2-16 Floating liner setup

Floating cylinder liners Figure 2-16 are used for piston and ring pack friction force measurement. A floating liner refers to the liner supported by load transducers, instead of bolted to the cylinder block directly. Thus, by measuring the force on the load transducers, the piston and ring pack friction force can be estimated [45-50].

2.5 Connecting rod

The connecting rod connects the reciprocating moving part, the piston through the small end to the rotating moving part, the crankshaft through the big end. Thus, the connecting rod has both the reciprocating motion property as well as the rotating motion property. It is often recognized that $1/3$ of the connecting rod mass is for reciprocation and $2/3$ for rotation.

2.6 Wrist pin

The wrist pin connects the piston to the small end of the connecting rod. Thus, forces from the combustion are transmitted to the connecting rod through the wrist pin.

The wrist pin has two different configurations: semi-floating and fully-floating configurations.

For the semi-floating configuration, the wrist pin is either fixed relative to the piston or fixed relative to the connecting rod small ending. For the semi-floating configuration with wrist pin fixed relative to the piston, the pin has interference fit with the journal in the piston. The other configuration, with the wrist pin relatively fixed to the connecting rod small end, is implemented with interference fit at the connecting rod instead of piston. However, in this design, the piston lubrication can be affected since all the oscillations from the connecting rod are transferred to the pin-boss. On technique for solving this problem is to drill oil traveling paths from the oil ring groove to the pin-boss to enhance lubrication at this level.

For the fully-floating configuration, bearing surfaces can be found between the small end of the connecting rod and the wrist pin, as well as between the piston and the pin. No interference fit is used so the wrist pin is free to rotate. This floating design improves the scuff resistance and reduces the wear rate.

Chapter 3 THREE-DIMENSIONAL RING-CYLINDER WALL AND RING-PISTON GROOVE CONTACT MODELING

3.1 Introduction

Piston ring pack has significant influence on engine power cylinder system performance as discussed in the previous chapters. The areas piston ring pack affects include lubrication, friction, wear, fuel consumption, emission, heat transfer, etc. Thus, thorough understanding of the ring pack behavior is necessary for engine power cylinder system design improvement. Significant amount of effort has been committed into the ring pack dynamic, tribological behaviors. All these behaviors are closely related to the interaction between the ring/cylinder wall interface and the ring/piston groove interface. However, these interactions nowadays are still less understanding areas. This chapter presents a three-dimensional ring-cylinder wall and ring-piston groove contact model solving the above problem.

3.2 Finite element analysis formulation

Finite element method (FEM hereafter) is a numerical technique finding approximate solutions for differential equations. Instead of solving the very complex geometry that the existing mathematical tools are not capable of, FEM solves the boundary or initial value problem by dividing the complex geometry into simple small elements. Thus, approximated solutions for problems with complicated geometries under certain boundary condition can be obtained by solving a system of equations.

The formulation of the piston ring/cylinder ball and piston ring/groove contact finite element model is discussed in the following paragraphs.

3.2.1 Governing Equations

The basic of this finite element model is the theory from material of elasticity, focusing on the displacement at certain loading condition. And the governing equations for the problem are shown in the following :

i. Balance equation

ii. Strain-stress relation

iii. Strain-displacement relation

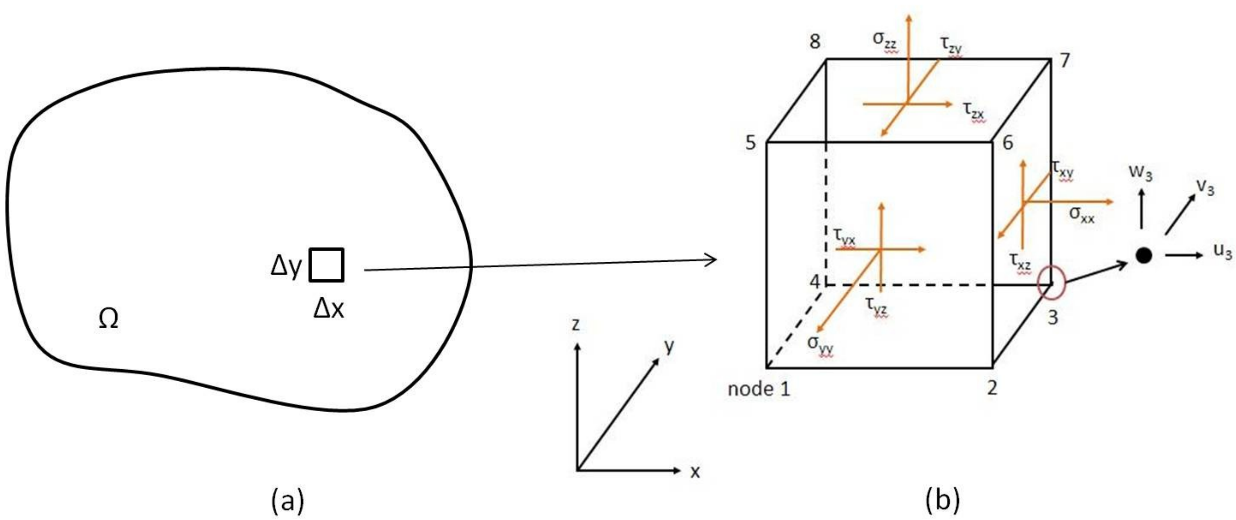

Figure 3-1 Finite element of an arbitrary domain

For any part of an arbitrary body Ω, which can be considered as a small element, under load at its boundaries Γ_i, the element must be in equilibrium due to the internal stress developed (Figure 3-1). This leads to the balance equations of this small element:

$$\frac{\partial \sigma_x}{\partial x} + \frac{\partial \tau_{yx}}{\partial y} + \frac{\partial \tau_{zx}}{\partial z} + f_x = 0 \tag{3-1}$$

$$\frac{\partial \sigma_y}{\partial y} + \frac{\partial \tau_{xy}}{\partial x} + \frac{\partial \tau_{zy}}{\partial z} + f_y = 0 \tag{3-2}$$

$$\frac{\partial \sigma_z}{\partial z} + \frac{\partial \tau_{xz}}{\partial x} + \frac{\partial \tau_{yz}}{\partial y} + f_z = 0 \tag{3-3}$$

where σ_x, σ_y and σ_z are the normal stresses on the planes perpendicular to the x, y and z axis; τ_{xy}, τ_{yx}, τ_{xz}, τ_{zx}, τ_{yz} and τ_{zy} are shear stresses, the first index denotes the axis the plane is perpendicular to and the second index indicates the direction of the shear stress, for example, τ_{yx} is defined as the shear stress on the plane perpendicular to the y axis and along the x direction; f_x, f_y and f_z are body forces along three different orientations respectively.

For an isotropic material, the following relations hold:

$$\tau_{xy} = \tau_{yx} \tag{3-4}$$

$$\tau_{xz} = \tau_{zx} \tag{3-5}$$

$$\tau_{yz} = \tau_{zy} \tag{3-6}$$

Thus, for a 3D problem with isotropic material, there are six unknowns for one element, which are σ_x, σ_y, σ_z and τ_{xy}, τ_{yz}, τ_{zx}.

From Hooke's law for isotropic material, the relation between stress and strain in 3D can be expressed as:

$$\varepsilon_x = \frac{\sigma_x}{E} - \mu\frac{\sigma_y}{E} - \mu\frac{\sigma_z}{E} \tag{3-7}$$

$$\varepsilon_y = \frac{\sigma_y}{E} - \mu\frac{\sigma_x}{E} - \mu\frac{\sigma_z}{E} \tag{3-8}$$

$$\boldsymbol{\varepsilon_z = \frac{\sigma_z}{E} - \mu\frac{\sigma_x}{E} - \mu\frac{\sigma_y}{E}} \tag{3-9}$$

$$\boldsymbol{\gamma_{xy} = \frac{2\cdot(1+\mu)}{E}\tau_{xy}} \tag{3-10}$$

$$\boldsymbol{\gamma_{yz} = \frac{2\cdot(1+\mu)}{E}\tau_{yz}} \tag{3-11}$$

$$\boldsymbol{\gamma_{zx} = \frac{2\cdot(1+\mu)}{E}\tau_{zx}} \tag{3-12}$$

γ in the above equations are engineering shear strains, which have the relation with shear strain as:

$$\boldsymbol{\gamma_{xy} = \varepsilon_{xy} + \varepsilon_{yx} = 2\varepsilon_{xy}} \tag{3-13}$$

$$\boldsymbol{\gamma_{yz} = \varepsilon_{yz} + \varepsilon_{zy} = 2\varepsilon_{yz}} \tag{3-14}$$

$$\boldsymbol{\gamma_{zx} = \varepsilon_{zx} + \varepsilon_{xz} = 2\varepsilon_{zx}} \tag{3-15}$$

The same relationships can be expressed in the form of stresses as the functions of strains, as shown in the following:

$$\boldsymbol{\sigma_x = \frac{E}{(1+\mu)(1-2\mu)}\left[(1-\mu)\varepsilon_x + \mu\varepsilon_y + \mu\varepsilon_z\right]} \tag{3-16}$$

$$\boldsymbol{\sigma_y = \frac{E}{(1+\mu)(1-2\mu)}\left[(1-\mu)\varepsilon_y + \mu\varepsilon_x + \mu\varepsilon_z\right]} \tag{3-17}$$

$$\boldsymbol{\sigma_z = \frac{E}{(1+\mu)(1-2\mu)}\left[(1-\mu)\varepsilon_z + \mu\varepsilon_x + \mu\varepsilon_y\right]} \tag{3-18}$$

$$\boldsymbol{\tau_{xy} = \frac{E}{2\cdot(1+\mu)}\cdot\gamma_{xy}} \tag{3-19}$$

$$\boldsymbol{\tau_{yz} = \frac{E}{2\cdot(1+\mu)}\cdot\gamma_{yz}} \tag{3-20}$$

$$\boldsymbol{\tau_{zx} = \frac{E}{2\cdot(1+\mu)}\cdot\gamma_{zx}} \tag{3-21}$$

In the above relationship, ε is the normal strain, E is the Young's modulus of the material and μ is the Poisson's ratio.

It can also be expressed using shear modulus, which is defined as:

$$\boldsymbol{G} = \frac{\boldsymbol{E}}{\mathbf{2(1+\mu)}} \tag{3-22}$$

Thus,

$$\boldsymbol{\tau_{xy} = G \cdot \gamma_{xy}} \tag{3-23}$$

$$\boldsymbol{\tau_{yz} = G \cdot \gamma_{yz}} \tag{3-24}$$

$$\boldsymbol{\tau_{zx} = G \cdot \gamma_{zx}} \tag{3-25}$$

In a matrix form, the above relations can be expressed as:

$$\begin{pmatrix} \sigma_x \\ \sigma_y \\ \sigma_z \\ \tau_{xy} \\ \tau_{yz} \\ \tau_{zx} \end{pmatrix} = C \cdot \begin{pmatrix} \varepsilon_x \\ \varepsilon_y \\ \varepsilon_z \\ \gamma_{xy} \\ \gamma_{yz} \\ \gamma_{zx} \end{pmatrix} \tag{3-26}$$

And C is the constitutive matrix:

$$C = \frac{E}{(1+\mu)(1-2\mu)} \begin{bmatrix} 1-\mu & \mu & \mu & & & \\ \mu & 1-\mu & \mu & & 0 & \\ \mu & \mu & 1-\mu & & & \\ & & & \frac{1-2\mu}{2} & 0 & 0 \\ & 0 & & 0 & \frac{1-2\mu}{2} & 0 \\ & & & 0 & 0 & \frac{1-2\mu}{2} \end{bmatrix} \tag{3-27}$$

The constitutive matrix defines the stress-strain relationship.

Another important relation is the Strain Displacement Relation. The strain is a normalized measure of displacement and it is related to the displacements as:

$$\boldsymbol{\varepsilon_x = \frac{\partial u}{\partial x}} \tag{3-28}$$

$$\boldsymbol{\varepsilon_y = \frac{\partial v}{\partial y}} \tag{3-29}$$

$$\boldsymbol{\varepsilon_z = \frac{\partial w}{\partial z}} \tag{3-30}$$

$$\boldsymbol{\gamma_{xy} = \frac{\partial v}{\partial x} + \frac{\partial u}{\partial y}} \tag{3-31}$$

$$\boldsymbol{\gamma_{yz} = \frac{\partial v}{\partial z} + \frac{\partial w}{\partial y}} \tag{3-32}$$

$$\boldsymbol{\gamma_{zx} = \frac{\partial w}{\partial x} + \frac{\partial u}{\partial z}} \tag{3-33}$$

where u, v and w are displacements in the x, y and z directions respectively.

The above relationship can also be expressed in a matrix form:

$$\boldsymbol{\begin{pmatrix} \varepsilon_x \\ \varepsilon_y \\ \varepsilon_z \\ \gamma_{xy} \\ \gamma_{yz} \\ \gamma_{zx} \end{pmatrix} = D \cdot \begin{pmatrix} u \\ v \\ w \end{pmatrix}} \tag{3-34}$$

where $D = \begin{bmatrix} \frac{\partial}{\partial x} & 0 & 0 \\ 0 & \frac{\partial}{\partial y} & 0 \\ 0 & 0 & \frac{\partial}{\partial z} \\ \frac{\partial}{\partial y} & \frac{\partial}{\partial x} & 0 \\ 0 & \frac{\partial}{\partial z} & \frac{\partial}{\partial y} \\ \frac{\partial}{\partial z} & 0 & \frac{\partial}{\partial x} \end{bmatrix}$

3.2.2 Finite Element Analysis

Eight-node hexahedron element is used to model the 3D ring. A basic hexahedron element is shown in the Figure 3-2 (a) below. An arbitrary shaped hexahedron element needs to be mapped to its parent element – a cubic element with all its sides equal to unit (Figure 3-2 b) thus only the parent element's shape function needs to be calculated.

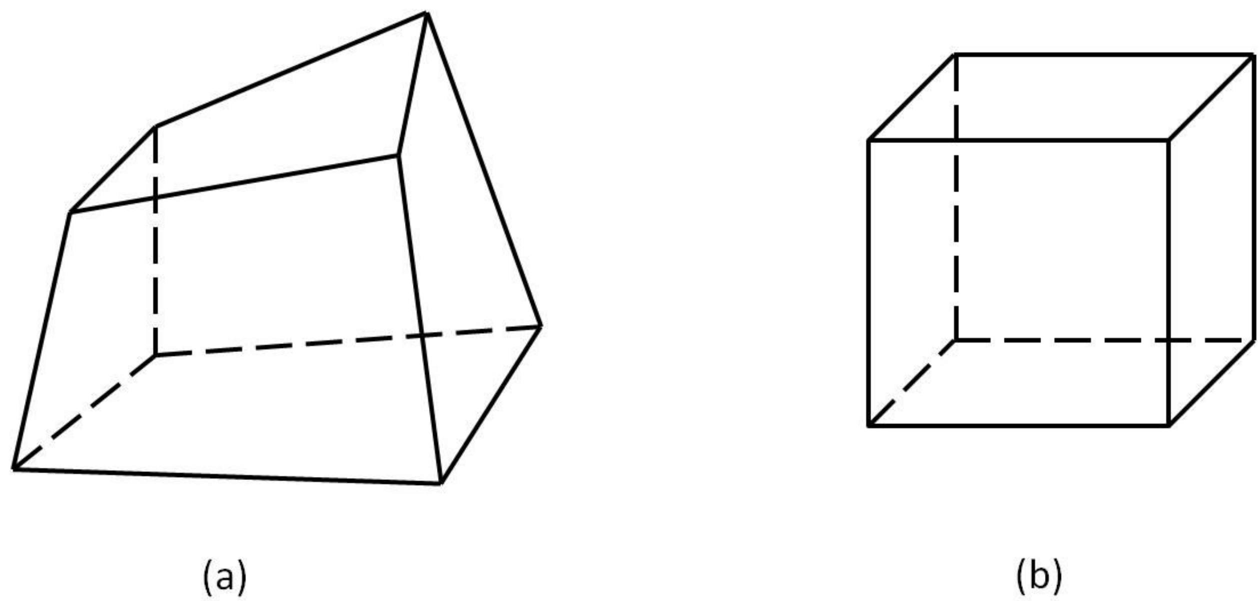

Figure 3-2 Hexahedron element (a) and parent element (b)

In FEM, interpolation method is widely used to represent the quantities (displacements, temperature, etc) at element nodes. This interpolation function is called shape function. For the parent element with the prescribed coordinate system (Figure 3-3), the shape functions for the parent element are defined as:

$$\boldsymbol{N_1 = \frac{1}{8} \cdot (1-x)(1-y)(1-z)} \tag{3-35}$$

$$\boldsymbol{N_2 = \frac{1}{8} \cdot (1+x)(1-y)(1-z)} \tag{3-36}$$

$$\boldsymbol{N_3 = \frac{1}{8} \cdot (1+x)(1+y)(1-z)} \tag{3-37}$$

$$\boldsymbol{N_4} = \frac{\mathbf{1}}{\mathbf{8}} \cdot (\mathbf{1} - \boldsymbol{x})(\mathbf{1} + \boldsymbol{y})(\mathbf{1} - \boldsymbol{z}) \tag{3-38}$$

$$\boldsymbol{N_5} = \frac{\mathbf{1}}{\mathbf{8}} \cdot (\mathbf{1} - \boldsymbol{x})(\mathbf{1} - \boldsymbol{y})(\mathbf{1} + \boldsymbol{z}) \tag{3-39}$$

$$\boldsymbol{N_6} = \frac{\mathbf{1}}{\mathbf{8}} \cdot (\mathbf{1} + \boldsymbol{x})(\mathbf{1} - \boldsymbol{y})(\mathbf{1} + \boldsymbol{z}) \tag{3-40}$$

$$\boldsymbol{N_7} = \frac{\mathbf{1}}{\mathbf{8}} \cdot (\mathbf{1} + \boldsymbol{x})(\mathbf{1} + \boldsymbol{y})(\mathbf{1} + \boldsymbol{z}) \tag{3-41}$$

$$\boldsymbol{N_8} = \frac{\mathbf{1}}{\mathbf{8}} \cdot (\mathbf{1} - \boldsymbol{x})(\mathbf{1} + \boldsymbol{y})(\mathbf{1} + \boldsymbol{z}) \tag{3-42}$$

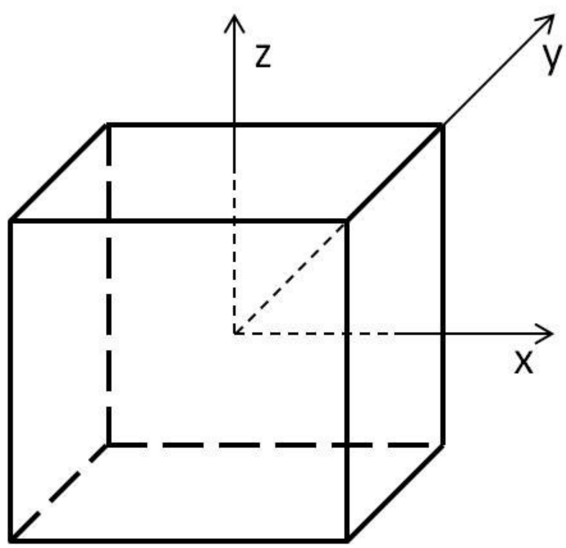

Figure 3-3 Parent element coordinate system

The way the shape function is defined ensures that the value of the shape function N_i is equal to 1 at node i, and 0 at node j when $i \neq j$ and the summation of all the shape function for one element is equal to one. The displacement of any point within the element can then be expressed using interpolation as the summation of the product of the shape function and the displacements at its 8 nodes.

The displacement can be found using the following relation:

$$\begin{pmatrix} \boldsymbol{u}_{(x,y)}^{(e)} \\ \boldsymbol{v}_{(x,y)}^{(e)} \\ \boldsymbol{w}_{(x,y)}^{(e)} \end{pmatrix} = \boldsymbol{N} \cdot \boldsymbol{U} \tag{3-43}$$

where $N = \begin{bmatrix} N_1 & 0 & 0 & N_2 & 0 & 0 & \cdots & N_8 & 0 & 0 \\ 0 & N_1 & 0 & 0 & N_2 & 0 & \cdots & 0 & N_8 & 0 \\ 0 & 0 & N_1 & 0 & 0 & N_2 & \cdots & 0 & 0 & N_8 \end{bmatrix}$

$$\boldsymbol{U} = \begin{pmatrix} \boldsymbol{u_1} \\ \boldsymbol{v_1} \\ \boldsymbol{w_1} \\ \vdots \\ \boldsymbol{u_8} \\ \boldsymbol{v_8} \\ \boldsymbol{w_8} \end{pmatrix} \tag{3-44}$$

where u_i denotes the displacement in the x direction for the ith node, and v_i and w_i are displacements in y and z directions for the ith node respectively.

And as will be discussed later, a hexahedron element with arbitrary dimensions would be mapped to the parent element using Jacobian matrix such that it is not necessarily to construct shape functions for each element.

The approximate solution of the balance equation may lead to a non-zero value (residual) in the right side of the equations as:

$$\boldsymbol{R_x} = \frac{\boldsymbol{\partial \sigma_x}}{\boldsymbol{\partial x}} + \frac{\boldsymbol{\partial \tau_{yx}}}{\boldsymbol{\partial y}} + \frac{\boldsymbol{\partial \tau_{zx}}}{\boldsymbol{\partial z}} + \boldsymbol{f_x} \neq \boldsymbol{0} \tag{3-45}$$

$$\boldsymbol{R_y} = \frac{\boldsymbol{\partial \sigma_y}}{\boldsymbol{\partial y}} + \frac{\boldsymbol{\partial \tau_{xy}}}{\boldsymbol{\partial x}} + \frac{\boldsymbol{\partial \tau_{zy}}}{\boldsymbol{\partial z}} + \boldsymbol{f_y} \neq \boldsymbol{0} \tag{3-46}$$

$$\boldsymbol{R_z = \frac{\partial \sigma_z}{\partial z} + \frac{\partial \tau_{yz}}{\partial y} + \frac{\partial \tau_{xz}}{\partial x} + f_z \neq 0} \tag{3-47}$$

R in the above equation is the residual.

Galerkin's method is trying to reduce the residual over the entire domain by making the integration of the weighted residual equal to zero. In order to generate as many equations as unknowns and not lose the generality, Galerkin's method uses the shape function itself as the weight function.

$$\boldsymbol{\iiint \omega_1 R d\Omega} \tag{3-48}$$

$$\vdots$$

$$\boldsymbol{\iiint \omega_n R d\Omega} \tag{3-49}$$

where $\omega_i = N_i$

Now, the governing equations can be written in the matrix form for one element:

$$\boldsymbol{[K]\{u\} = \{F\}} \tag{3-50}$$

where $[K] = \iiint ([D][N])^T [C][D][N]\, dxdydz$

$\boldsymbol{\{F\} = \iiint N \cdot \{f\}\, dxdydz}$

$[K]$ is the element stiffness matrix and $\{F\}$ is the load vector.

Integration is involved in the evaluation of element stiffness matrix and load vector. Gaussian quadrature is introduced here to calculate these integrations numerically.

Gaussian quadrature converts integration into summation of a series of polynomials evaluated at certain points. In a 3D domain with $\in [-1, +1]$, $y \in [-1, +1]$ and $z \in [-1, +1]$ the integration is calculated as:

$$\boldsymbol{I = \int_{-1}^{+1}\int_{-1}^{+1}\int_{-1}^{+1} f(\zeta, \eta, \varphi) d\zeta d\eta d\varphi}$$
$$\boldsymbol{= \sum_{i=1}^{2}\sum_{j=1}^{2}\sum_{k=1}^{2}\left[\omega_i \cdot \omega_j \cdot \omega_k \cdot f(\zeta, \eta, \varphi)\right]} \tag{3-51}$$

Two node Gaussian quadrature yields the exact value of the integration of up to third order polynomial. Gaussian quadrature requires the function to be integrated from -1 to +1 in all directions. For integrations with other upper and lower limits, the integration domain should be mapped to the parent domain first using Jacobian matrix.

As mentioned above earlier, in engineering applications, quite often the domain one's working on is non-rectangular. Or sometimes the regular rectangular element cannot define the domain properly. And to write the shape function individually for each element becomes tedious and impossible as the number of element increases. In this case, one could map the actual element to a parent element using Jacobian matrix, which is unique.

In this case, the integration for the stiffness matrix becomes:

$$\boldsymbol{k^e = \int B^{eT} C B^e d\Omega = \int_{-1}^{1}\int_{-1}^{1}\int_{-1}^{1} B^{eT} C B^e |J^e| d\zeta d\eta d\varphi =}$$
$$\boldsymbol{\sum_{i=1}^{2}\sum_{j=1}^{2}\sum_{k=1}^{2} W_i W_j W_k \left|J^e_{(\zeta_i, \eta_j, \varphi_k)}\right| B^{eT}_{(\zeta_i, \eta_j, \varphi_k)} C B^e_{(\zeta_i, \eta_j, \varphi_k)}} \tag{3-52}$$

where ζ_i , η_j and , φ_k are Gaussian quadratures; $|J^e|$ is the determinant of Jacobian of one element.

The Jacobian is defined as:

$$J^e = \begin{bmatrix} \frac{\partial x}{\partial \zeta} & \frac{\partial y}{\partial \zeta} & \frac{\partial z}{\partial \zeta} \\ \frac{\partial x}{\partial \eta} & \frac{\partial y}{\partial \eta} & \frac{\partial z}{\partial \eta} \\ \frac{\partial x}{\partial \varphi} & \frac{\partial y}{\partial \varphi} & \frac{\partial z}{\partial \varphi} \end{bmatrix} \tag{3-53}$$

With the Jacobian, the first derivatives of a shape function with respect to x, y and z can be transformed to the derivatives with respect to ζ, η and φ. And the following relations hold:

$$\begin{bmatrix} \frac{\partial N_i}{\partial \zeta} \\ \frac{\partial N_i}{\partial \eta} \\ \frac{\partial N_i}{\partial \varphi} \end{bmatrix} = [J^e] \begin{bmatrix} \frac{\partial N_i}{\partial x} \\ \frac{\partial N_i}{\partial y} \\ \frac{\partial N_i}{\partial z} \end{bmatrix} \text{ and } \begin{bmatrix} \frac{\partial N_i}{\partial x} \\ \frac{\partial N_i}{\partial y} \\ \frac{\partial N_i}{\partial z} \end{bmatrix} = [J^e]^{-1} \begin{bmatrix} \frac{\partial N_i}{\partial \zeta} \\ \frac{\partial N_i}{\partial \eta} \\ \frac{\partial N_i}{\partial \varphi} \end{bmatrix} \tag{3-54}$$

Known the Jacobian matrix, both the inverse of Jacobian matrix and the determinant of Jacobian can be expressed explicitly.

3.2.3 Ring-Cylinder Wall Contact Modeling

The 3D ring finite element analysis program is presented in this section solving the interaction between the piston ring front face and the cylinder wall [51].

This study describes a 3D analytical ring model to addresses the pressure/force distribution and the ring conformability between the ring-cylinder bore interface. The main contribution of this work is that it solves the problem from the minimum strain energy point of view without any unrealistic boundary condition assumptions. The penalty method is used to find the contact pairs between the ring and the cylinder liner. The finite element model is described in the following sections along with experimental measurement validation.

The piston ring cross-section geometries (Figure 3-4) need to be input to the model. This including the ring thickness t and radial width w, as well as the ring's keystone angle α and β if any. In addition, the bevel angle and length at any corner also need to be specified since they introduce ring static twist after installing the ring into the piston groove.

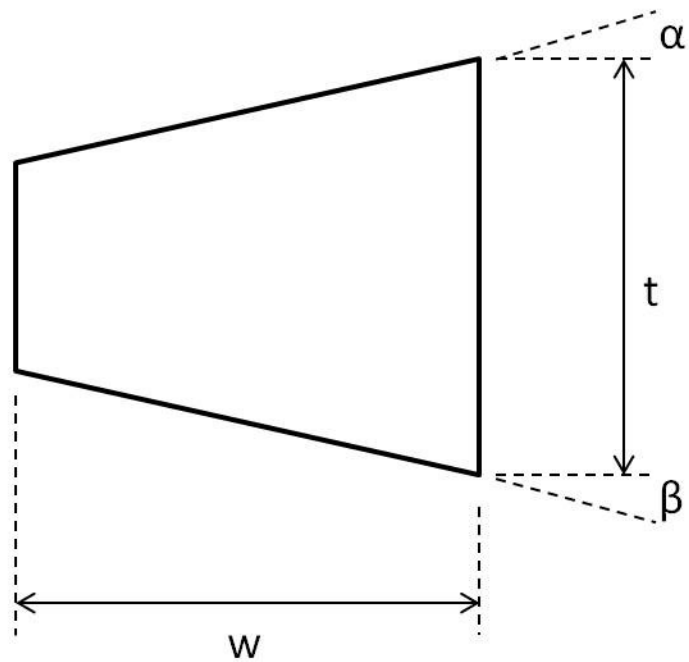

Figure 3-4 Ring Cross-Section

Another important input to the model is the ring outer diameter (OD) profile at its free state. The free state profile can be either measured using a coordinate measurement machine (CMM) or from a computer aided design (CAD) model. Figure 3-5 shows an example of the ring free state profile, normalized by the ring radius opposite to the ring end gap. As the center of the free state ring is really arbitrary, the point that yields the OD at the ring back (opposite to the ring end gap) equal to the cylinder bore inside diameter (ID) is picked as reference center. The selection of the ring center will not result in any difference on the result. The ring free state profile shown in Figure 3-5 is the normalized radius that the ring radius at any circumference location is normalized by the one at the ring back.

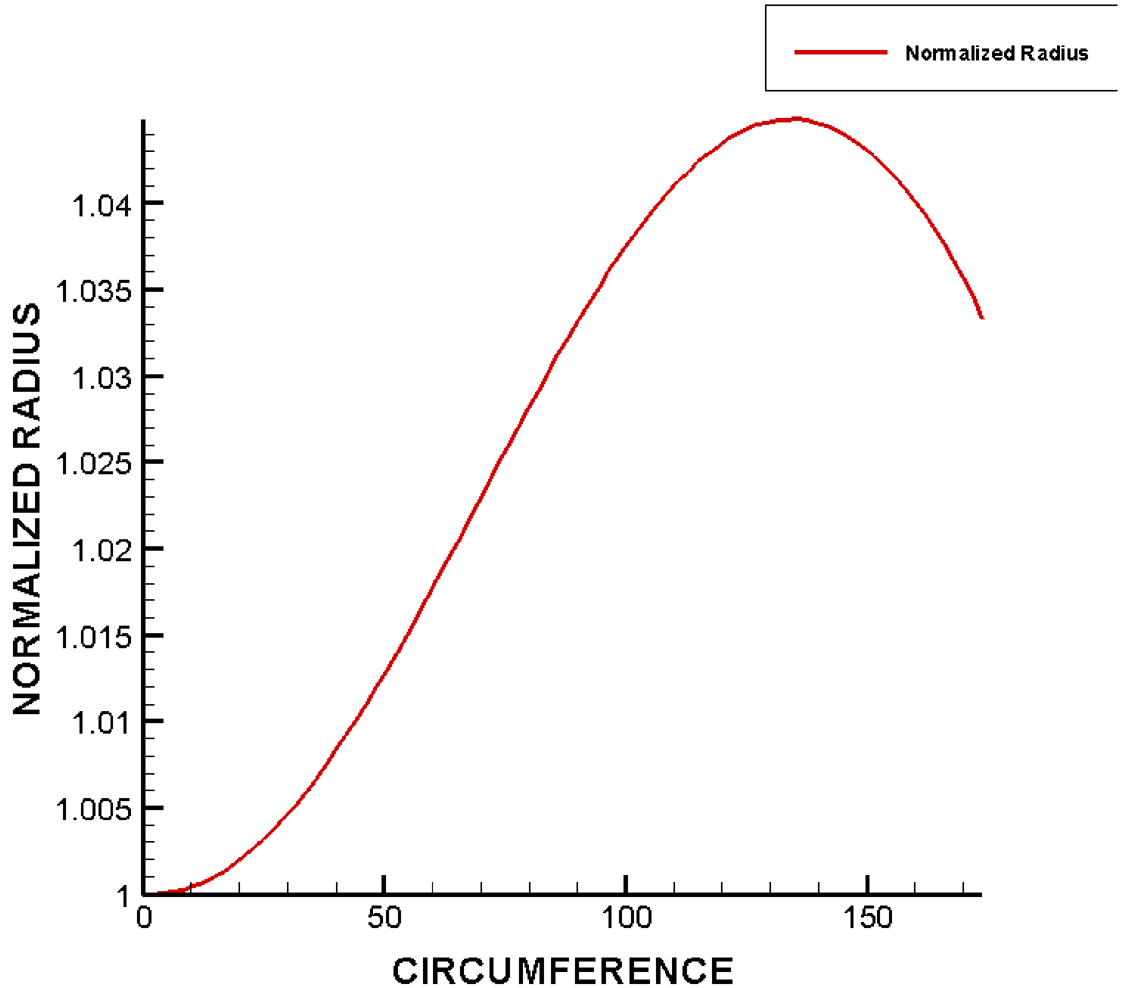

Figure 3-5 Normalized ring curvature

Figure 3-5 only shows one half of the ring assuming the ring is symmetric about the cross-section at the ring back.

The free state ring is then meshed using 8-node hexahedron element and is shown in Figure 3-6.

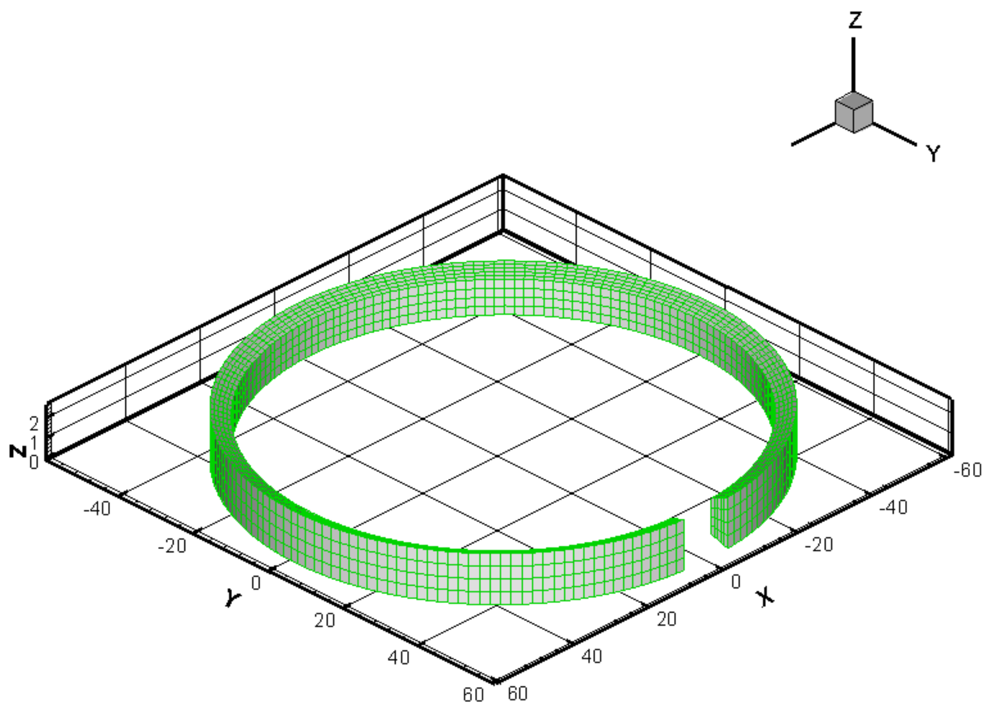

Figure 3-6 Free shape ring mesh with hexahedron elements

The penalty method is a widely used for solving contact problems [52, 53]. Compared to the other popular method, the Lagrange multiplier method, the order of the system is not increased using the penalty approach. Thus penalty method was chosen to solve the present ring-cylinder bore contact problem.

The base constrained optimization problem can be formulated using the principle of minimum total potential energy. This principle is a fundamental concept used in structure analysis analyzing structure deformation. It states that a structure should deform to a stationary state that minimizes its total potential energy, including the elastic strain energy and potential energy from the applied force. This principle is used to formulate the ring-cylinder bore contact problem. The formulation can then be expressed as:

To find nodal displacement: q

that minimizes the ring potential energy defined as:

$$\mathbf{\Pi} = \frac{1}{2}\mathbf{q}^{\mathrm{T}}\mathbf{K}\mathbf{q} - \mathbf{q}^{\mathrm{T}}\mathbf{f} \tag{3-55}$$

and subject to the constraint:

$$\mathbf{r}_{\mathrm{i}} \leq \mathbf{R}_{\mathbf{B}} \tag{3-56}$$

where $\mathrm{r_i}$ is the radius of the ith cross-section at the ring face and $\mathrm{R_B}$ is the radius of the cylinder wall.

The minimization of the potential energy requires the derivative of Π with respect to q vanishing, which is:

$$\mathbf{K}\mathbf{q} = \mathbf{f} \tag{3-57}$$

At the same time, the constraint implies that if the node on the ring front face is in contact with the cylinder bore, the constraint force should be non-zero and along the radial direction pointing inward to the center of the cylinder bore; on the other hand, if the node on the ring front face is not in contact against the cylinder bore, the constraint force should be zero. It is obvious that high nonlinearity is involved in the present contact problem. The penalty method is used to solve q by instead solving a sequence of specially constructed unconstrained optimization problem. That is, with the penalty method, an additional term that accounts the constraints is introduced into the system potential energy found in (3-55) as:

$$\mathbf{\Pi}_{\mathbf{P}} = \frac{1}{2}\mathbf{q}^{\mathrm{T}}\mathbf{K}\mathbf{q} - \mathbf{q}^{\mathrm{T}}\mathbf{f} + \frac{1}{2}\mathbf{g}^{\mathrm{T}}\boldsymbol{\lambda}\mathbf{g} \tag{3-58}$$

where λ is the penalty number and g represents the node geometric constraint and can be expressed in the matrix form as:

$$\mathbf{g} = \mathbf{A}\mathbf{q} - \mathbf{c} \tag{3-59}$$

Here, $\mathbf{c}$ is the gap between the node's initial free state position and the final deformed state and matrix A projects the nodal DOF to the gap. Now, the minimization of the modified potential energy accounting for the penalties requires the derivatives of Π_{P} with respect to q to vanish, which yields the following relation:

$$[\mathbf{K} + \mathbf{A}^{\mathbf{T}}\boldsymbol{\lambda}\mathbf{A}]\mathbf{q} = \mathbf{f} + \mathbf{A}^{\mathbf{T}}\boldsymbol{\lambda}\mathbf{c} \tag{3-60}$$

From equation (3-60), the penalty method converts the geometric nonlinearity into material nonlinearity by modifying the potential energy term. The penalty method introduces a penalty term into the system potential energy formula as expressed in (3-58). If the penalty number λ is equal to zero, then equation (3-58) becomes identical to equation (3-55). The penalty number λ is typically a very large number such that a large cost is added to the objective function when the solution points lie outside of the original feasible region. Thus by minimizing the modified potential energy accounting for the penalty term, the ring displacement is found and the constraint is satisfied. The recommended range for the penalty number λ found in literature [52] is:

$$\boldsymbol{\lambda} = \boldsymbol{\lambda}_{\mathbf{r}}\, \mathbf{max}[\mathbf{diag}(\mathbf{K})]\,;\ \boldsymbol{\lambda}_{\mathbf{r}} \in [\mathbf{10^4}, \mathbf{10^6}] \tag{3-61}$$

A flowchart for solving the ring-cylinder bore contact problem using penalty method can be found in Figure 3-7.

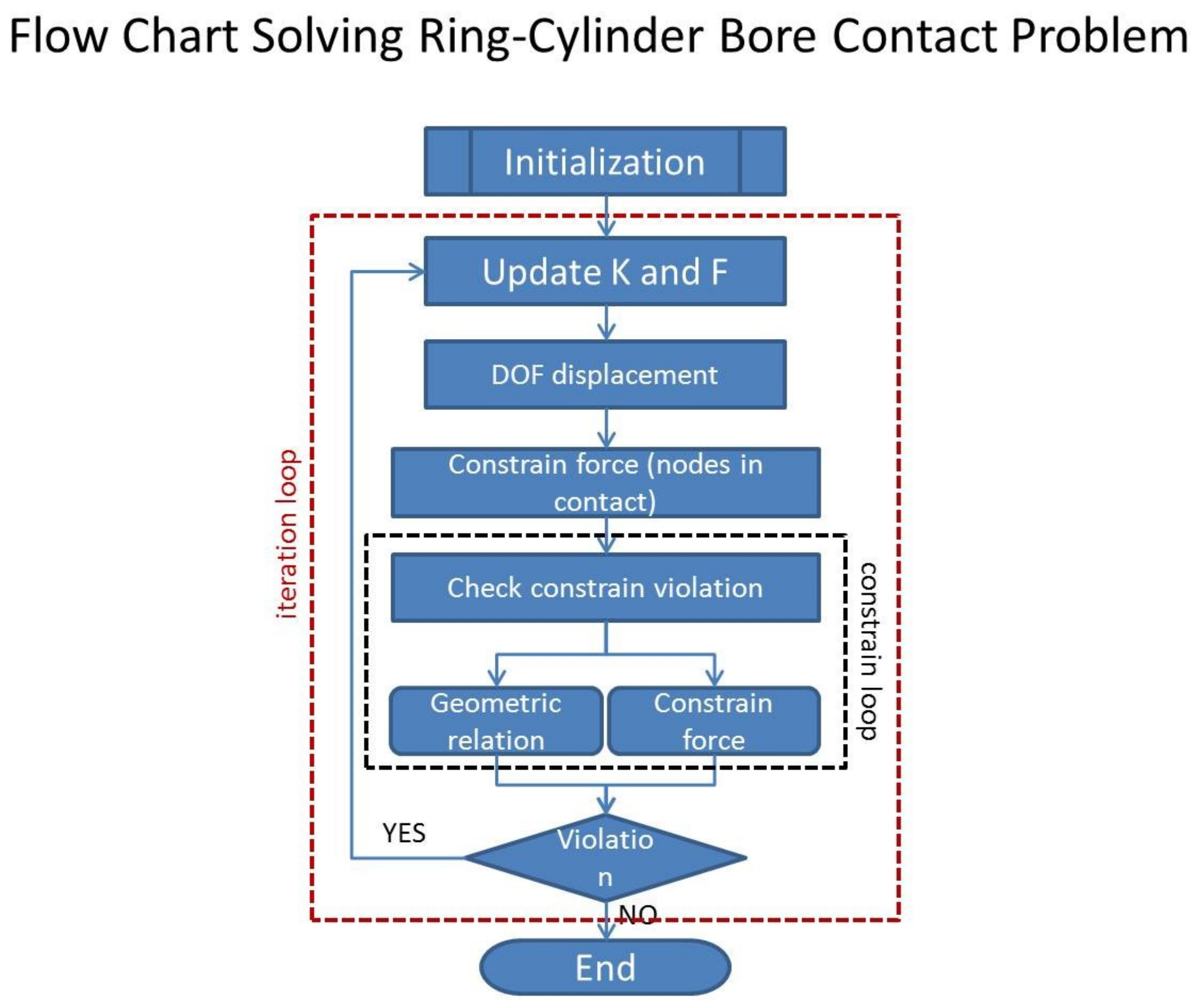

Figure 3-7 Flow chart solving ring-cylinder bore contact

In this approach, geometric relations and constraint force directions are used to check the constraint violation during the penalty method iteration. The steps are outlined as:

I. Build/update the global stiffness matrix and force vector.

II. Calculate the nodal displacement under the current force condition.

III. Calculate the constraint force for the nodes that are in contact with the cylinder bore.

IV. Check the constraint violation: for the nodes not under constraint force, they should not move beyond the cylinder bore surface; for the nodes under constraint force, the constraint force direction should be inward, pointing to the center of cylinder bore.

V. If no constraint mentioned in step 4 is violated, the stationary state of the ring is found; otherwise, return to step 1 until all the constraints are satisfied.

The nodes used for the constraint violation check are the upper and lower ones at the specified cross-sections on the ring front face as shown in Figure 3-8. If the upper and lower nodes satisfy the constraint criterion, it is assumed the corresponding cross-section is also satisfied.

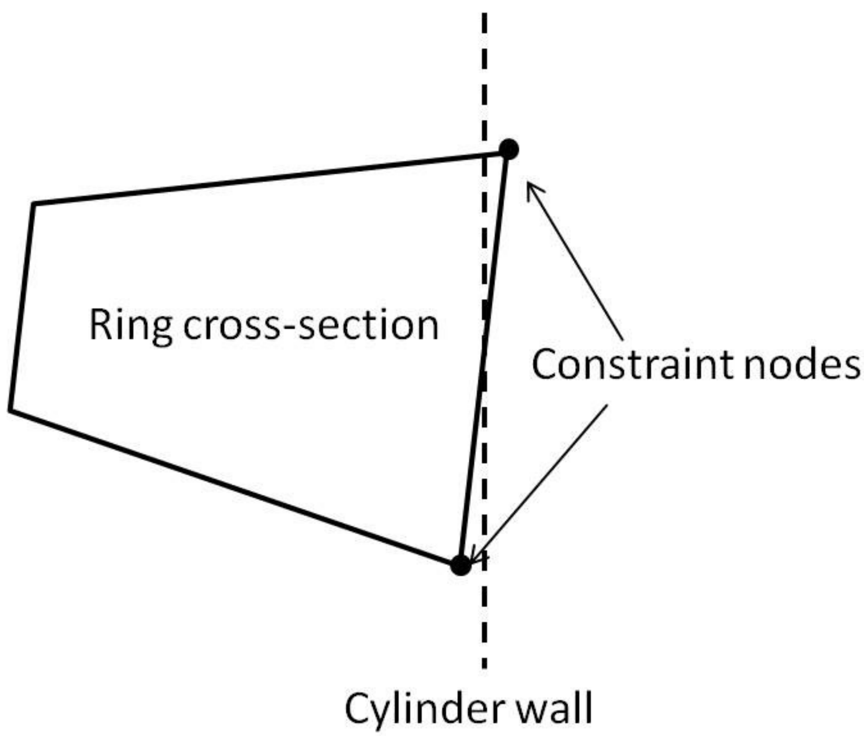

Figure 3-8 Constrained Nodes on One Cross-Section

For a ring with a symmetric cross-section under uniformly distributed temperature, the upper and lower constraint forces should be equal in magnitude and in the same direction. Different constraint forces develop when a twisting moment on the ring occurs, due to cross-section, asymmetry, temperature gradient, non-uniform gas pressure, etc.

One challenge with the penalty method is to identify the correct contact pair on the two surfaces: the constrained nodes on the ring front face and the corresponding infinitesimal constraint surface on the cylinder wall. For the constrained nodes on the ring, the locations at the ring deformed state are not known. For the constraint surface, either for a circular bore or a distorted bore with a known distortion pattern, the geometry and the normal direction of any infinitesimal surface can be found. The unknown is which infinitesimal constraint surface will be in contact with the constrained nodes after the ring deformation.

In order to overcome the difficulties in identifying the contact pairs, a force release approach is adopted by initially applying a pulling force at the ring tips as shown in Figure 3-9. The approach can be considered as the reverse process of removing the ring from the piston with a ring clamp. The direction of the initial force is along the line that connects the ring tips and its magnitude should be chosen with care. The reason is that the ring under this force is desirable to be as close to the constrained bore surface as possible. One simple criterion in choosing the initial force is that under the initial pulling force, all nodes at the ring front face should not move beyond the constraint bore surface and at the same time, the ring end gap should be greater or equal to zero, so that no overlap occurs at the ring tips. The finite element model can be used to find the appropriate initial force.

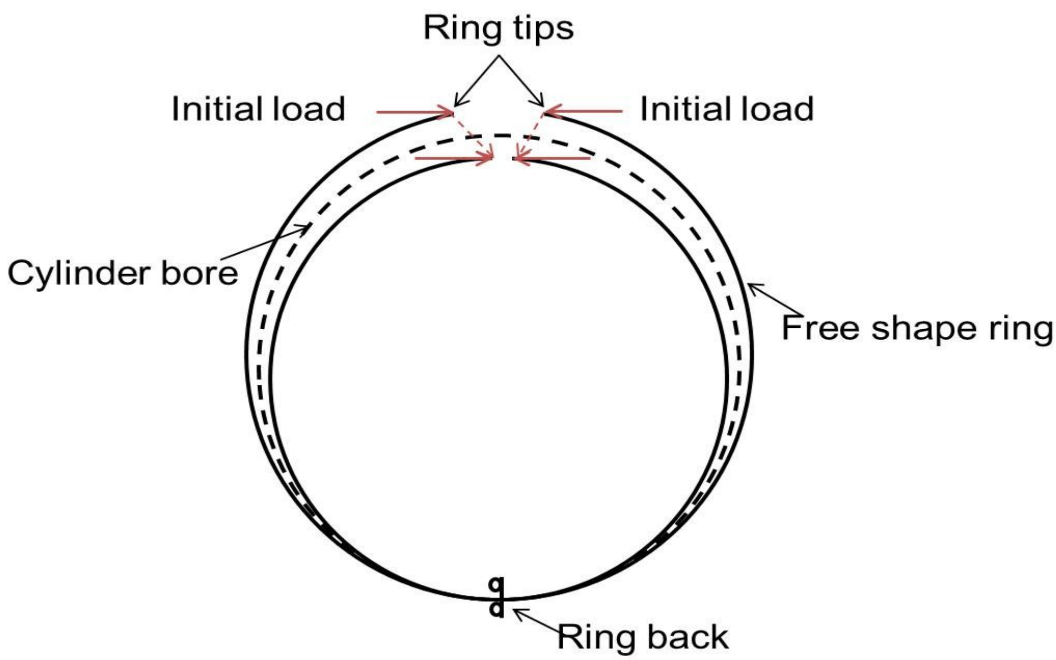

Figure 3-9 Initial forces at ring tips

The purpose of the initial force is only to assist in finding the infinitesimal constraint surface on the cylinder liner that restrains the corresponding ring node. This force must vanish eventually due to its fictional nature, and it needs to be released gradually to guarantee the convergence of the constraint infinitesimal surface. In this work, the force is halved at each step until the force difference between the two consecutive steps is less than 0.1 N. And in each step, the penalty method approach is employed to obtain the constraint pair in current step.

The matrix A described previously denotes the points that constrain the ring along the circumference. The constraint point can be considered that there is a very stiff spring which can only be compressed and not tension is allowed. The direction of the spring placement is always along the cylinder bore radial direction.

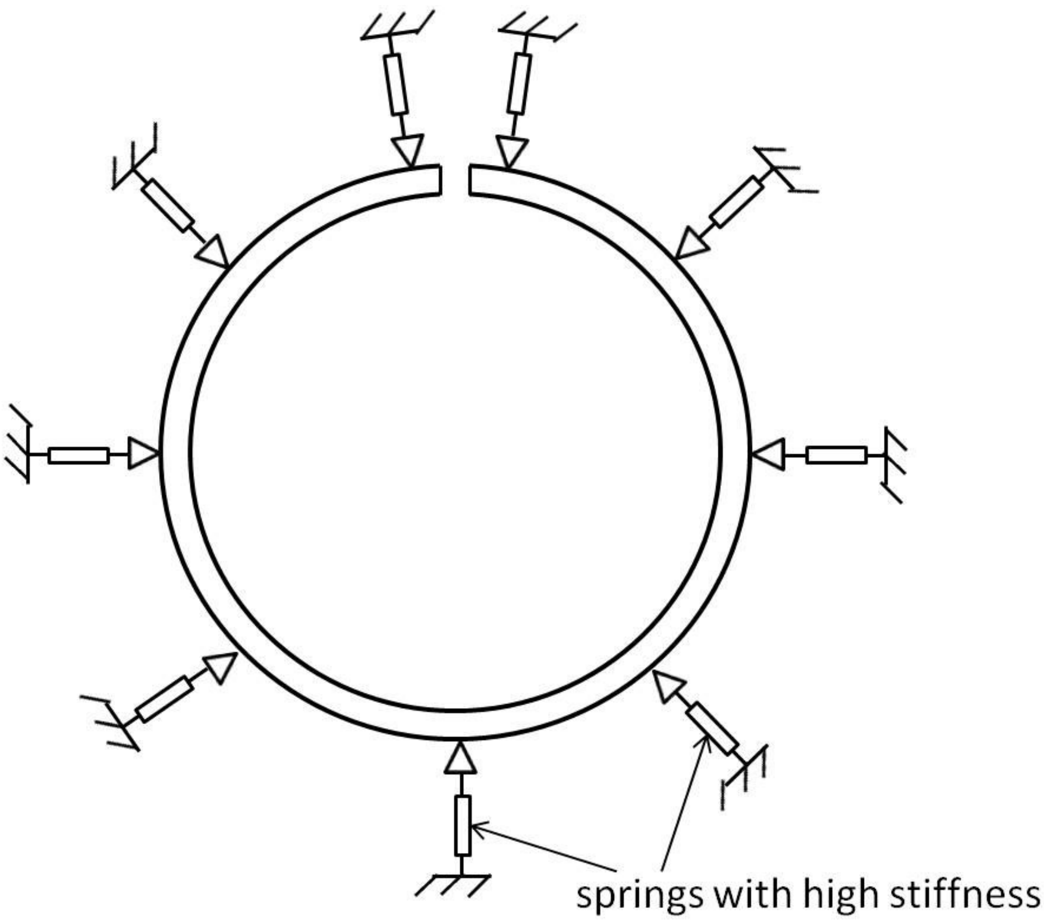

Figure 3-10 High stiffness springs at contact locations

The penalty applied to the ring can be considered as defining the stiffness of the spring that pushes the ring back into bore shape (Figure 3-10).

The gap vector $\mathbf{c}$ defines the displacement a ring node should undergo from its free state to deformed condition (Figure 3-11). The gap $\mathbf{c}$ does not necessarily along the cylinder bore radial direction. This is because when the ring is pushed into the bore shape, the nodes not only have radial displacement, but also a tangential displacement.

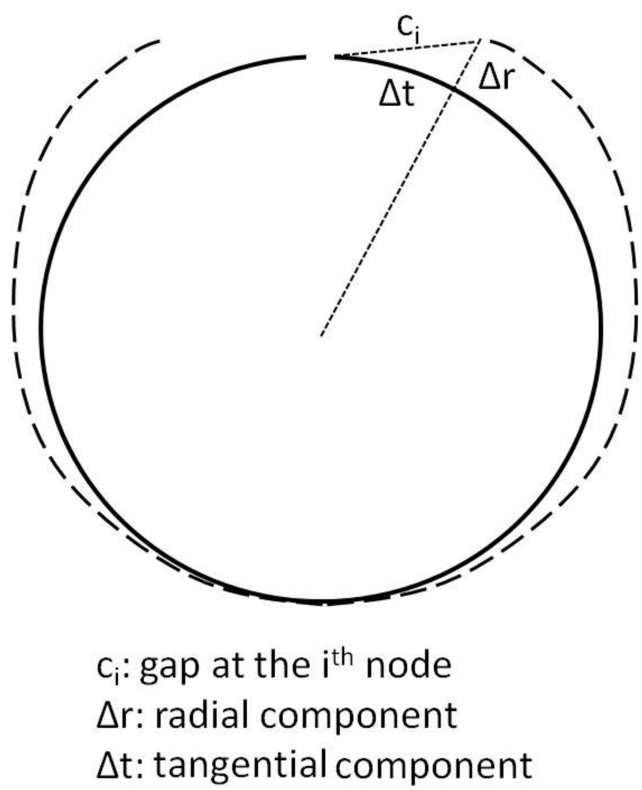

Figure 3-11 Gap vector between free shape and deformed ring

The flowchart using the force release method is shown in Figure 3-12. The “Contact Analysis” part here refers to the procedures described in Figure 3-7.

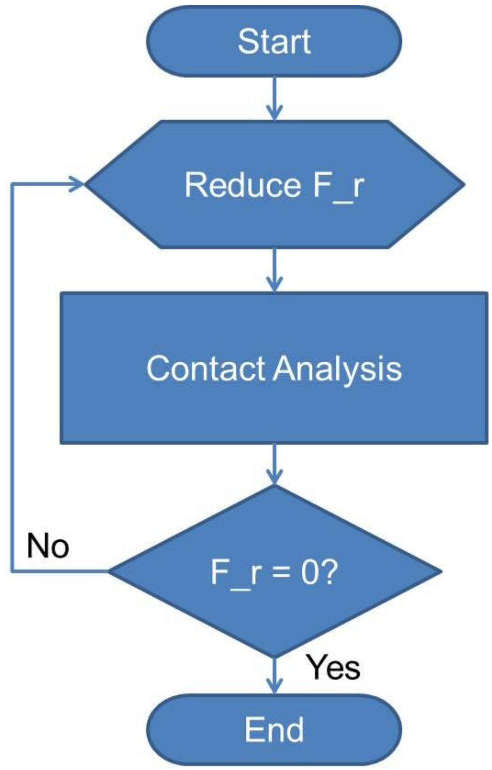

Figure 3-12 Flow chart of force release method

As the nature of the constraint force, it cannot be calculated directly. Instead, it can be obtained knowing other applied force conditions and the ring condition. Thus, known the displacement q, the constraint forces are found in the following way:

$$\mathbf{F}_c = \mathbf{A}^{\mathbf{T}}\boldsymbol{\lambda}\mathbf{c} - (\mathbf{A}^{\mathbf{T}}\boldsymbol{\lambda}\mathbf{A})\mathbf{q} \tag{3-62}$$

This constraint force satisfies the equation:

$$\mathbf{Kq} = \mathbf{f} + \mathbf{F}_c \tag{3-63}$$

which is the state with minimum potential energy of the ring under the prescribed constraints.

3.2.4 Ring-Groove Side Contact Modeling

The interaction between the ring-groove side interface is becoming a more time limiting factor for piston ring application, thus needs to be considered in modeling. Similar to constructing the ring-cylinder bore contact formulation, the ring-groove side contact can also be considered. In addition to the constraints in the radial direction only shown in $\mathbf{r_i} \leq \mathbf{R_B}$ **(3-56**), the constraints in the axial direction between the ring and groove sides should also be included. This yields:

$$\mathbf{r_i} \leq \mathbf{R_B}, \mathbf{h_T} \leq \mathbf{G_T} \text{ and } \mathbf{h_B} \geq \mathbf{G_B} \tag{3-64}$$

In this case, r_i is still the outer radius at the ring i^{th} cross-section and $\mathrm{R_B}$ is the cylinder liner radius of curvature. And h_T and h_B are the z-coordinates of the ring top and bottom sides respectively; while G_T and G_B are the coordinates of the groove top and bottom sides respectively.

The constraints require that the ring outer radius should stay in contact (for the "=" case) or within (for the "<") case the cylinder wall surface. In addition, the ring top side should stay in contact with the groove top side (for $h_T = G_T$ case) if it is in contact or below the groove top side (for $h_T < G_T$ case) if it is not in contact. Similarly, the ring bottom side should stay in contact with the groove bottom side (for $h_B = G_B$ case) if it is in contact or above the groove bottom side (for $h_B > G_B$ case) if it is not in contact.

Figure 3-13 shows the constraints at the ring front face, top and bottom sides at one cross-section. In this case shown in the figure, the two nodes at the ring front face top and bottom edge are constrained in the radial direction by the cylinder wall surface. And the four corner nodes, as numbered 1, 2, 3 and 4, are constrained in the axial direction by the groove sides. It is not necessary the nodes constrained in the radial direction coincide with the nodes constrained in the axial direction. For example, in most cases, the groove side has a short radial length such that it would not constrain the ring at its outside bottom corner (node 2 in this case).

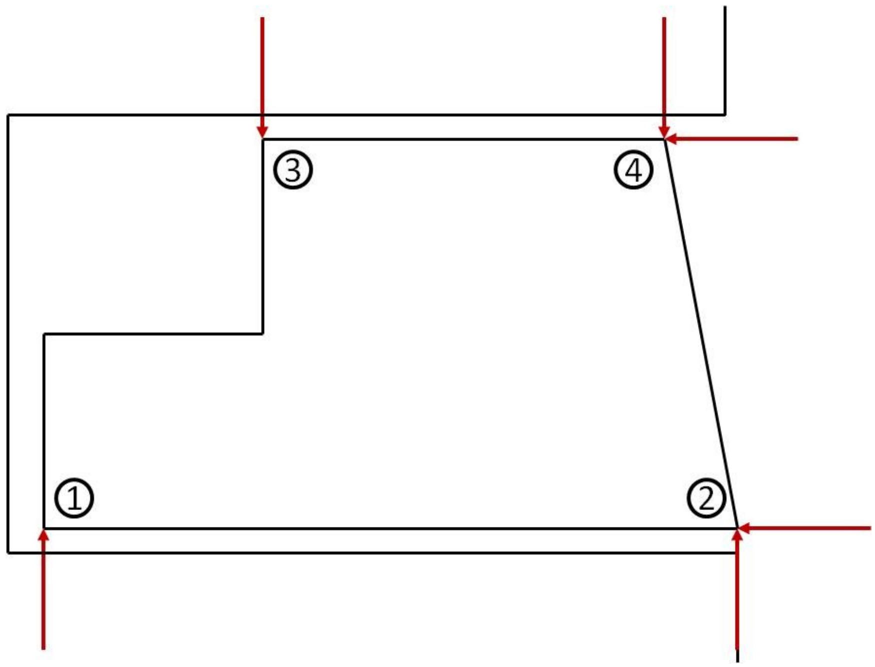

Figure 3-13 Constraints at ring face and ring sides

3.2.5 Result of Ring-Cylinder Bore Contact

When the free state ring is installed into the cylinder liner, the ring is constrained at its front face by the cylinder wall. Every point on the ring front face needs to be tracked whether it is in contact with the cylinder wall or not. However, due to the computation time and resource, it is not possible with the existing computation tool. And the most important thing is how the contact force/pressure distributes along the ring circumference. Thus, in this study, the ring is specified constrained at thirteen different cross-section locations along the circumference. The middle constraint locates at the ring back front face. Other constraints are symmetric about the ring back and distribute with an increment of about 30°.

The free shape ring mesh and the deformed ring mesh without temperature compensation are shown in Figure 3-14.

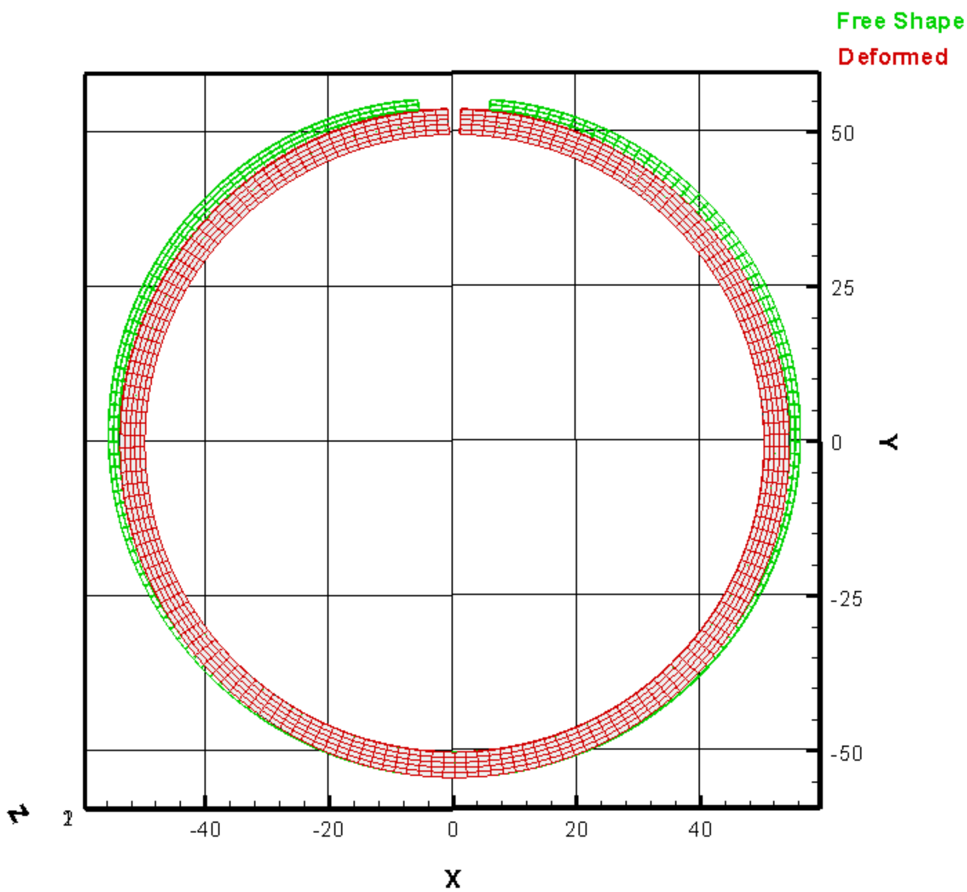

Figure 3-14 Free shape and deformed ring meshes

The green mesh in Figure 3-14 represents the free shape ring while the red mesh represents the deformed ring shape under the cylinder bore constraints without temperature compensation. It is obvious that the ring is pushed inward from its free state. The constraint forces that push the ring to its deformed position are shown in Figure 3-15. The blue and red bars represent the constraint forces at a certain circumference location at the upper and lower corners at ring face. And the green and purple dots show the separation gaps between the ring face and the cylinder bore.

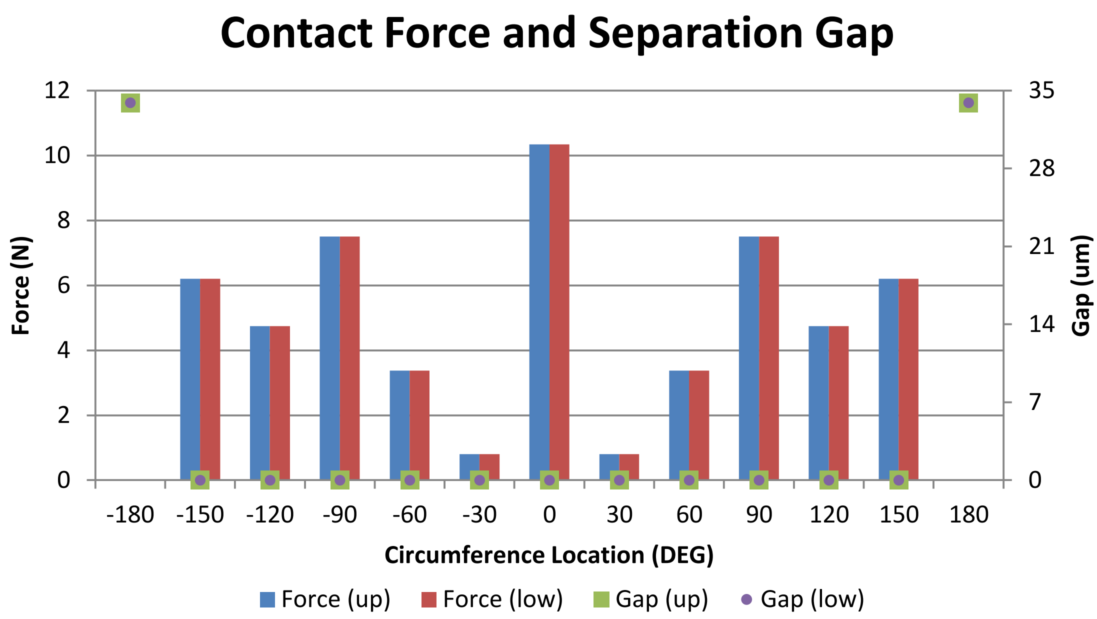

Figure 3-15 Constraint force and separation gap

From Figure 3-15, it is found that the two contact forces at the same cross-section are identical since the ring has a symmetric cross-section and there is no twisting moment on the ring. The plot also shows that the constraint force at the ring back is the highest. At the cross-sections approximately 30 degrees away from the ring back, the lowest constraint forces are found for the sections that are in contact against the cylinder wall. The constraint forces at the ring tips vanish such that the ring separates from the cylinder wall in its front face at its two tips. The separation gap is defined as the radial distance between the cylinder wall ID and the ring tip OD. A 34 μm separation gap is found for this specific ring from the FEA model. Details of the contact forces and the separation gaps are listed in Table 3-1.

Table 3-1 Constraint forces and separation gaps

Location	0°	30°	60°	90°	120°	150°	~180°
Force, Up (N)	10.3	0.8	3.4	7.5	4.7	6.2	0.0
Force, Low (N)	10.3	0.8	3.4	7.5	4.7	6.2	0.0
Gap, Up (μm)	0	0	0	0	0	0	34
Gap, Low (μm)	0	0	0	0	0	0	34

3.2.6 Application on EcoMotors 2-Stroke Engine

The 3D ring FEA model is applied to EcoMotors 2-Stroke opposite piston opposite cylinder (OPOC) engine for friction analysis. The contact pressure distributions between the ring and bridge surfaces were calculated. The ring was examined for three different boundary conditions: ring gap at the middle of bridge; ring gap at the middle of port; and one ring tip at bridge and the other in the port. In each of the boundary condition, two cases were analyzed: the first case assumed the constraint forces are at the middle of the bridges and the second case assumed the constraint forces are at the bridge edges.

The EcoMotors OPOC engine cylinder is shown in Figure 3-16.

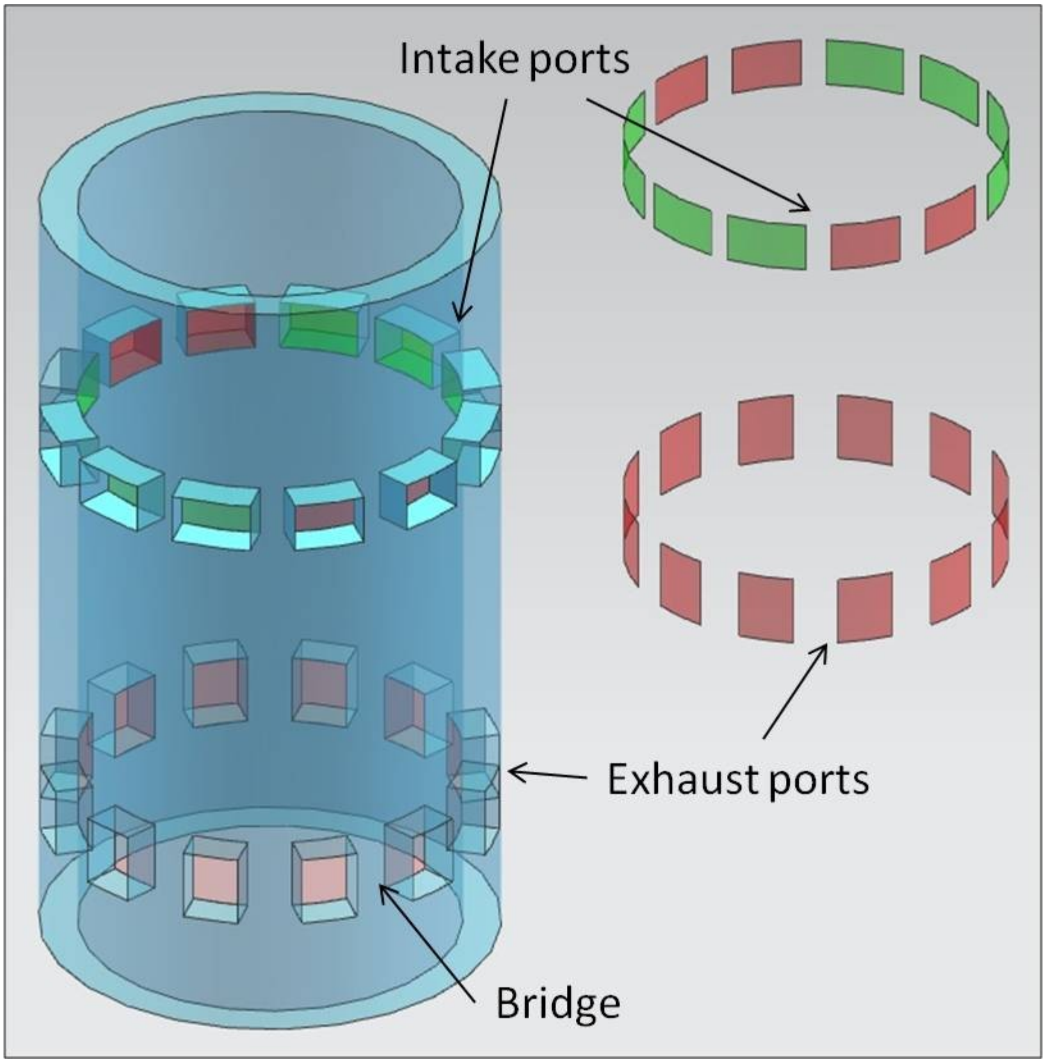

Figure 3-16 EcoMotors OPOC engine geometry showing intake and exhaust ports

The bridge is defined as the cylinder wall between two adjacent ports. The ring-bridge contact study only focuses on the contact at the exhaust ports side. However, the contact between the ring and bridge at the intake ports side can be analyzed very similar to that of the exhaust side. The three boundary conditions discussed in this study are:

1. Ring gap is at the middle of bridge (both ring tips are in the bridge area, BC1).
2. Ring gap is at the middle of port (both ring tips are in the port area, BC2).

3. One tip is at the bridge area and the other tip is in the port area (BC3).

These three boundary conditions are shown in Figure 3-17.

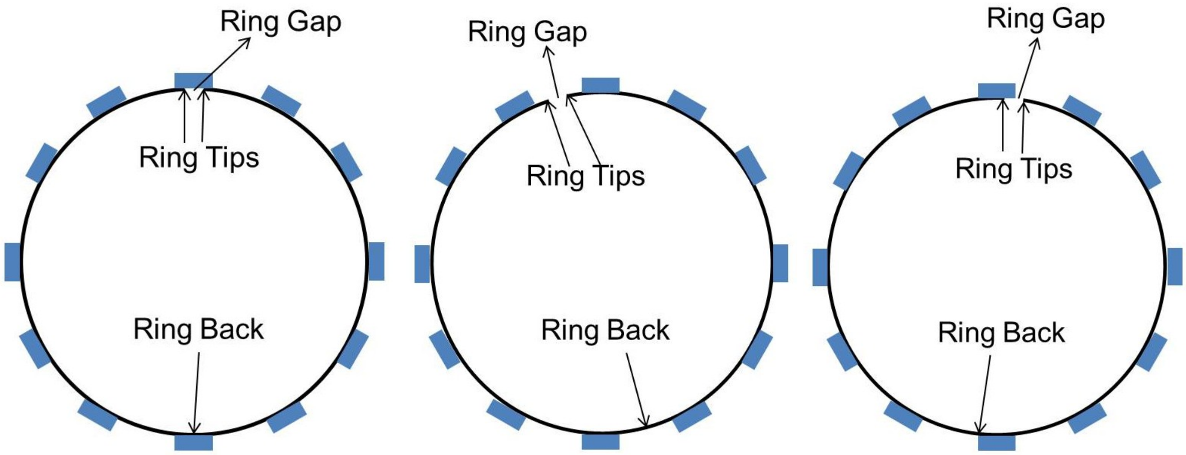

1. Ring gap at middle of bridge 2. Ring gap at middle of port 3. One tip at bridge and one at port

Figure 3-17 Boundary condition for ring-bridge contact

In each of the three above boundary conditions shown in Figure 3-17, the ring-bridge contact was analyzed with two constraint cases. The two cases have different locations of the constraint force applied on the bridge. One case is assuming the constraint force is applying at the middle of the bridge (CBM); while the other case has two constraint forces at the two edges of each bridge (CBE). These constraint conditions are illustrated in Figure 3-18.

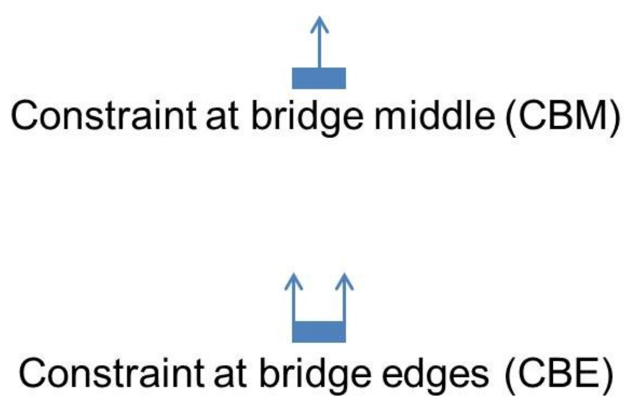

Figure 3-18 Constraint force conditions

With the constraint forces solved from the finite element analysis simulation, the contact pressure distribution on each bridge can be obtained using a force-pressure balance correlation knowing the ring-bridge contact area. The average pressure on a bridge is calculated first as the constraint force on the bridge divided by the ring-bridge contact area. It is assumed that the pressure distributes linearly on the bridge from one edge to the other. Figure 3-19 shows how the pressure distribution on the bridge is calculated for both constraint force at middle of bridge and at bridge edges cases. The method leads to that the pressure at the middle of the bridge is always equal to the average pressure. The pressures away from the middle of the bridge follow the rule described below. For the constraint at the middle of bridge case, the bridge local pressure is related to the position between the ring node and the bridge surface. A ring node here is a node of a ring mesh element located on the ring front face. As forces which represent constraints are applied to the free ring, if a node on the ring is located beyond a curved bridge that represents the bridge surface, the pressure will be high since the ring face needs to be pushed back to the ring-bridge interface; while if a node locates within the bridge radius, the pressure at this location is low as there is no contact at that point. The distances between the bridge and the ring points away from the bridge middle are very small. For the constraints at bridge edges case, the linearly distributed pressure is calculated based on the two constraint forces at the bridge edges. If the constraint force is high on one bridge edge, the pressure should also be high near this bridge edge; and if the constraint force is low at one bridge edge, the pressure would also be low.

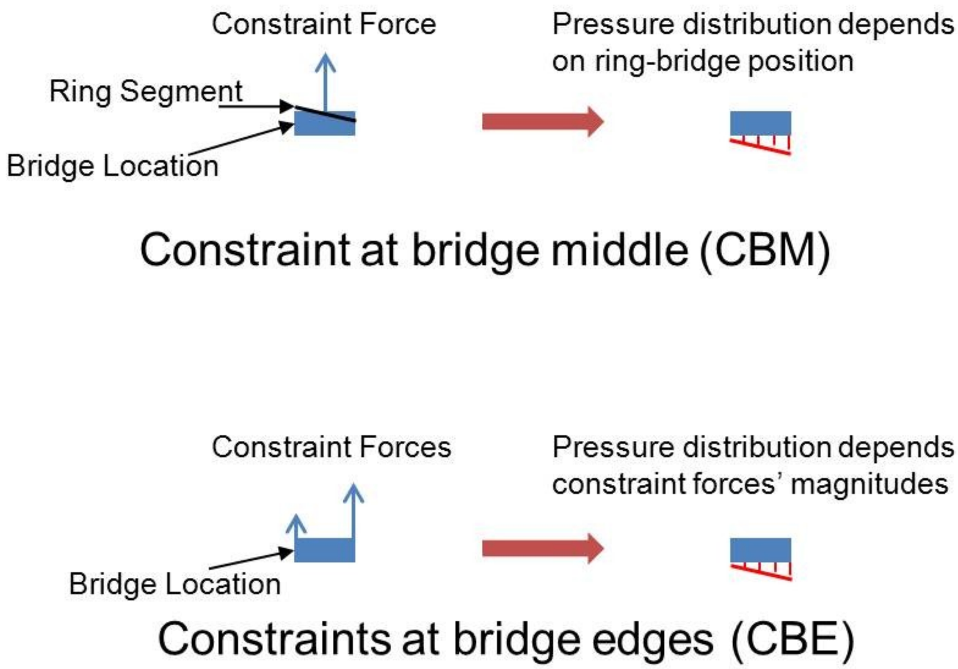

Figure 3-19 Bridge contact pressure distribution calculation

The pressure distribution for the ring gap at the middle of bridge boundary condition case (BC1) is shown in Figure 3-20.

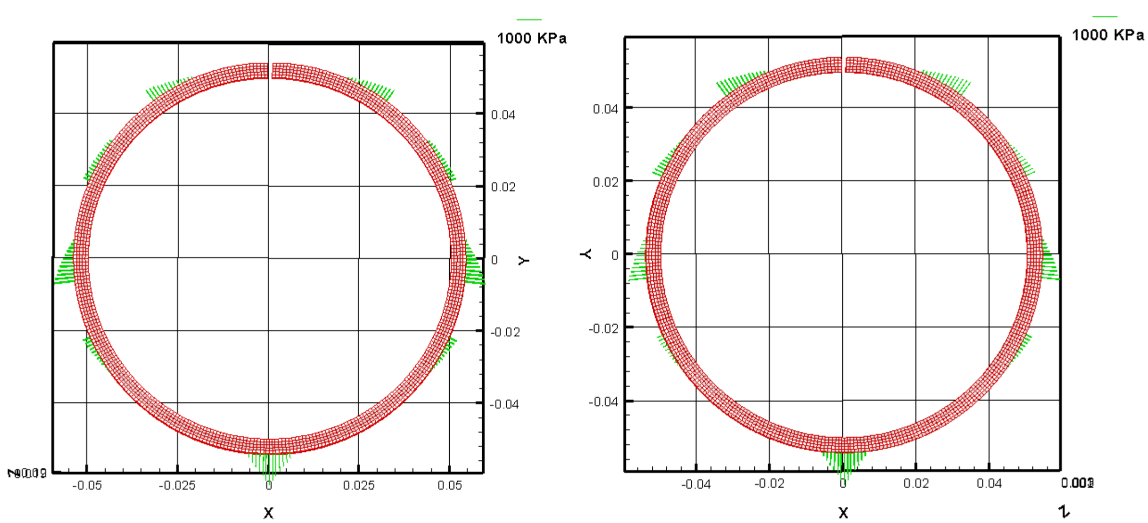

a. Constraint at middle of bridge

b. Constraints at bridge edges

Figure 3-20 Pressure distribution for ring gap at middle of bridge case

From Figure 3-20 (a) and (b), the contact pressure distributions for the two cases showed good agreement not only in the pressure magnitude, but also the pressure distribution pattern on each bridge. From the two plots, the bridge in contact with the ring back shows the highest pressure. No pressure was found for the bridge at 150° and 210° locations, which means the ring is not in contact with the bridge at these locations, or at least the contact pressures are supposed to be very low due to the limitation of the ring coordinate measurement tolerance. The ring tips are not in contact with the bridge as no pressure was observed at the bridge constraining the ring tips.

Similarly, the pressure distributions for the ring gap at the middle of port (BC2) are shown in Figure 3-21.

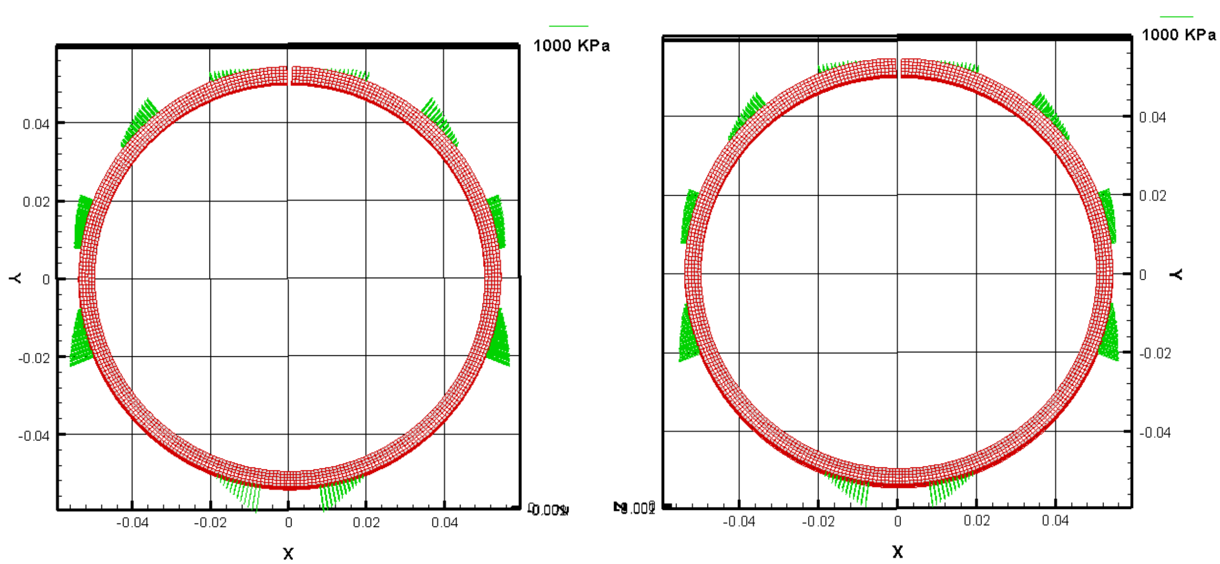

a. Constraint at middle of bridge   b. Constraints at bridge edges

Figure 3-21 Pressure distribution for ring gap at middle of port case

From Figure 3-21 (a) and (b), the pressure distribution configurations of the two cases also show good agreement too. The highest pressures at the bridge edge locating at 165° and 195°

(closest to the ring back) are 668 KPa for the CBM case and 600 KPa for the CBE case respectively. In addition, the bridges at 135° and 225° did not show contact with the ring.

The one tip at the bridge and one tip in the port boundary condition case (BC3) results are shown in Figure 3-22 (a) and (b) for the constraint at middle of bridge and bridge edges respectively. In Figure 3-22, the right tip is in the port while the left tip is at the bridge.

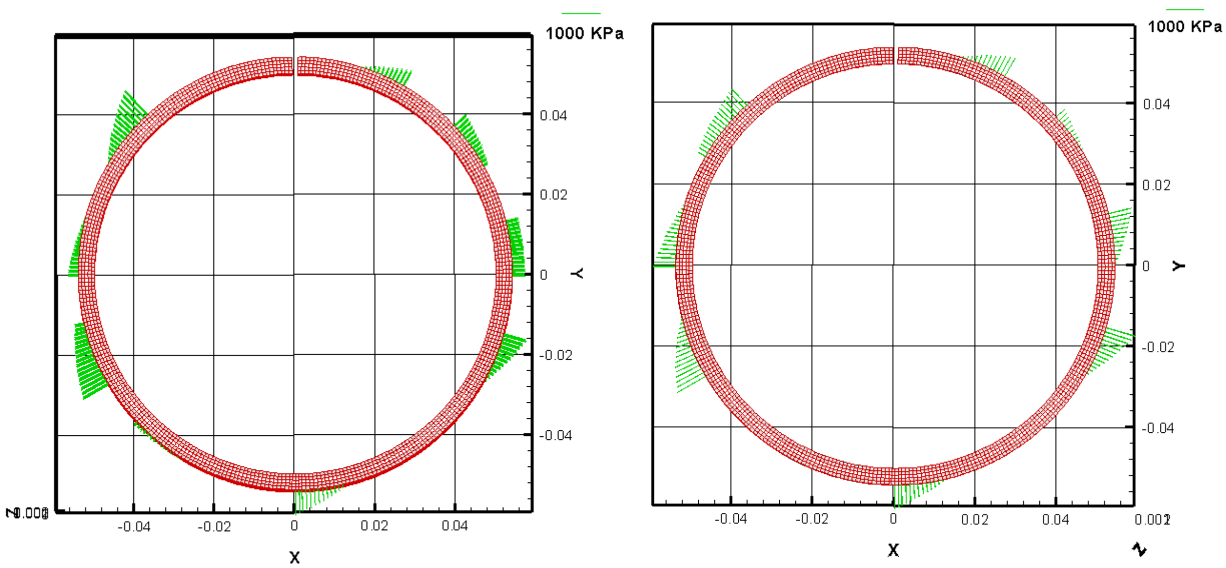

a. Constraint at middle of bridge

b. Constraints at bridge edges

Figure 3-22 Pressure distribution for one tip at bridge and one tip in port case

Slight difference in pressure magnitude can be found from Figure 3-22. For the bridge locating at 323.4°, the constraint at middle of bridge (CBM) case shows the contact pressure drops to zero at one edge, while from the constraints at bridge edges (CBE) case, it does not vanish on the same bridge edge. A similar difference is also found for the bridge locating at 83.4°. Other than that, good agreement is found between these two results. The highest pressures at the ring back are 603 KPa for the CBM case and 634 KPa for the CBE case respectively.

3.2.6 Result of Ring-Cylinder Bore-Groove Side Contact

Another example is given in this section for ring-cylinder bore-groove side contact using a scraper ring. The scraper ring has a taper face and cut-off at the ring inner upper corner, which promotes positive twist when installing the ring into the piston groove. The cross-section of the scraper ring is shown in Figure 3-23.

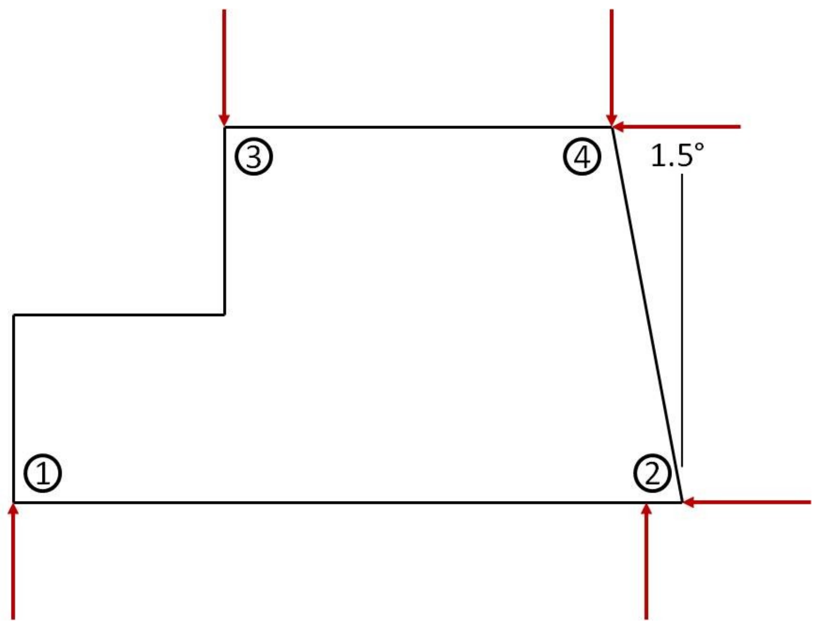

Figure 3-23 Constraints on ring cross-section

From Figure 3-23, four nodes of the cross-section at a given circumference location are considered for the ring-piston groove side interaction and are numbered as node 1, node 2, node 3 and node 4 as shown. These four nodes are constrained by the groove in the axial direction. This means node 1 and 2 should stay in contact or above the groove bottom side; while node 3 and 4 should stay in contact or below the groove top side. Two nodes on the ring front face are constrained by the cylinder bore in the radial direction, at the front face top and bottom edges respectively. The groove has zero uptilt angle at its top and bottom sides. The nominal clearance between the groove and ring axial thicknesses is 0.1 mm.

The main parameters describing the ring are listed in Table 3-2.

Table 3-2 Main parameters for the ring

Ring Material	Steel
Modulus of Elasticity	200.0 GPa
Poisson's Ratio	0.3
Cylinder Bore Diameter	108.0 mm
Coefficient of Thermal Expansion	13.0E-6 /°C
Thermal Conductivity	45 W/mK
Ring/Gas Convective Coefficient	25 W/m^2K
Ring/Oil Film Convective Coefficient	100 W/m^2K

The scraper ring is a ring with negative ovality. The ring also has a positive static twist due to the cut-off at the inner top corner.

The constraint locations along the ring circumference are equally spaced with about 30° from one butt end to the other. The number of constraint locations is found to be able to represent the ring/cylinder liner/groove side contact force/pressure distribution pattern and also save calculation time. Increasing constraint locations will increase computation time exponentially; while decreasing the constraint locations may result in the contact force/pressure pattern not being able well represented.

The deformed ring shape is shown in Figure 3-24 after installed into the cylinder liner and piston groove. The displacement in the z-direction (axial direction) is amplified by 100 times in order to illustrate the ring deformation distinctly.

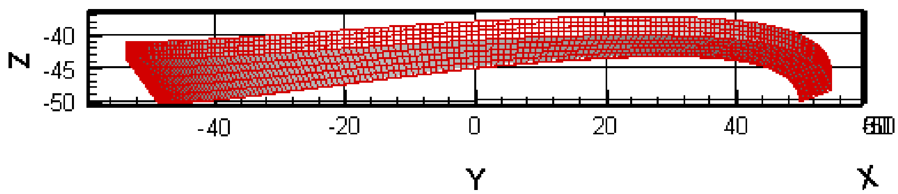

Figure 3-24 Deformed ring shape after installed into the cylinder liner and piston groove

In this case, the ring back and ring butt ends are in contact with the groove bottom side; while the ring touches the groove top side at about 60° from the end gap (120° from the ring back). The constraint forces between the ring and the piston groove sides are important since it dictates the contact pattern which will affect the ring-groove side wear eventually. Table 3-3 lists the constraint forces between the ring and piston groove for the scraper ring at four constrained node locations shown in Figure 3-23.

Table 3-3 Constraint forces between ring and groove side

Force (N)	0°	30°	60°	90°	120°	150°	~180°
ND_1	0.49	0.0	0.0	0.0	0.0	0.0	1.51
ND_2	0.0	0.0	0.0	0.0	0.0	0.0	0.0
ND_3	0.0	0.0	0.0	0.0	0.0	0.0	0.0
ND_4	0.0	0.0	0.0	0.0	-2.0	0.0	0.0

Table 3-3 shows that for the cross-section that are in contact with the groove bottom (at ring back and ring end), the contact occurs at the lower inner node (node 1 in Figure 3-23). And for the cross-section that touches the groove top, the contact occurs at the upper outer node (node 4 in Figure 3-23). This contact pattern is due to the fact that the ring twists positively, which results in a two-point contact between the ring and the groove sides.

In addition to the axial displacement variance, the ring twist angle also varies along the circumference shown in Figure 3-25 for one half of the ring. The other half is symmetric at the ring back.

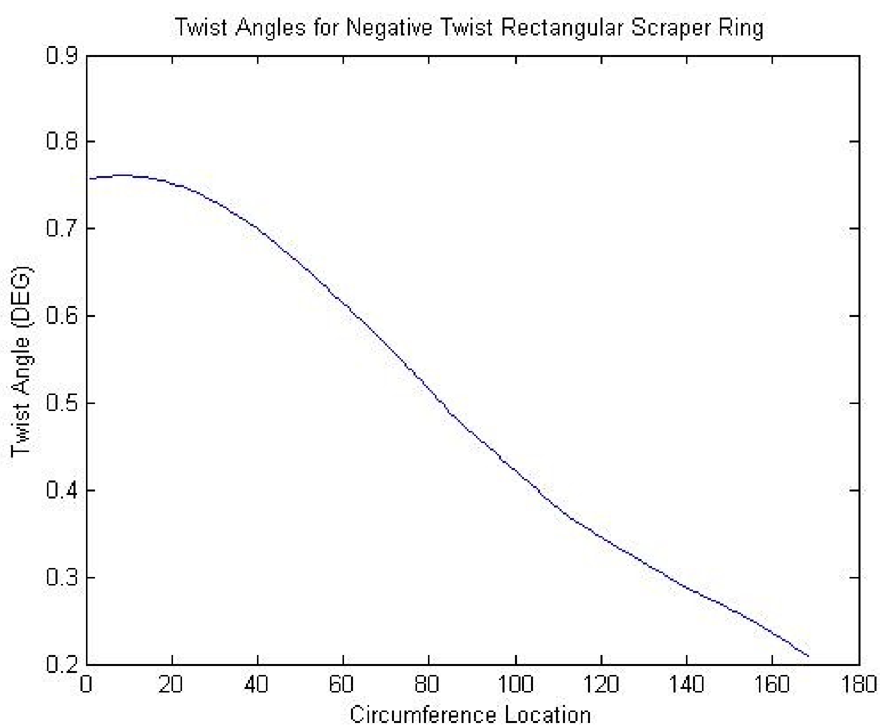

Figure 3-25 Twist angle along ring circumference

The twist angle plot shows that the scraper ring twists positively as expected from the cut-off at the ring inner top corner. However, the magnitude of the twist decreases from the ring back to the ring end gap. The maximum positive twist occurs near the ring back at less than 0.8°. And the minimum positive twist is found at the ring ends with slightly higher than 0.2°.

Chapter 4 RING THERMAL LOAD INFLUENCE

4.1 Introduction

Piston rings are subject to different temperature conditions depending on engine operating conditions: during engine start-up, the thermal load on the piston rings is relatively low; after engine warm-up, piston rings are usually under high temperature condition, especially the top compression ring, which is exposed directly to the combusted gases in the combustion chamber. Thus, besides many other functions including gas and lubrication oil control, the piston ring is also responsible to dissipate heat from the piston to the cylinder liner, which is cooled by coolant fluid, in order to reduce the piston temperature.

The thermal load on the piston ring is believed to have an important impact on both functions mentioned above. As a result, the piston ring's conformability and the contact force/pressure can alter significantly between the low and high temperature conditions. This thermal effect is especially essential for the top compression ring, which is typically under the highest thermal load. Thus, a temperature distribution analysis for the ring is necessary for the ring thermal deformation as well as the ring-cylinder liner-groove contact analysis.

As claimed by Mierbach A., et al [54], 31% of heat flow from the piston is through the ring pack for pistons with cooling channels. For pistons that do not have internal cooling channels, this ring pack heat flow value becomes 44% (Figure 4-1).

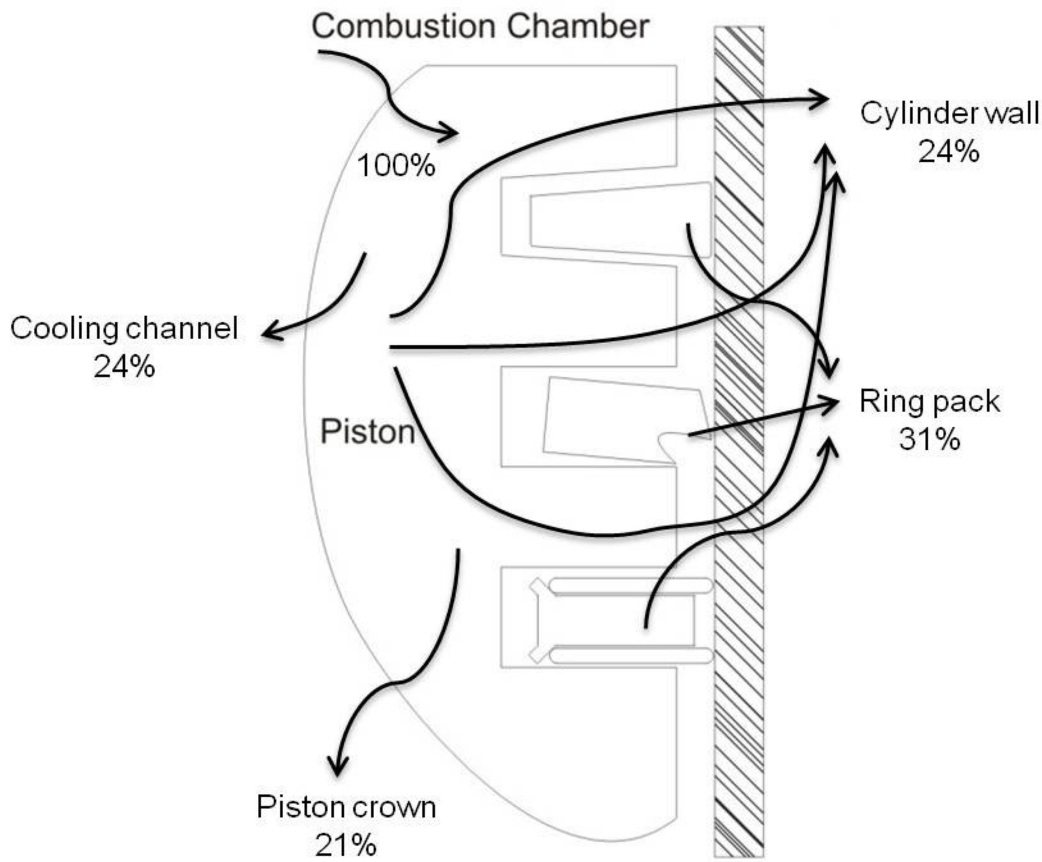

Figure 4-1 Heat flow through the piston

The proportional distribution of the possible routs of piston heat flow for a high-duty diesel engine is shown in Table 4-1.

Table 4-1 Piston heat flow proportional distribution

Path of heat flow	with piston cooling	without piston cooling
Piston rings	31%	44%
Piston – cylinder	24%	29%
Piston crown	21%	27%
Cooling channel	24%	NA

It is known that the piston rings play significant roles regarding dissipating piston heat. The consideration of ring thermal load becomes necessary in piston ring design. Due to the high temperature difference between the cold and hot conditions, the ring end gap size needs to be optimized. Small end gap is desired regarding to blowby control. However, the size of ring end gap should also compensate the thermal expansion. Otherwise, the ring ends could collide, which is recognized as “ring end gap butting”. In addition to the ring temperature difference between the cold and hot conditions, in order for the piston ring to conduct heat, a temperature gradient between the ring I.D. and O.D. should exist. Therefore, the I.D. of piston ring undergoes greater thermal expansion than the O.D., depending on the thermal gradient. As a result, the ring radius of curvature alters from the cold condition, and the contact force/pressure varies as well. The temperature distribution on piston ring and the thermal load influence are discussed in this chapter.

4.2 Model Description

The 3D heat transfer problem of the piston ring can be described by the 3D heat equation below:

$$\frac{\partial T}{\partial t} - k\left(\frac{\partial^2 T}{\partial x^2} + \frac{\partial^2 T}{\partial y^2} + \frac{\partial^2 T}{\partial z^2}\right) = 0 \tag{4-1}$$

where T denotes the temperature, which is a function of three spatial variables (x, y, z) and the time variable t.

However, for a piston ring application as described in this study, the ring is moving rapidly with the piston’s motion at over 1000 RPM. Thus the rate of temperature variance at any point can be considered to be zero since heat spread process takes time and it would not be able to change much in such a short duration between engine cycles when the engine is wormed up. In this case, the temperature variation does not depend on time. Based on this assumption, the time variant problem can be simplified as a steady-state problem and the governing equation becomes:

$$\boldsymbol{k}\left(\frac{\partial^2 \boldsymbol{T}}{\partial \boldsymbol{x}^2}+\frac{\partial^2 \boldsymbol{T}}{\partial \boldsymbol{y}^2}+\frac{\partial^2 \boldsymbol{T}}{\partial \boldsymbol{z}^2}\right)=\mathbf{0} \tag{4-2}$$

with a convective boundary condition:

$$-\boldsymbol{k}\left(\frac{\partial \boldsymbol{T}}{\partial \boldsymbol{x}}\boldsymbol{n}_{\boldsymbol{x}}+\frac{\partial \boldsymbol{T}}{\partial \boldsymbol{y}}\boldsymbol{n}_{\boldsymbol{y}}+\frac{\partial \boldsymbol{T}}{\partial \boldsymbol{z}}\boldsymbol{n}_{\boldsymbol{z}}\right)-\boldsymbol{h}(\boldsymbol{T}-\boldsymbol{T}_{\infty})=\mathbf{0} \tag{4-3}$$

The ring front face is flooded with the lubrication oil film while other boundaries are exposed to gas combustion products. Convection occurs between the ring surface and its corresponding fluid. For this study, the convective boundary condition used is shown in Figure 4-2.

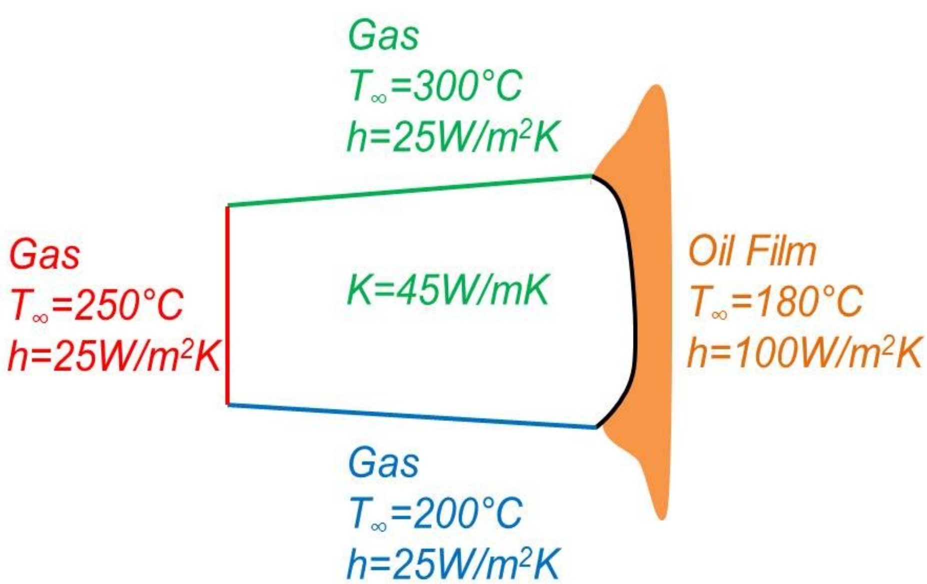

Figure 4-2 Ring cross-section heat transfer boundary conditions

In Figure 4-2, the ring has a keystone cross-section. The boundaries are the interfaces between the ring cross-section edges and the gases above, behind and below the ring as well as between the ring front face and the oil film on the cylinder liner. The example used here is a top compression ring, which is typically under much more severe thermal load condition than the second compression ring and the oil control ring since it is exposed to the hot combustion gas directly.

As piston rings moving along the axial direction with the movement of piston, the temperature on the ring front face varies since the cylinder liner temperatures vary from top to bottom. However, the boundary condition at the ring front face in this study assumes the average cylinder liner temperature.

The ring material properties and the convection coefficient between the ring and the surrounding fluids are listed in Table 4-2.

Table 4-2 Ring material properties and convection coefficients

Ring Material	Steel
Conduction Coeff.	45 W/mK
Convection Coeff. between ring and surrounding gas	25 W/m^2K
Convection Coeff. between ring face and oil film	100 W/m^2K

Finite element analysis is used again to calculate the temperature distribution for the piston ring. With the additional thermal load, the constitutive relation for an isotropic linear elastic material [55, 56] can be written as:

$$\boldsymbol{\sigma} = \boldsymbol{E\varepsilon} + \boldsymbol{\sigma_0} \tag{4-4}$$

where

$$\boldsymbol{\sigma_0} = \frac{\boldsymbol{E\alpha\Delta T}}{\mathbf{1-2\upsilon}} \begin{Bmatrix} \mathbf{1} \\ \mathbf{1} \\ \mathbf{1} \\ \mathbf{0} \\ \mathbf{0} \\ \mathbf{0} \end{Bmatrix} \tag{4-5}$$

As can be found, an additional thermal load due to temperature change is imposed onto the ring. This thermal load deforms the free state ring as can be found in the following sections.

For the simplified 2D piston ring heat transfer problem, the weighted residual form of the governing heat equation under the boundary conditions discussed previously using Galerkin's method becomes:

$$\iint \left[\boldsymbol{k} \left(\frac{\partial \omega}{\partial x}\frac{\partial T}{\partial x} + \frac{\partial \omega}{\partial y}\frac{\partial T}{\partial y} \right) \right] \boldsymbol{d}\mathbf{xdy} + \int \boldsymbol{\omega h_1 (T - T_1) d\Gamma_1} + \int \boldsymbol{\omega h_2 (T - T_2) d\Gamma_2} + \int \boldsymbol{\omega h_3 (T - T_3) d\Gamma_3} + \int \boldsymbol{\omega h_4 (T - T_4) d\Gamma_4} = \mathbf{0} \tag{4-6}$$

The above expression can be rewritten as the matrix form:

$$(\boldsymbol{K_1^e} + \boldsymbol{K_2^e})\boldsymbol{T^e} = \boldsymbol{F^e} \tag{4-7}$$

$$\boldsymbol{K_1^e} = \iint \left[\boldsymbol{k} \left(\frac{\partial N_i}{\partial x}\frac{\partial N_i}{\partial x} + \frac{\partial N_i}{\partial y}\frac{\partial N_i}{\partial y} \right) \right] \boldsymbol{d}\mathbf{xdy} \tag{4-8}$$

$$\boldsymbol{K_2^e} = \sum_{m=1}^{2} \boldsymbol{h_i} \int \boldsymbol{N_i N_j \, d\Gamma_m} \tag{4-9}$$

$$\boldsymbol{F^e} = \sum_{m=1}^{2} \int \boldsymbol{N_i d\Gamma_m} \tag{4-10}$$

4.3 Ring Heat Transfer Result

4.3.1 Ring Temperature Distribution

With the boundary condition defined in the previous section, the top compression ring cross-section temperature distribution was obtained using FEA approach and the result is shown in Figure 4-3.

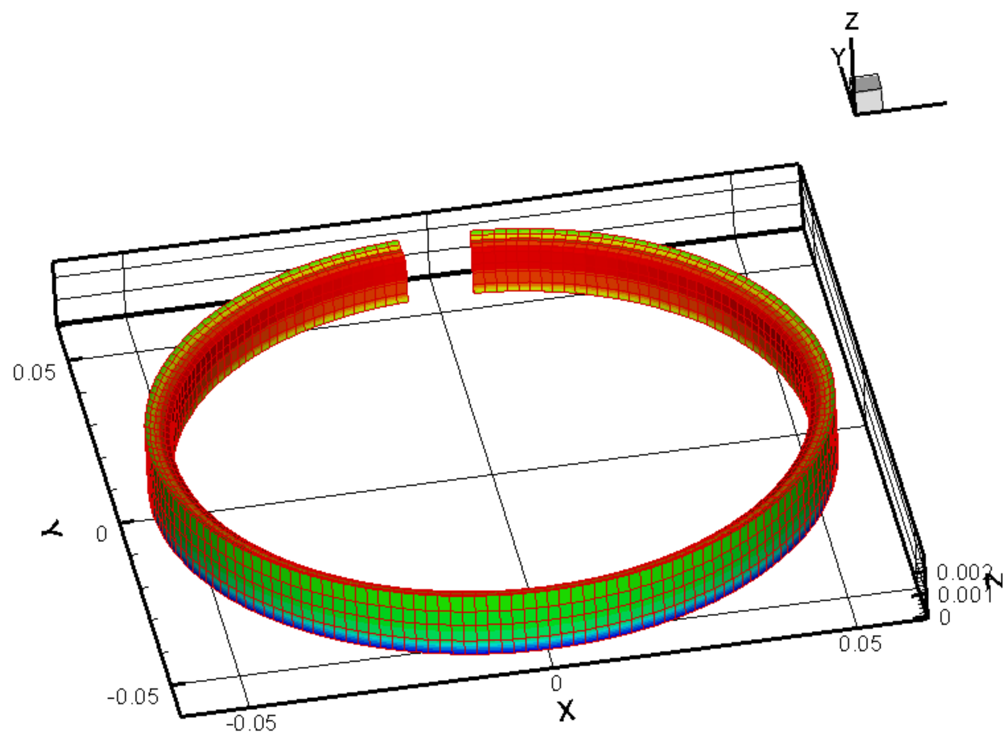

Figure 4-3 Ring temperature distribution

As the temperature distribution does not vary along the ring circumferential direction as assumed, the temperature only depends on the radial and axial location. This temperature distribution for one arbitrary cross-section can be found in Figure 4-4.

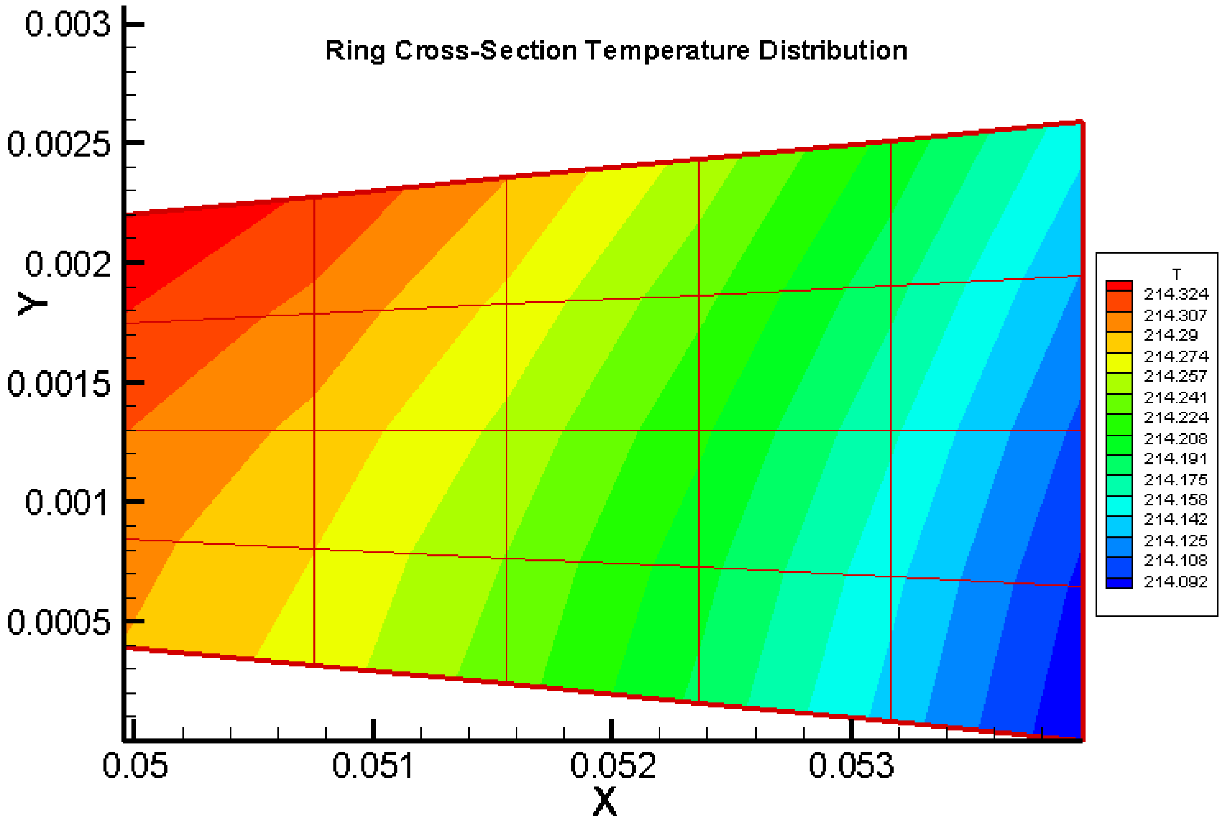

Figure 4-4 Ring cross-section temperature distribution

From Figure 4-4, the ring temperature decreases from its inner-top corner through the outer-bottom corner. However, the temperature gradient cross the ring is very small as the maximum temperature difference on the ring cross-section is within one Celsius.

The result was verified using the energy balance relationship such that the energy going into the ring from its top and inner sides is equal to the outgoing energy from its bottom and outer sides.

The 2D ring cross-section temperature distribution was verified with COMSOL, a commercial finite element package that is widely in multi-physics engineering applications. The result is shown in Figure 4-5.

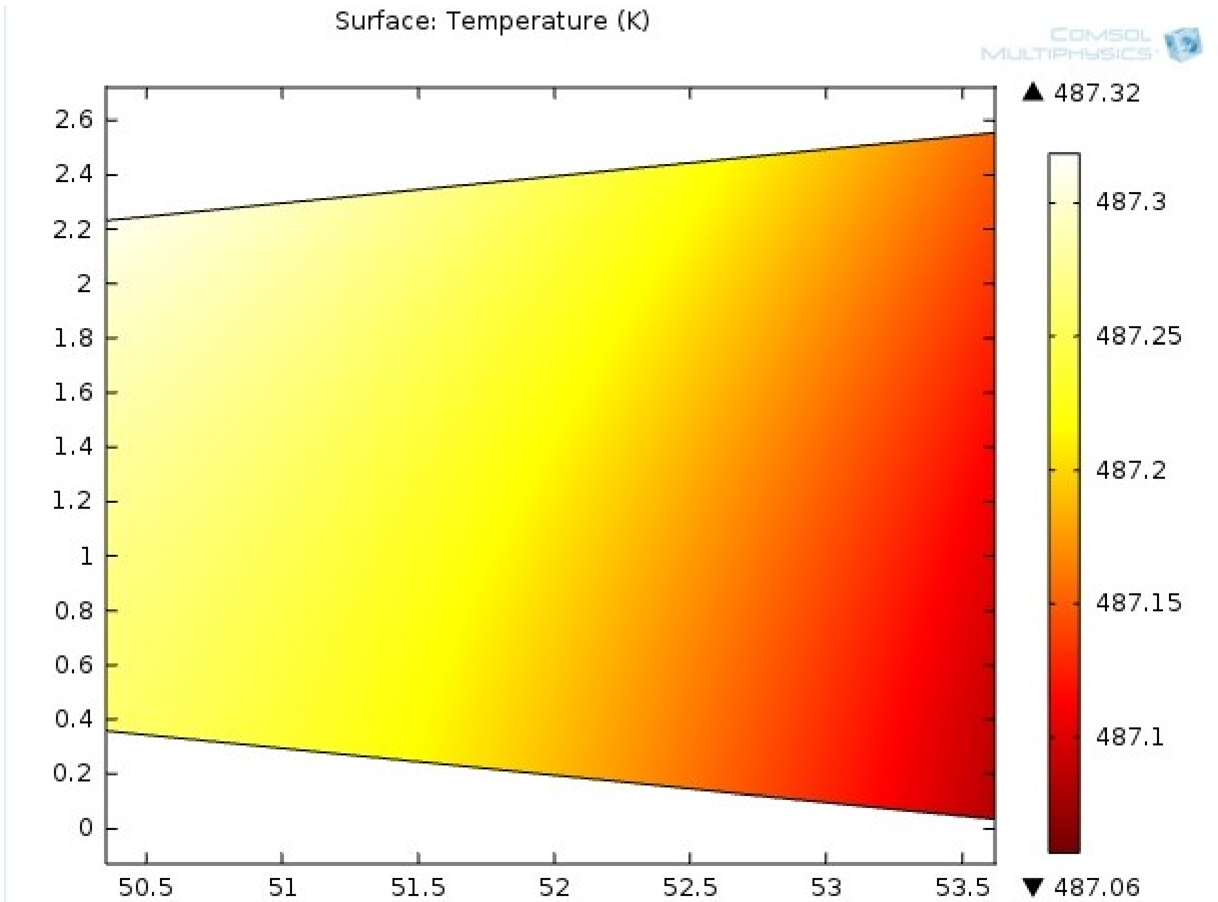

Figure 4-5 Ring cross-section temperature distribution from COMSOL

From Figure 4-5,the highest and lowest temperatures across the ring cross-section are 214.14°C (487.32 K) and 213.91 °C (487.06 K) respectively from the inner-upper corner through the outer-lower corner. The temperature gradient from the FEM code is verified being very small. The highest temperature from the FEM code showed good agreement with the COMSOL result. Although the lowest one showed a bit more deviation, the margin was still very small.

The difference between the FEM code and COMSOL result likely resulted from the way how the corner nodes who share two boundaries were treated. In the FEM code, the heat convection at those nodes are the summation of the two boundaries, which can result in higher temperature at the heat input side and lower temperature at heat output side.

From Figure 4-4 and Figure 4-5, the ring average temperature at the prescribed condition is about 214 °C, which is much higher than room temperature (25 °C). The inner upper corner has the highest temperature while the lowest temperature is found at the outer lower corner. However, the temperature gradient across the ring is very small, due to the small dimensions in both the radial and axial directions of the ring. These small dimensions do not provide high thermal resistance with the material being used. Although the temperature gradient across the ring is small, the temperature increase from the room temperature to the hot operation condition is significant. This large temperature change does act as a thermal load that can cause ring volumetric thermal expansion. Thus, the temperature influenced ring free shape must be studied when analyzing the ring-cylinder wall contact.

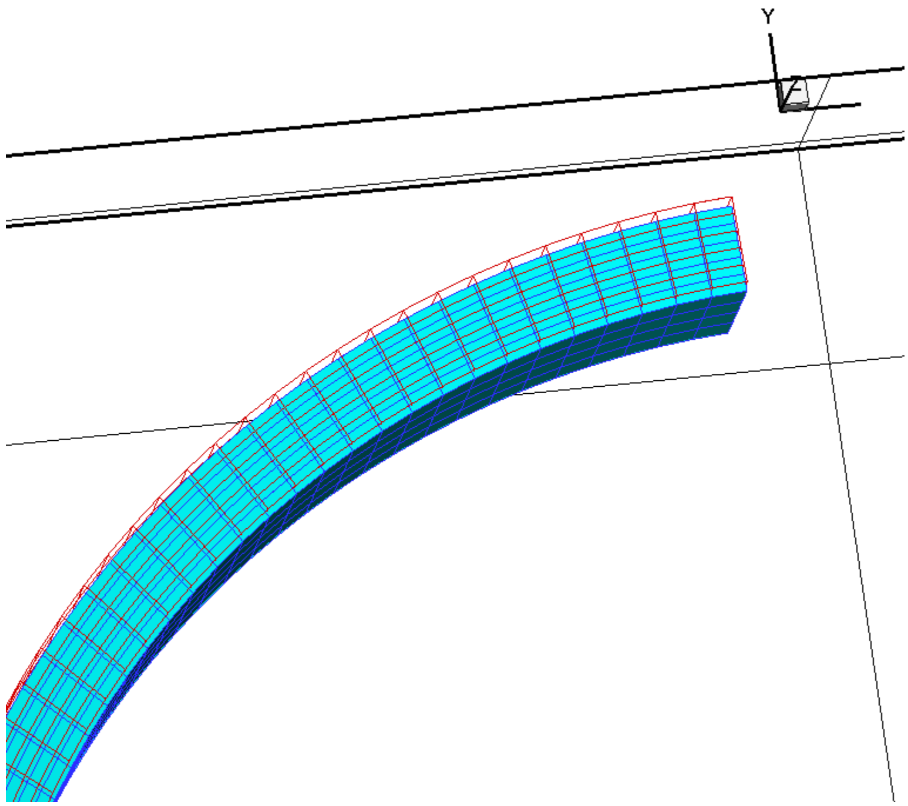

Figure 4-6 Ring free shape with and without temperature influence

Figure 4-6 shows the ring at room temperature condition (blue mesh with shade) as well as the ring after thermal expansion (red mesh). It clearly shows that the ring radius of curvature increases. The ring radius growth along the circumferential direction is not as significant as in the radial direction. However, the ring curvature length increases as well.

As for the room temperature condition (cold), the ring free shape normalized radius at high temperature operation condition (hot) is also plotted, for comparison. The plot can be found in Figure 4-7. The maximum radial growth for the ring is 0.33 mm. It is obvious the free shape has changed significantly considering the temperature effect.

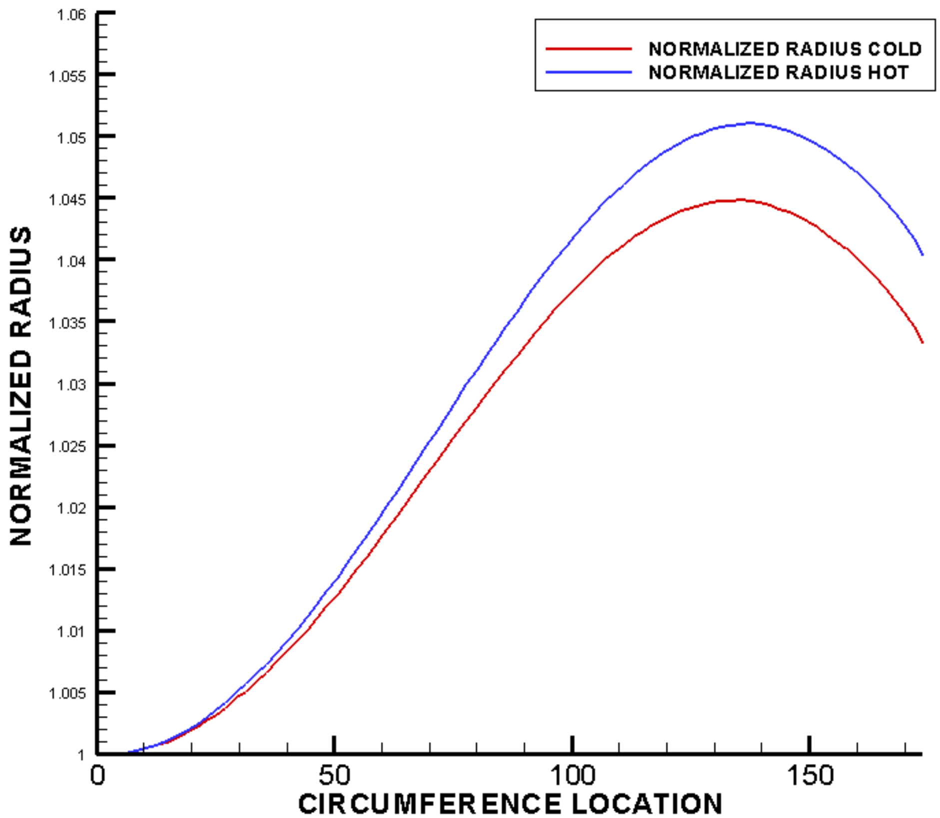

Figure 4-7 Normalized ring radius with and without temperature influence

With the influence of thermal load on the ring, the ring-cylinder bore conformability and the contact force/pressure can vary. Particularly, if the radius of curvature at the ring end tips increases greatly, the ring can lose its conformability near the ring end. Instead, point contacting occurs at the ring tips as shown in Figure 4-8.

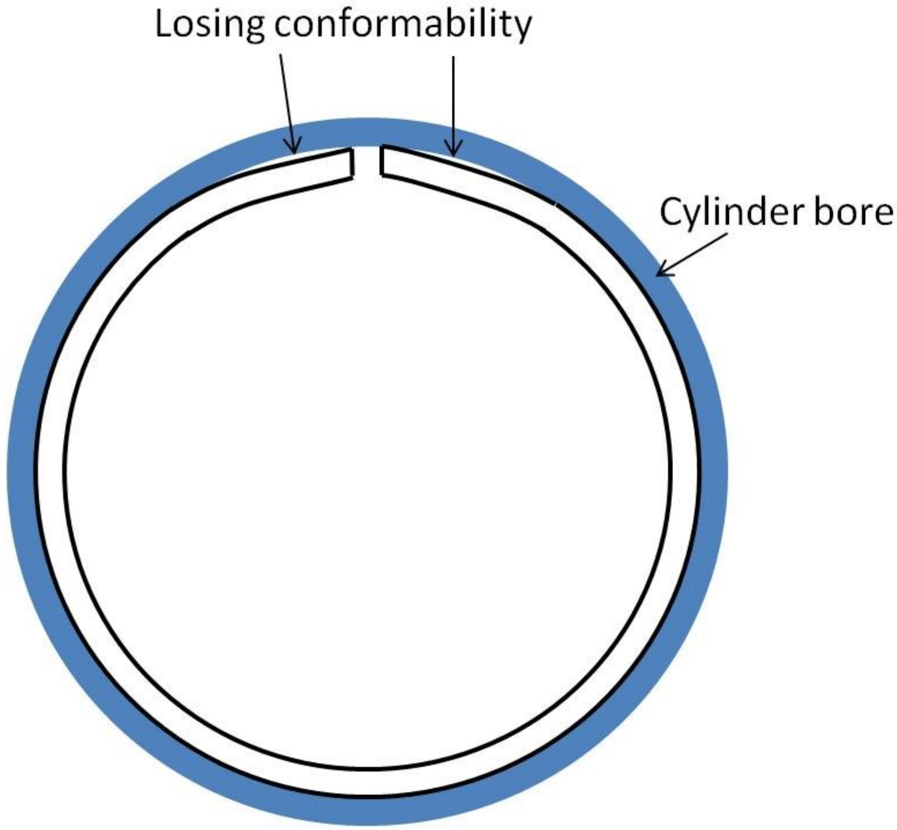

Figure 4-8 Losing conformability due to thermal influence

The loss of conformability results in separation gaps between the ring front face and the cylinder wall, allowing gas to escape from the high pressure side to low pressure side. This could be bad for engine blowby control. In addition, the loss of conformability also results in high contact pressure at the ring tips. This is one of the reasons of the high wear typically found at the ring end tips.

4.3.2 Result of Ring-Cylinder Bore and Ring-Groove Contact

The ring-cylinder liner contact was also analyzed for the temperature influenced free shape ring. The constraint forces and separation gap sizes at the upper and lower edges along the ring circumference with temperature influence can be found in Figure 4-9. The constraint force pattern along the ring circumference shows that separation gaps also exist at the ring tips. However, these gaps have been significantly reduced. And the constraint loads at the locations about ±30° and ±120° away from the ring back are very small compared to other locations. Slight difference in contact force can be found between the upper edge and the lower edge at the same circumferential location. This results from the temperature difference across the ring cross-section. The higher temperature at the ring inner upper corner and the lower temperature at the outer lower corner introduce a twist torque that tends to twist the ring negatively. The higher constraint force at the upper corner and lower force at the lower corner form another moment that balances the temperature induced twist moment. The separation gap at the ring tips also shows difference between the upper and lower edges with the upper gaps slightly smaller than the lower ones.

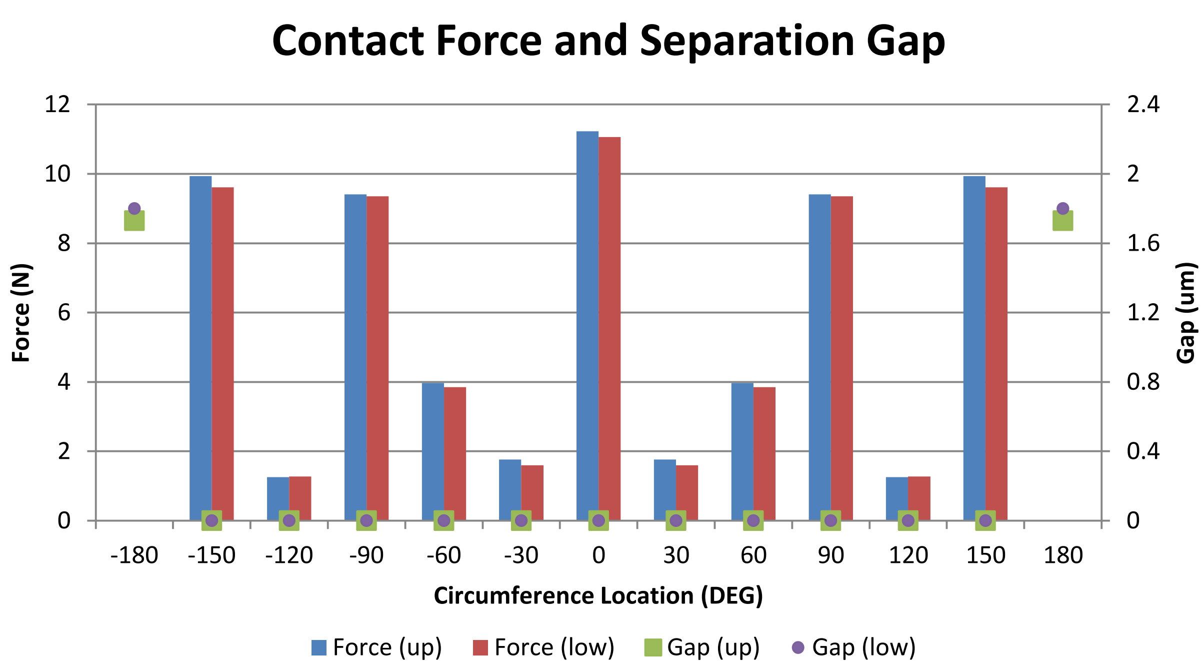

Figure 4-9 Contact force and separation gap with temperature influence

The constraint forces and separation gaps around the ring circumference with temperature influence are also listed in Table 4-3.

Table 4-3 Constraint forces and separation gap size with temperature influence

Location	0°	30°	60°	90°	120°	150°	~180°
Force, Up (N)	11.2	1.8	4.0	9.4	1.3	9.9	0.0
Force, Low (N)	11.1	1.6	3.9	9.4	1.3	9.6	0.0
Gap, Up (μm)	0	0	0	0	0	0	1.7
Gap, Low (μm)	0	0	0	0	0	0	1.8

It is also worthwhile to study how the constraint force pattern changes between the cold ring and temperature influenced hot ring. Figure 4-10 shows the constraint forces at the upper and lower edges along the ring circumference comparison between the conditions with and without temperature influence. At the cold condition, the constraint forces at the upper and lower edges are identical at the same circumferential location as explained in the previous section. Only one bar plot is needed to represent the constraint forces at either edge at cold condition. The constraint forces all increase with different magnitude except for the one at around 120° away from the ring back with the consideration of the temperature compensation. The location of the maximum constraint force shows agreement as at the ring back.

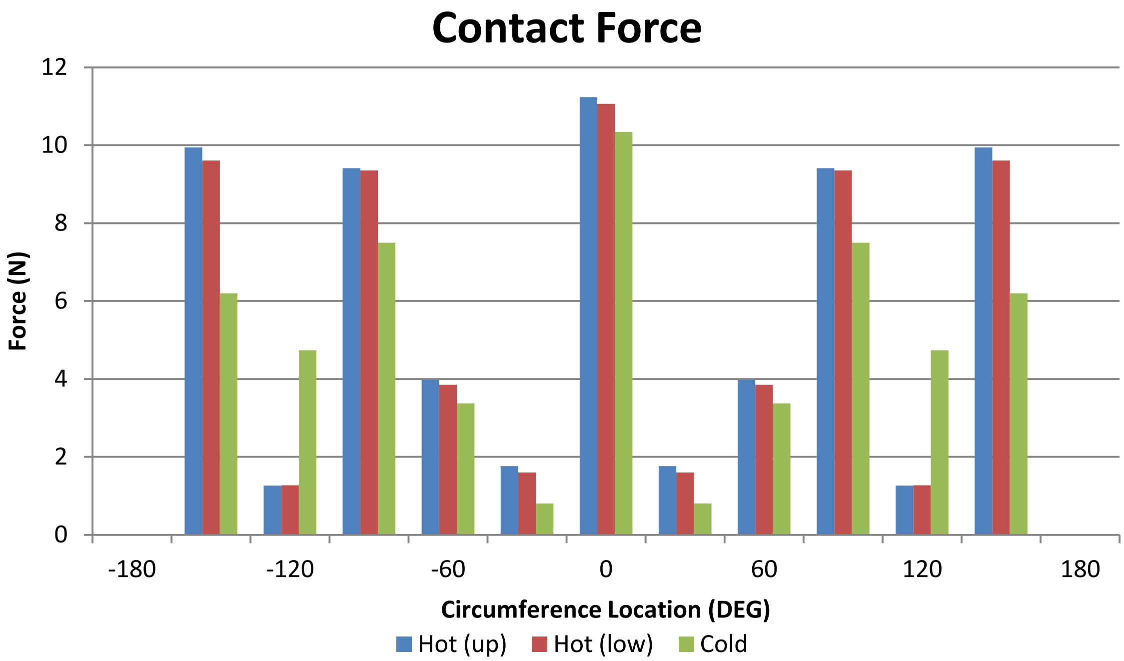

Figure 4-10 Contact force with and without temperature influence

4.3.3 Application on EcoMotors 2-Stroke Engine

With the temperature compensation considered, the ring-bridge contact was analyzed in a similar way as for the cold condition. Three boundary conditions were studied as well: the ring gap at the middle of bridge; ring gap in the middle of port and one tip at the bridge one tip in the port. In each of these conditions, two constraint patterns were used: one is the constraint force at the bridge middle and the other is the constraint forces at the bridge edges. And the contact pressure distributions were calculated in the same way as the previous cold condition. The pressure distribution for the ring gap at the middle of bridge boundary condition case (BC1) with temperature compensation is shown in Figure 4-11.

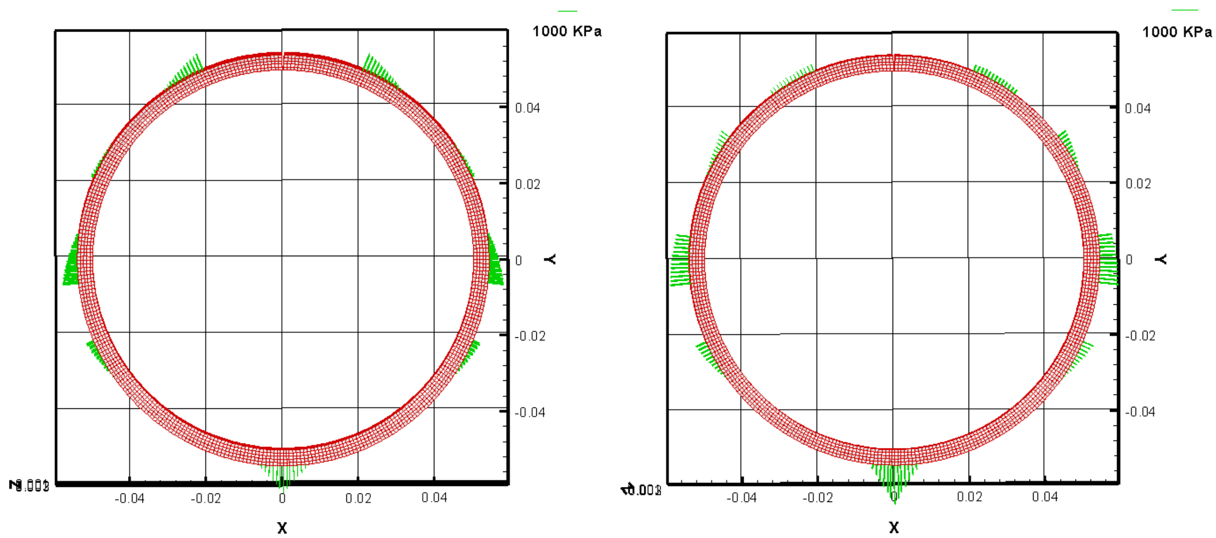

a. Constraint at middle of bridge

b. Constraints at bridge edges

Figure 4-11 Pressure distribution for ring gap at middle of bridge case with temperature influence

From Figure 4-11, the pressure distributions show agreement between the two constraint cases regarding to pressure magnitudes at different bridges. The pressure distribution patterns between these two cases also show good agreement except for at the bridges at 90° and 270°. The result of the constraint at the middle of bridge case shows bigger pressure difference across the bridge while the constraints at bridge edges case suggests a more homogeneous distribution. Comparing the result to Figure 3-20 that did not consider temperature compensation, it is found that the pressure distributions on the bridges locating at 30° and 330° as well as 60° and 300° behave different with temperature compensation. This is due to that face that the ring free shape is changed under the thermal load.

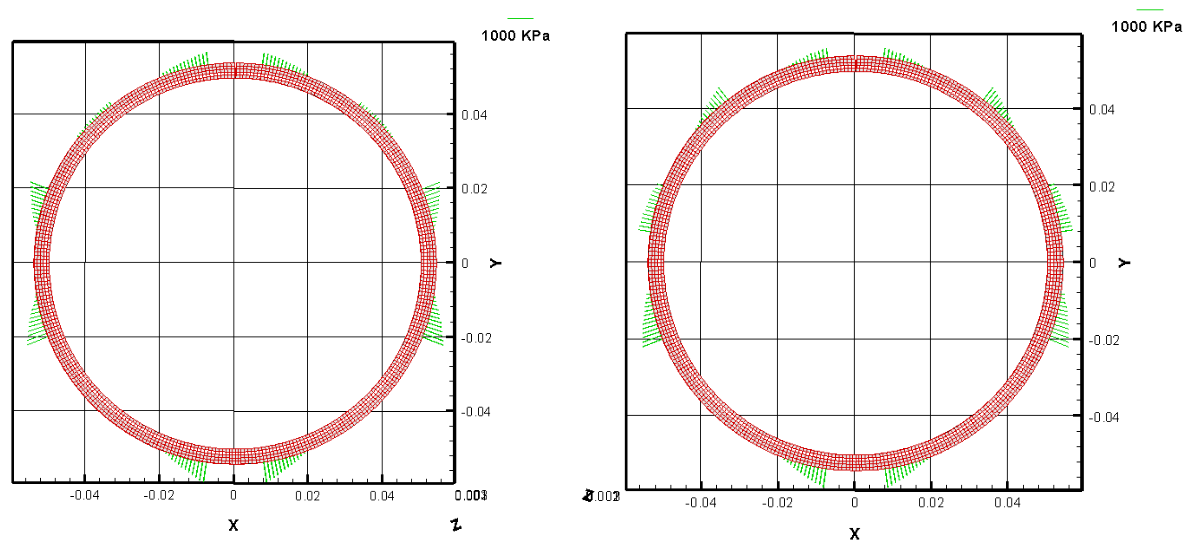

a. Constraint at middle of bridge

b. Constraints at bridge edges

Figure 4-12 Pressure distribution for ring gap at middle of port case with temperature influence

Similarly, the pressure distributions at bridges for the ring gap at middle of port case (BC2) with temperature compensation are shown in Figure 4-12. The two constraint cases showed good agreement except the pressure distribution at the bridge locating at 75° and 285°. In addition, the constraints at bridge edges case showed a little higher pressure at the bridges at 45° and 315°. Both results showed there is no pressure at the bridges locating at 135° and 225°. This means the pressure is expected to be low at those locations as ring free shape measurement error could be involved for the ring mesh.

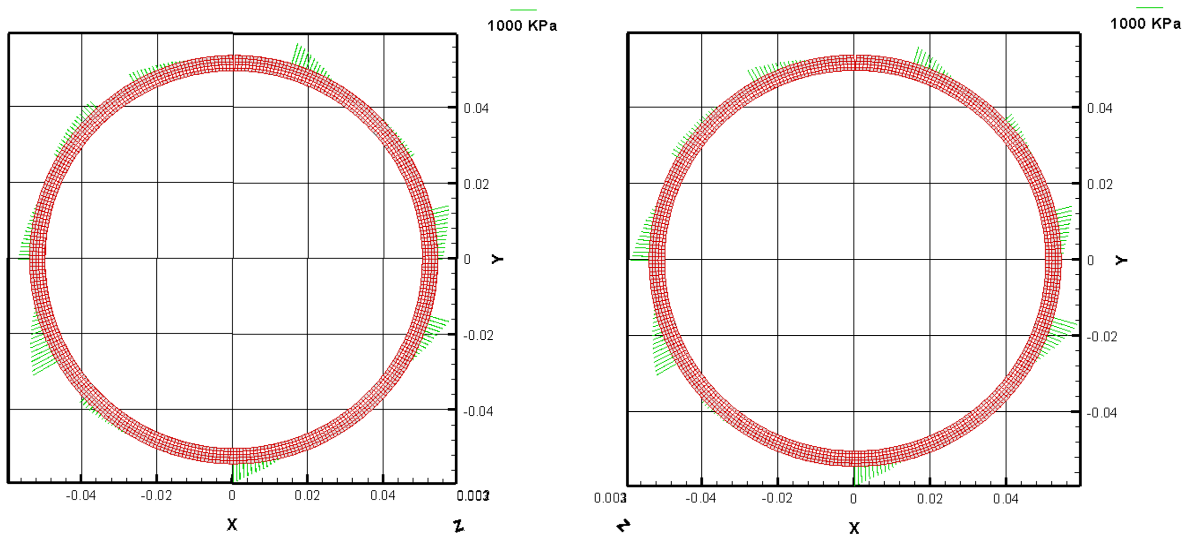

a. Constraint at middle of bridge

b. Constraints at bridge edges

Figure 4-13 Pressure distribution for one tip at bridge and one tip in port case with temperature influence

The bridge pressure distributions for the one tip at bridge and one tip in port case (BC3) are shown in Figure 4-13. The ring right tip is in the port and the left tip is at the bridge area. The two constraint cases showed great agreement regarding to the pressure magnitude as well as the distribution pattern at different bridges. Comparing to the pressure distribution at the cold condition, the results with temperature compensation showed the pressure pattern at the bridge locating at 23.4° changed. This can be explained as the ring grew outward due to the thermal load and thus the pressure is higher at the bridge edge that is closer to the ring tip.

Chapter 5 RING-CYLINDER LINER LUBRICATION AND WEAR

5.1 Introduction

Friction occurs between the contact surfaces when they have relative motions. The engine power cylinder system has a major contribution to engine mechanical friction [57-63]. Engine fuel economy also benefits from friction reduction [64, 65]. Stribeck diagram (Figure 5-1) is typically used to define the friction coefficient between the contact pairs [42]. In the diagram, the ordinate is the friction coefficient and the abscissa defines the operating condition, which is the product of the lubrication oil viscosity μ and the relative velocity N, divided by the normal load P on the surfaces.

The Stribeck curve can be divided into three zones: the boundary friction zone, mixed friction zone and the hydrodynamic friction zone. The boundary friction zone is where asperity contact occurs due to lack of lubrication supply. As a result, the friction coefficient is relatively high and remains almost constant throughout the boundary friction zone. The hydrodynamic friction zone is recognized as the hydrodynamic lubrication occurs. Thus, instead of asperity contact, the two surfaces are separated by a thin lubrication oil film, in the order of less than one micron. The hydrodynamic friction is caused by the share stress of the lubrication oil layer between the two surfaces. Hydrodynamic friction increases as the oil viscosity or velocity increases; but decreases as the normal load increases. Between the boundary friction zone and the hydrodynamic friction zone is the mixed friction zone, where both boundary friction and hydrodynamic friction can be found. Depending on the operating condition, the contact pressure is carried differently by the asperity contact and hydrodynamic contact.

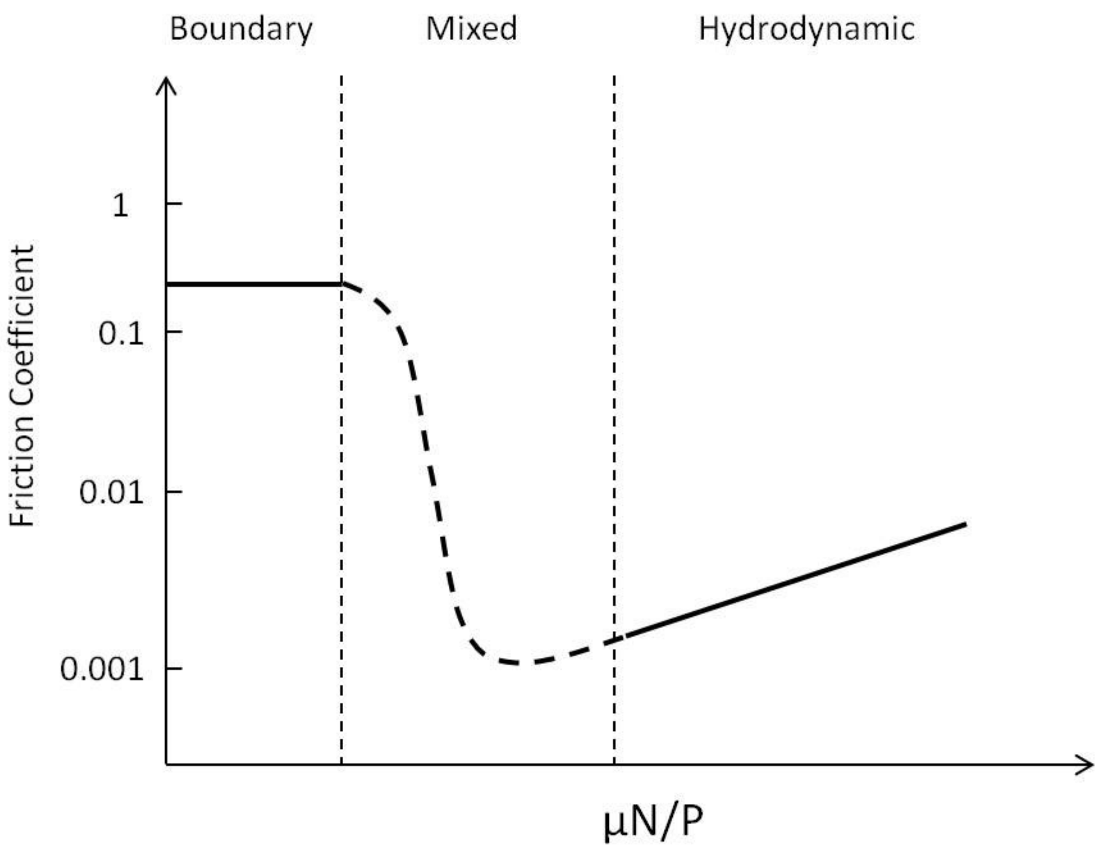

Figure 5-1 Stribeck diagram

Within the engine, the valvetrain system mainly experiences boundary friction, with a small amount of mixed friction; the engine bearings experience mainly the hydrodynamic friction; and the piston skirt mainly faces hydrodynamic friction. For the piston rings, both mixed friction and hydrodynamic friction can be found. The top compression ring with a barrel face has mostly hydrodynamic friction. However, lubrication oil may not be sufficient as the piston moves close to TDC. As a result, asperity friction occurs for the top ring. For a scraper second compression ring, hydrodynamic friction and asperity friction switches between the upward strokes and the downward strokes. The oil control ring has asperity friction most of the time since the rails of the oil control ring breaks the oil film thus hydrodynamic lubrication cannot form.

Boundary friction, also known as asperity friction, and the hydrodynamic friction are important phenomena within the power cylinder system. The power cylinder system friction loss, wear depend heavily on these phenomena. Thus, understanding the physics of these phenomena as well as their contribution in carrying the contact load becomes important.

5.2 Asperity Contact Model

The Greenwood-Tripp model for the contact of two nominally flat rough surfaces is a widely used model in asperity contact studies [66, 67]. The model describes the contact of two surfaces depends on the topography of the surfaces and showed indistinguishable results from the previous single rough surface models. They claimed that the asperity height of the rough surface is very close to a Gaussian distribution, for non-worn surfaces.

For two rough surfaces separated by gap h, the nominal gap is defined by:

$$\boldsymbol{H_\sigma = \frac{h}{\sigma}} \tag{5-1}$$

where σ is the composite standard deviation of the asperity heights distribution, which is defined as:

$$\boldsymbol{\sigma = \sqrt{\sigma_1^2 + \sigma_2^2}} \tag{5-2}$$

In the above equation, σ_1 and σ_2 are the standard deviation of the asperity height distribution of the two rough surfaces as shown in Figure 5-2.

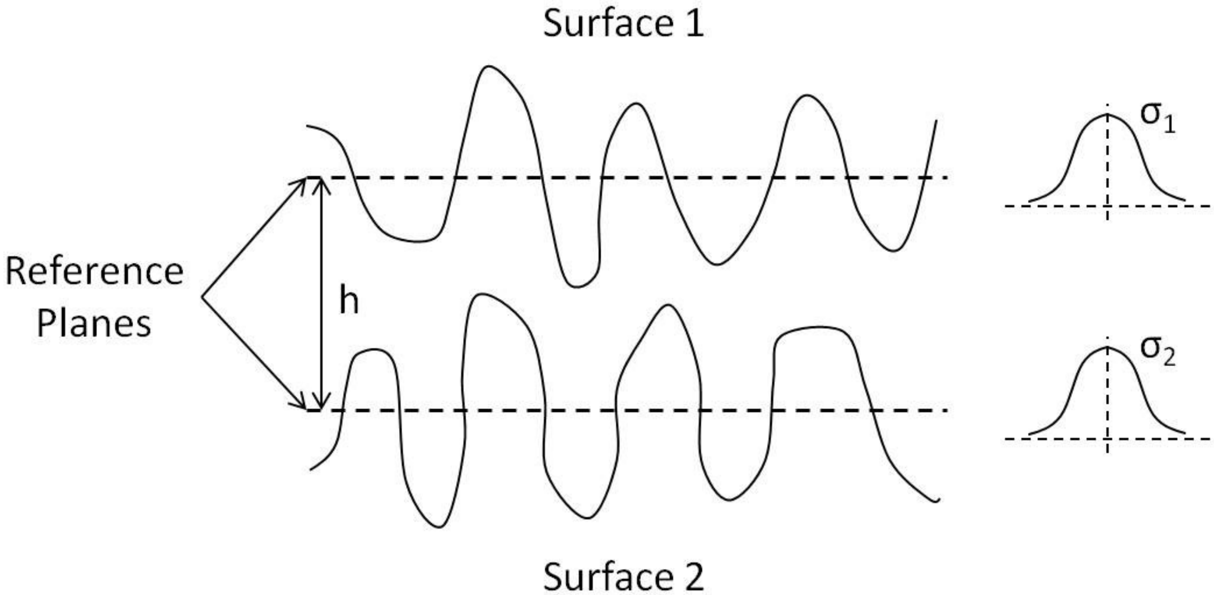

Figure 5-2 Asperity distribution for rough surfaces

The contact load carried by the asperity $P_{(h)}$ then can be expressed as:

$$\boldsymbol{P_{(h)} = KE'F_{5/2(H_\sigma)}} \tag{5-3}$$

where K, E' and $F_{5/2(H_\sigma)}$ are the functions of surface properties and the material property.

K is a function of the asperity density η and the radius of curvature β of the surfaces and K can be expressed as:

$$\boldsymbol{K = \frac{16\sqrt{2}}{5}\pi(\eta\beta\sigma)^2\sqrt{\frac{\sigma}{\beta}}} \tag{5-4}$$

E' is the composite modulus of elasticity of the two contacting materials, and is defined as:

$$\boldsymbol{\frac{1}{E'} = \frac{1-v_1^2}{E_1} + \frac{1-v_2^2}{E_2}} \tag{5-5}$$

$F_{5/2(H_\sigma)}$ is the function that describes the integral of the Gaussian distribution of the asperity heights. $F_{5/2(H_\sigma)}$ is defined as:

$$F_{5/2(H_\sigma)} = \frac{1}{\sqrt{2\pi}} \int_{H_\sigma}^{\infty} (u - H_\sigma)^{5/2} e^{-u^2/2} du \tag{5-6}$$

It is clear that there is no close form solution for the evaluation shown in equation 5-6. Either numerical solution or approximate solution are needed to evaluate this integration. Greenwood and Tripp gave tabulated values for the integration as shown in Table 5-1. These values are used to approximate the value of integration of $F_{5/2(H_\sigma)}$.

Table 5-1 Tabulated values for $F_{5/2}$

H_σ	$F_{5/2(H_\sigma)}$
0.0	0.61664
0.5	0.24040
1.0	0.08056
1.5	0.02286
2.0	0.00542
2.5	0.00106
3.0	0.00017
3.5	0.00002
4.0	0.00000
>4.0	0.00000

Some approximation models have been proposed to evaluate the integral $F_{5/2(H_\sigma)}$ easily. A power law approximation has been proposed by Hu et al [68]. The expression for the approximation is:

$$\boldsymbol{F}_{5/2(\boldsymbol{H}_\sigma)} = \begin{cases} \boldsymbol{A}(\mathbf{4.0} - \boldsymbol{H}_\sigma)^{\boldsymbol{z}} & \boldsymbol{H}_\sigma < 4.0 \\ \mathbf{0} & \boldsymbol{H}_\sigma \geq \mathbf{4.0} \end{cases} \tag{5-7}$$

The constants in the approximation are found to be: $A = 4.4.68 \times 10^{-5}$ and $z = 6.804$.

Besides Hu's approximation model, Arcoumanis et al [58] proposed a sixth order polynomial for the approximation of $F_{5/2(H_\sigma)}$, which is approximated as:

$$F_{5/2}(H_\sigma) = \begin{cases} C_6 H_\sigma^6 + C_5 H_\sigma^5 + C_4 H_\sigma^4 + C_3 H_\sigma^3 + C_2 H_\sigma^2 + C_1 H_\sigma^1 + C_0 & H_\sigma < 4.0 \\ 0 & H_\sigma \geq 4.0 \end{cases} \tag{5-8}$$

In this approximation, $C_0, C_1, \dots, C_6$ are constants which can be found in Table 5-2 below.

Table 5-2 Constants for $\boldsymbol{F}_{5/2}$ approximation

Constant	Value
C_0	0.6167
C_1	-1.0822
C_2	8.0203×10^{-1}
C_3	-3.1933×10^{-1}
C_4	7.1624×10^{-2}
C_5	-8.5375×10^{-3}
C_6	4.2074×10^{-4}

Figure 5-3 shows the relationship between the asperity contact pressure and the normalized gap between the two flat surfaces with the $F_{5/2(H_\sigma)}$ evaluated with Arcoumanis' model.

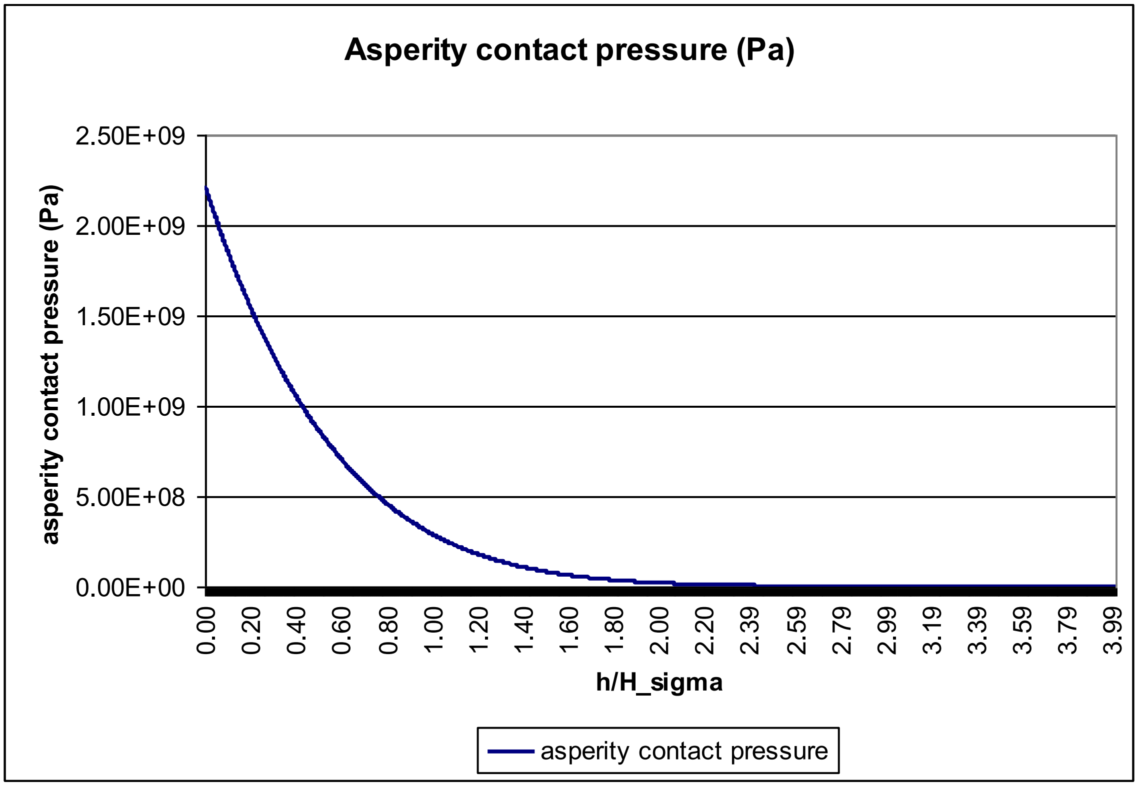

Figure 5-3 Asperity contact pressure

From Figure 5-3, a nonlinear relation is found between the asperity contact pressure and the normalized gap. And the asperity contact pressure decreases gradually as the gap increases between the two contacting surfaces. The asperity contact pressure vanishes eventually when the gap becomes greater or equal to 4 times of the normalized gap value.

5.3 Hydrodynamic Contact Model

Hydrodynamic contact carries the contact pressure together with the asperity contact. Reynolds' equation is a widely used method modeling hydrodynamic pressure distribution. And this model is also adopted to calculate the hydrodynamic lubrication pressure at the piston skirt/cylinder wall interface as well as the piston ring face/cylinder wall interface. The one-dimensional form of the Reynolds' equation can be expressed as:

$$\frac{\partial}{\partial x}\left(\frac{h^3}{\mu}\frac{\partial P}{\partial x}\right) = -6\frac{\partial x}{\partial t}\frac{\partial h}{\partial x} + 12\frac{\partial y}{\partial t} \tag{5-9}$$

Here, the time derivatives, $\frac{\partial x}{\partial t}$ and $\frac{\partial y}{\partial t}$ denote the relative velocities between the two moving surfaces along different direction. Thus, they can be considered constants and be replaced with U and V. Then the one-dimensional Reynolds' equation becomes:

$$\frac{\partial}{\partial x}\left(\frac{h^3}{\mu}\frac{\partial P}{\partial x}\right) = -6U\frac{\partial h}{\partial x} + 12V \tag{5-10}$$

A schematic diagram of this lubrication model is shown in Figure 5-4.

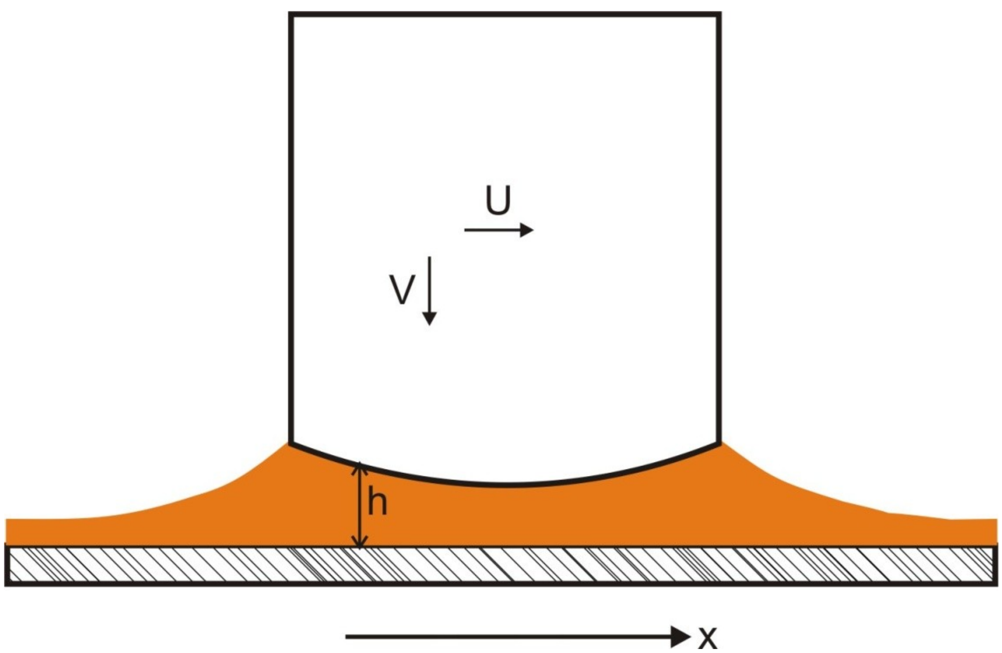

Figure 5-4 Schematic diagram of lubrication between surfaces

Known the pressure distribution, the shear stress resulted from the hydrodynamic friction can be obtained. The shear stress is defined as a function consisting a viscosity and dynamic part, and a pressure gradient part:

$$\bar{\boldsymbol{\tau}} = \frac{\boldsymbol{\mu U}}{\boldsymbol{h}} + \frac{\boldsymbol{h}}{\mathbf{2}}\frac{\partial \bar{\boldsymbol{P}}}{\partial \boldsymbol{x}} \tag{5-11}$$

However, this shear stress model predicts that the viscosity term becomes unbounded as the distance between the two surfaces approaches to zero. However, in practical, the breaking up of the oil film by the asperities as the distance approaches to zero should cause the viscous shear stress to approach to zero as well. Thus, this shear model is modified with flow factor method proposed by Patir and Cheng [69]. The shear stress equation is then defined as:

$$\bar{\boldsymbol{\tau}} = \frac{\boldsymbol{\mu U}}{\boldsymbol{h}}(\boldsymbol{\Phi_a} + \boldsymbol{\Phi_b}) + \boldsymbol{\Phi_c}\frac{\boldsymbol{h}}{\mathbf{2}}\frac{\partial \bar{\boldsymbol{P}}}{\partial \boldsymbol{x}} \tag{5-12}$$

where Φ_a, Φ_b and Φ_c are the flow factors.

In order to fulfill the condition that the shear stress stays bounded as the oil film thickness goes to zero, it is essential that the flow factors approach to zero as fast as the decrement of oil film thickness h. The flow factors are defined by Patir and Cheng as:

$$\boldsymbol{\phi_a} = \boldsymbol{f}(\boldsymbol{z}) = \frac{\mathbf{35}}{\mathbf{32}}\boldsymbol{z}\left[(\mathbf{1} - \boldsymbol{z}^{\mathbf{2}})^{\mathbf{3}}\ln\left(\frac{\boldsymbol{z}+\mathbf{1}}{\boldsymbol{\epsilon}/\mathbf{3}\boldsymbol{\sigma}}\right) + \ldots\right], \text{ where } \boldsymbol{z} = \frac{\boldsymbol{h}}{\mathbf{3}\boldsymbol{\sigma}} \tag{5-13}$$

$$\boldsymbol{\phi_b} = \mathbf{11.1}\left(\frac{\boldsymbol{h}}{\boldsymbol{\sigma}}\right)^{\mathbf{2.31}} \boldsymbol{e}^{-\mathbf{2.38}\frac{\boldsymbol{h}}{\boldsymbol{\sigma}}+\mathbf{0.11}\left(\frac{\boldsymbol{h}}{\boldsymbol{\sigma}}\right)^{\mathbf{2}}} \cong \mathbf{0} \tag{5-14}$$

$$\boldsymbol{\phi_c} = \mathbf{1} - \mathbf{1.4}\boldsymbol{e}^{-\mathbf{0.66}\boldsymbol{h}/\boldsymbol{\sigma}} \tag{5-15}$$

The viscous term of the shear stress equations can be written as:

$$\bar{\boldsymbol{\tau}}_{\mu} = \begin{Bmatrix} \boldsymbol{\mu U}\left(\frac{\phi_a}{\boldsymbol{h}}\right), & \boldsymbol{h} < 3\boldsymbol{\sigma} \\ \boldsymbol{\mu U}\left(\frac{\mathbf{1}}{\boldsymbol{h}}\right), & \boldsymbol{h} \geq \mathbf{3}\boldsymbol{\sigma} \end{Bmatrix} \tag{5-16}$$

Figure 5-5 shows both ${}^{1}/_{h}$ and ${}^{\Phi_a}/_{h}$, together with the viscous term with the flow factor taken into account for $\sigma = 0.4\ \mu m$ case. It is clear that without the flow factor, ${}^{1}/_{h}$ goes to infinity as h approaches to zero. However, ${}^{\Phi_a}/_{h}$ does converge to a certain value when h goes to zero. In this case, the viscous term of the shear stress is also bounded.

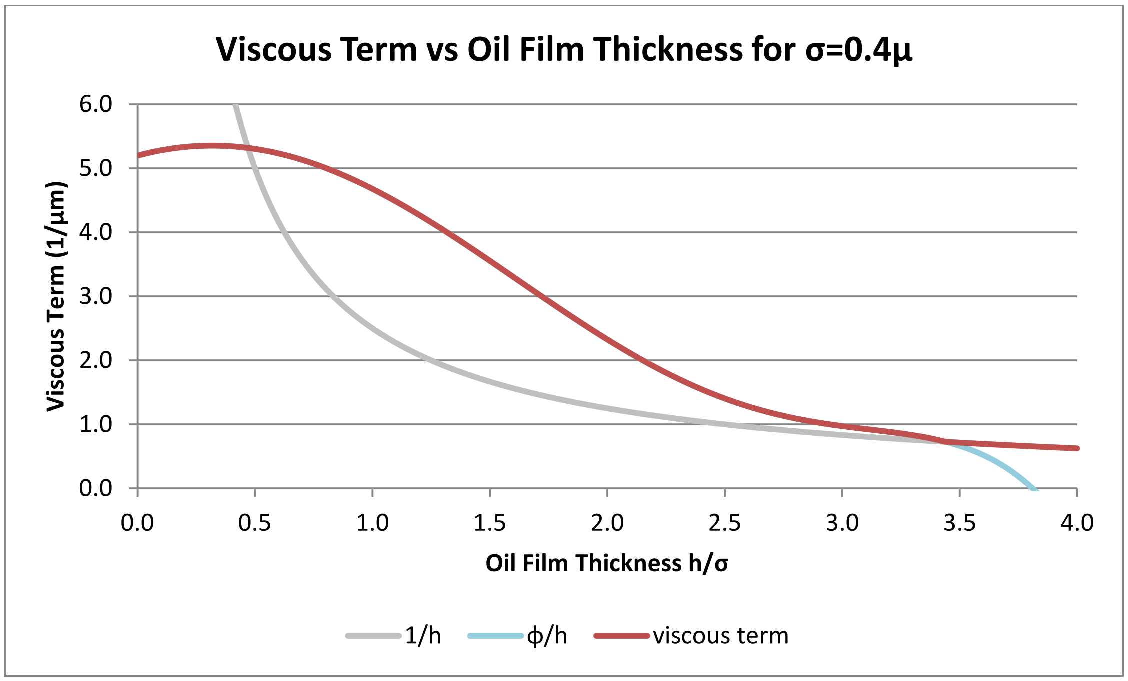

Figure 5-5 Viscous part of shear stress for different oil film thickness

Figure 5-6 illustrates to what value the viscous term of the shear stress converges to as the distance approaches to zero for different surface roughness cases. It becomes clear that the viscous term decreases as the surface roughness increases when the distance between the two surfaces is zero.

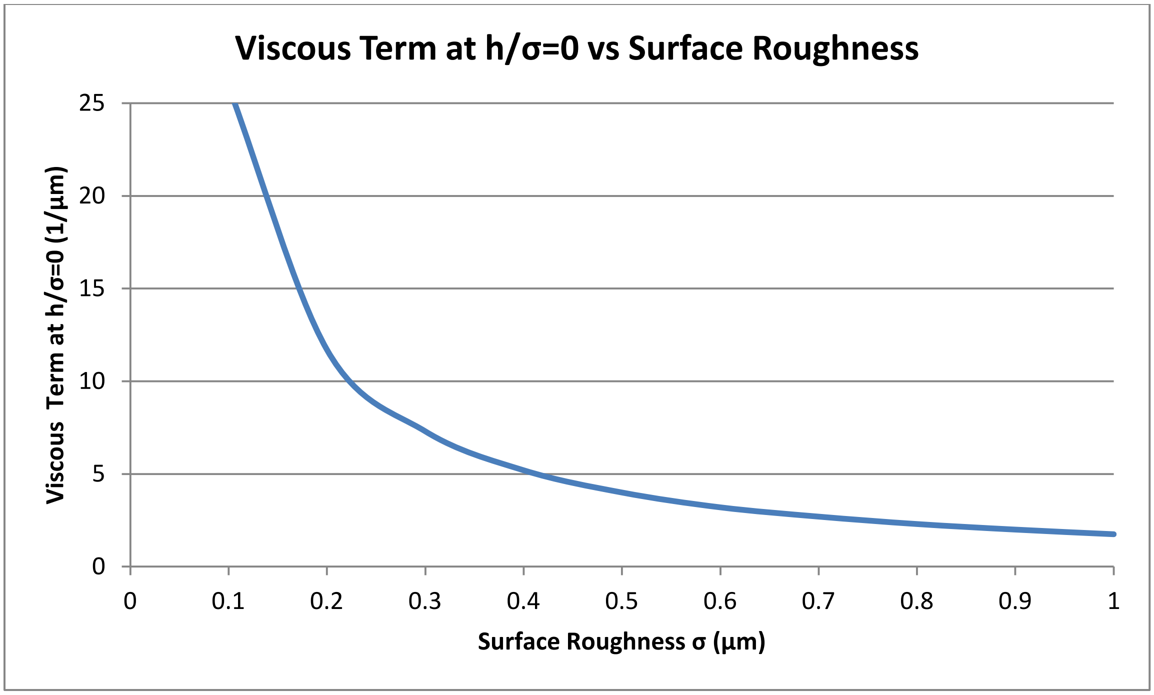

Figure 5-6 Viscous part of shear stress at different surface roughness

5.4 Wear

Wear occurs at the interacting surfaces when two contacting surfaces have relative motion. Wear can be categorized into different types: adhesive wear, abrasive wear, surface fatigue, corrosive wear, etc.

Adhesive wear occurs between surfaces with friction/asperity contact as the surfaces are sliding against each other.

Abrasive wear occurs between two surfaces when one of the surface is hard rough and the other one is softer.

Surface fatigue occurs when cyclic loading is involved for a surface. As a result, the surface material is weakened by the loading and materials are removed by the cyclic crack.

Corrosive wear refers to the process that chemical reaction occurs between the surfaces such that surface material degradation occurs.

A huge amount of effort has been committed for engine wear modeling and analysis [28, 70-76]. Considering the nature of wear and in order not to make the problem too complex, only adhesive wear mechanism is considered for the power cylinder system. And Archard equation [77] is adopted to model the wear. According to Archard, the surface volume removed between the sliding surfaces is proportional to the sliding distance, the asperity contact load between the two surfaces and inversely proportional to the hardness of the surface material.

$$\boldsymbol{V = k\frac{NL}{H}} \tag{5-17}$$

where V is the removed volume; k is the wear coefficient determined empirically; N is the asperity contact force; L is the sliding distance between the two surfaces and H is the combined hardness of the two surface materials.

The local removed material volume can be obtained in the same manner:

$$\boldsymbol{dV = k\frac{(P_A dA)dl}{H}} \tag{5-18}$$

where P_A denotes the local asperity contact pressure and dA is the area of the local volume in contact, dl is the local sliding distance.

Sometimes it is more important to know the height of removed material, this can be found as:

$$\boldsymbol{dh = k\frac{P_a dl}{H}} \tag{5-19}$$

Integrated over the entire engine cycle, the overall wear for one engine cycle can then be obtained for one specific point.

A piston ring and groove side wear analysis for diesel engines has been conducted by Poort, M. and Cheng, C., Richardson, Dan, et al [78].

5.5 Simulation Result

The asperity and hydraulic contact models are applied on a top compression ring for a heavy duty diesel engine at full load operation condition. The approach can be summarized as: The ring tension is an input to the model. And the ring pressure distribution profile (cam shape) obtained from the 3D ring contact at static condition is also input. Besides, the gas pressure behind the ring is superimposed on the ring during cycle analysis. The lubrication oil used for this simulation is 10W40. And the in-cylinder gas pressure is plotted in **Figure 5-7**.

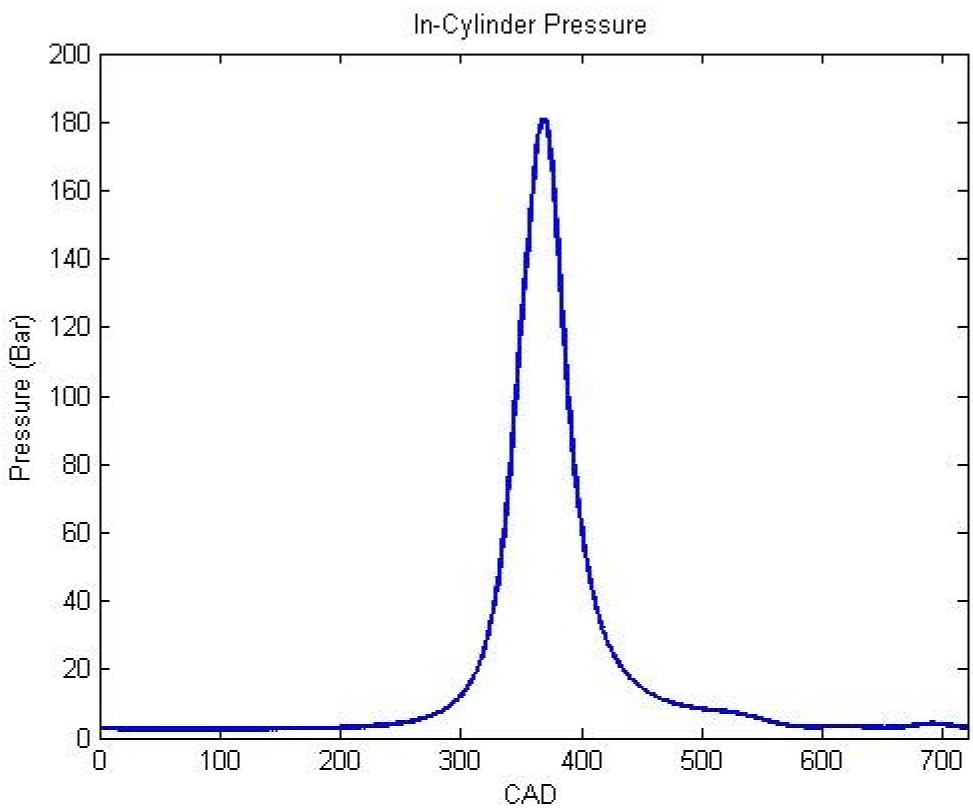

Figure 5-7 In-cylinder gas pressure

Under this condition, the oil film thickness for the top compression ring is shown in **Figure 5-8**.

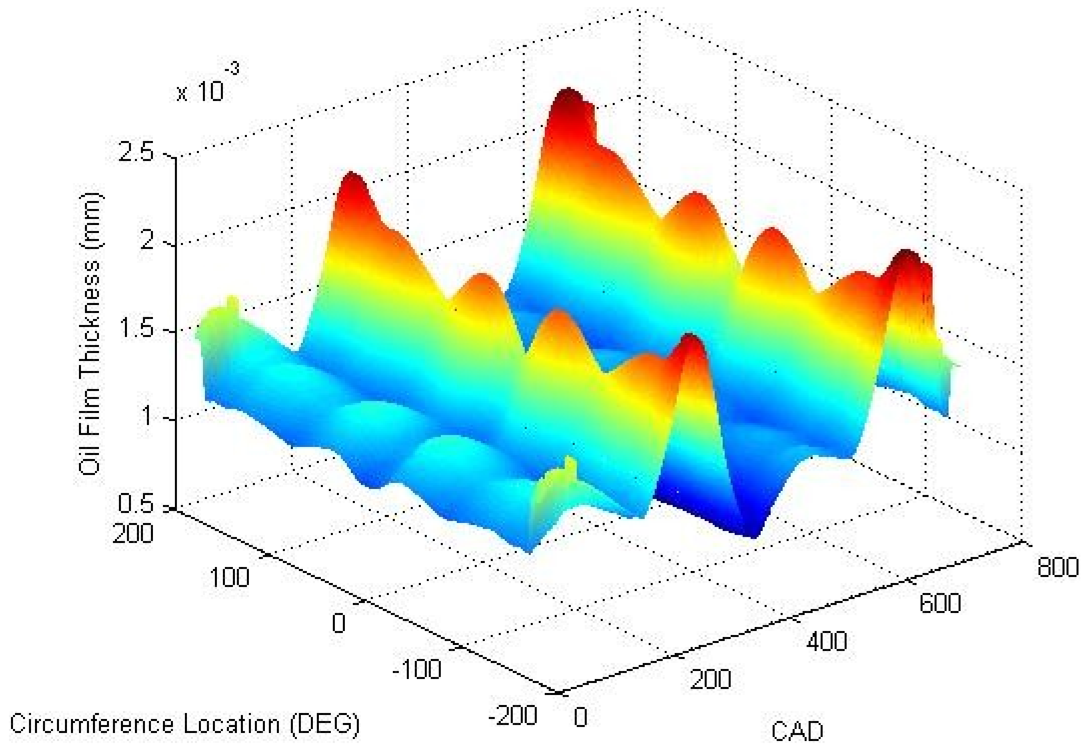

Figure 5-8 Oil film thickness for top ring

The oil pressure force for the top ring is shown in **Figure 5-9**.

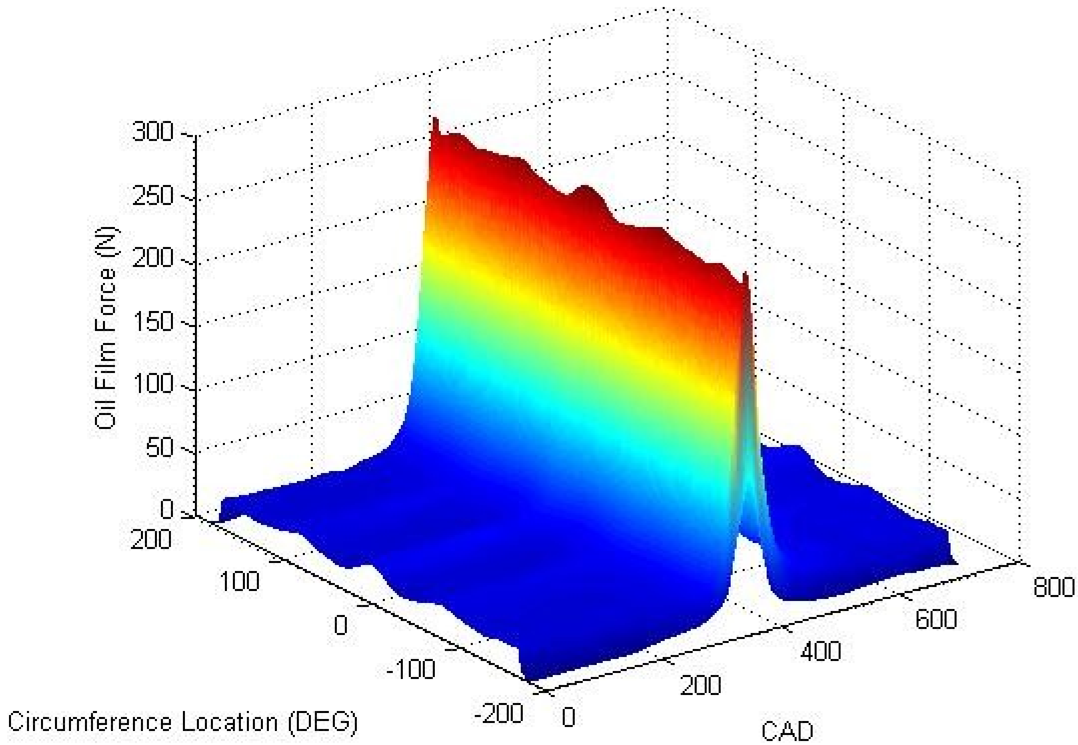

Figure 5-9 Oil pressure force for top ring

Figure 5-10 and Figure 5-11 show the asperity and hydrodynamic contact pressure for the top ring over the cycle.

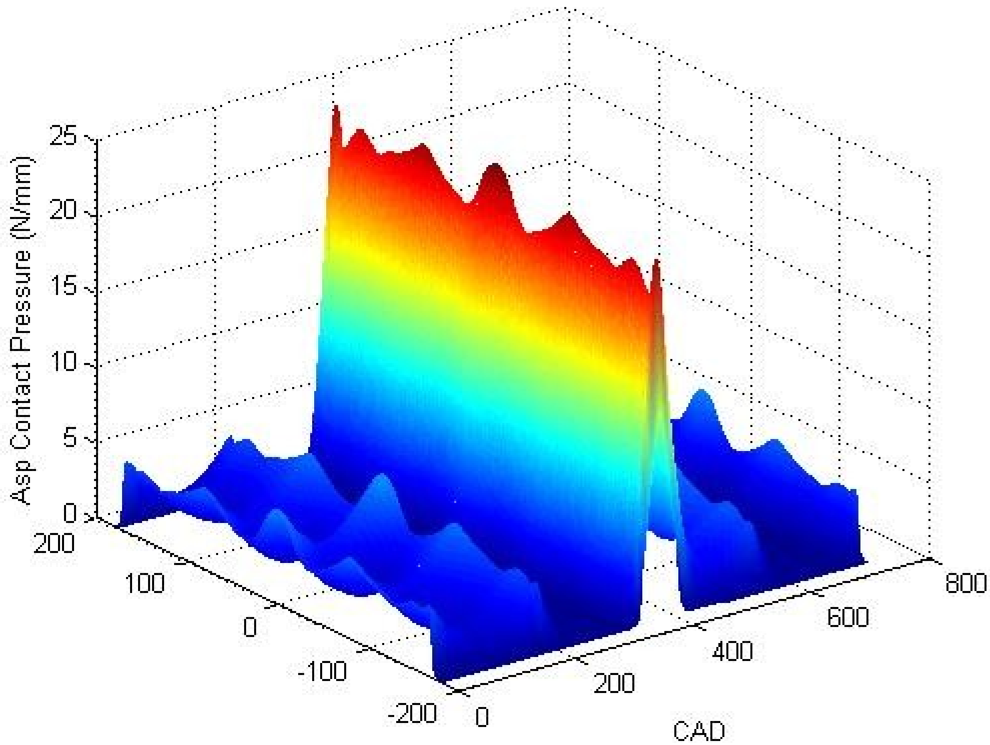

Figure 5-10 Asperity contact pressure for top ring

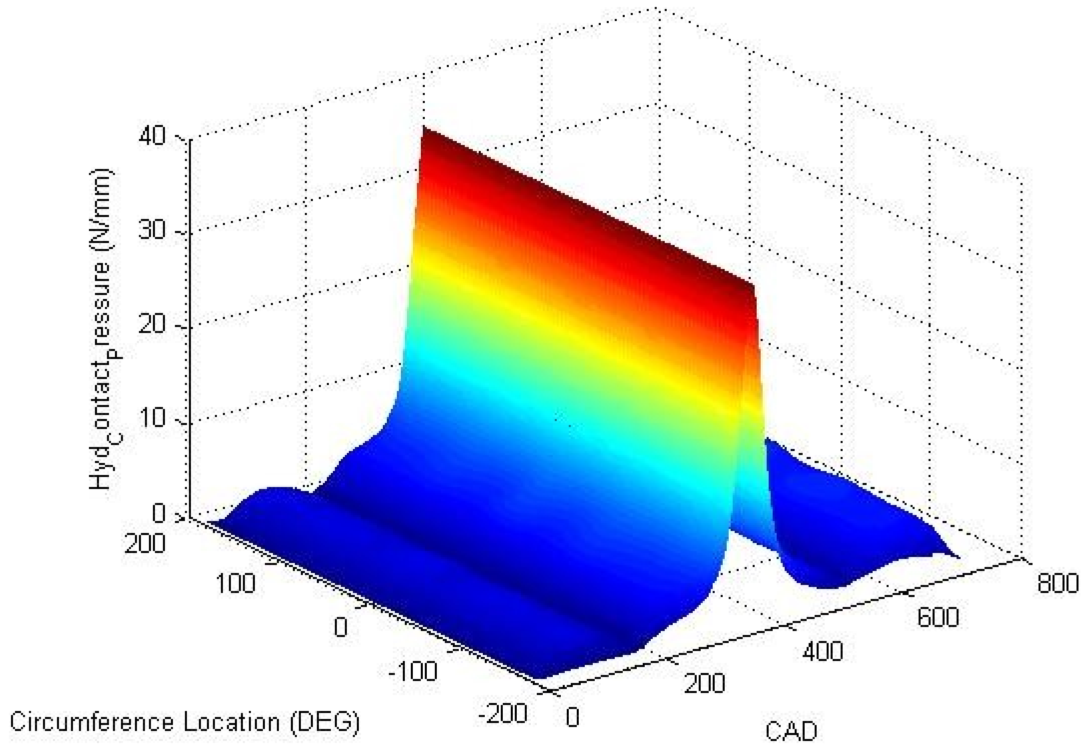

Figure 5-11 Hydrodynamic contact pressure for top ring

Figure 5-12 and Figure 5-13 show the asperity friction pressure and hydrodynamic friction pressure respectively.

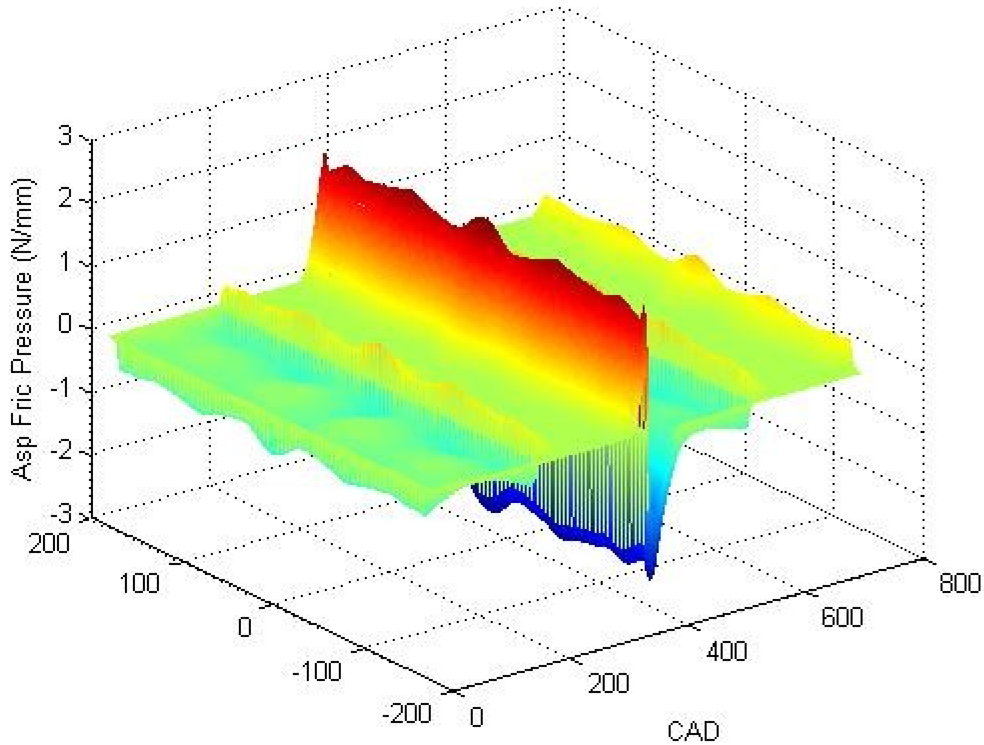

Figure 5-12 Asperity Friction Pressure

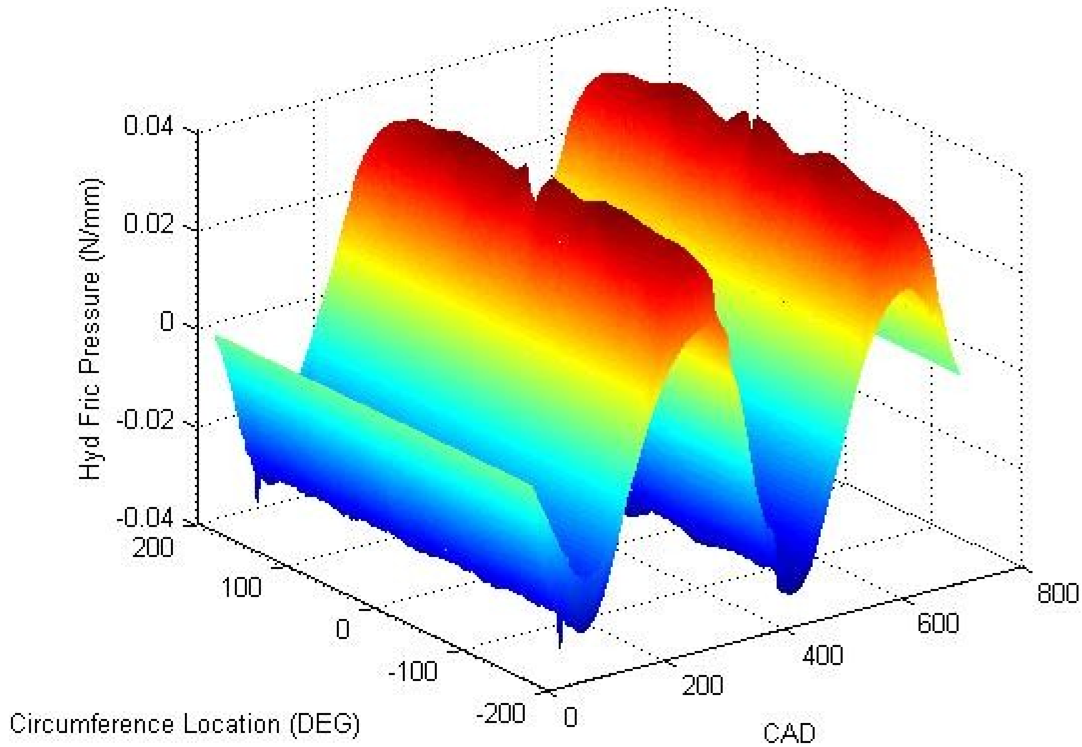

Figure 5-13 Hydrodynamic Friction Pressure

The instantaneous ring face wear for the top ring is shown in Figure 5-14.

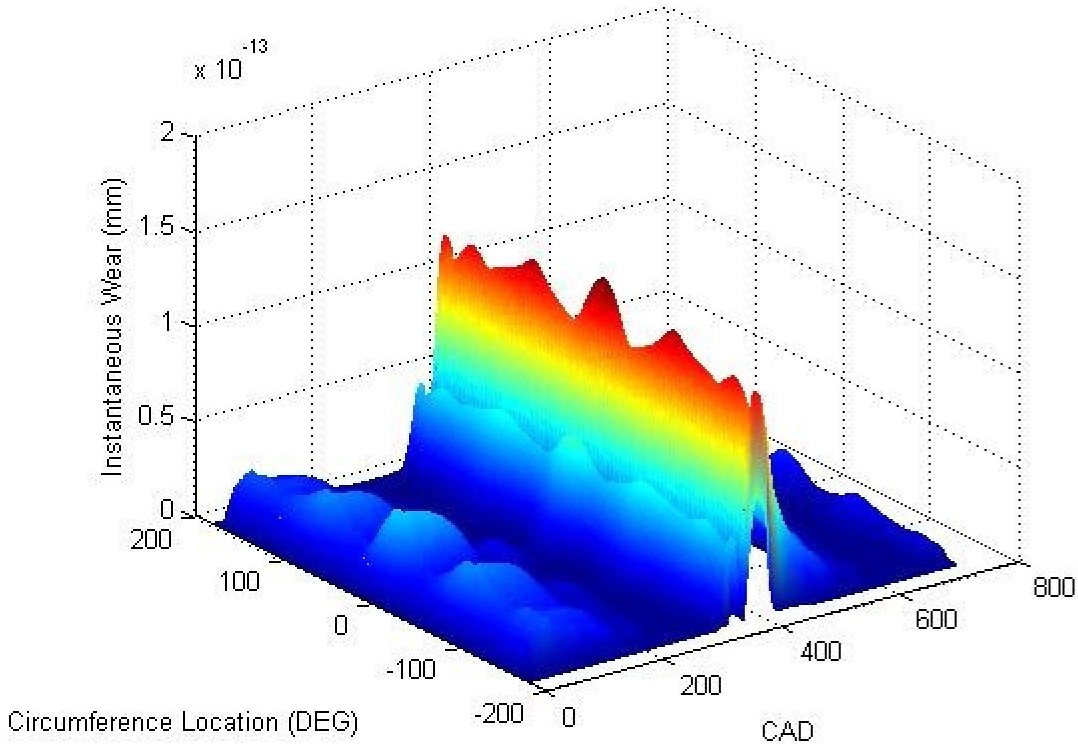

Figure 5-14 Instantaneous ring face wear for top ring

Chapter 6 VALIDATION OF NUMERICAL MODEL

6.1 Introduction

The 3D piston ring/cylinder bore contact FEA model presented in the previous chapters is compared with experimental measurement results.

Two experiment validations are used to verify the numerical model. One is by comparing the piston ring/cylinder bore contact force distribution along the ring circumference. The other is by comparing the separation gaps along the ring circumference as found by the numerical method.

6.2 Piston Ring Pressure/Force Distribution Measurement

A test rig capable of measuring the piston ring/cylinder bore contact load at variable circumferential locations is adopted to measure the contact force between the ring front face and the cylinder wall. The test rig setup is shown in Figure 6-1. In this test, the contact forces are only measured at five circumferential locations. Five locations may not be enough to represent the continuous contact force distribution. However, the goal is to validate the numerical model by comparing the numerical and measured results.

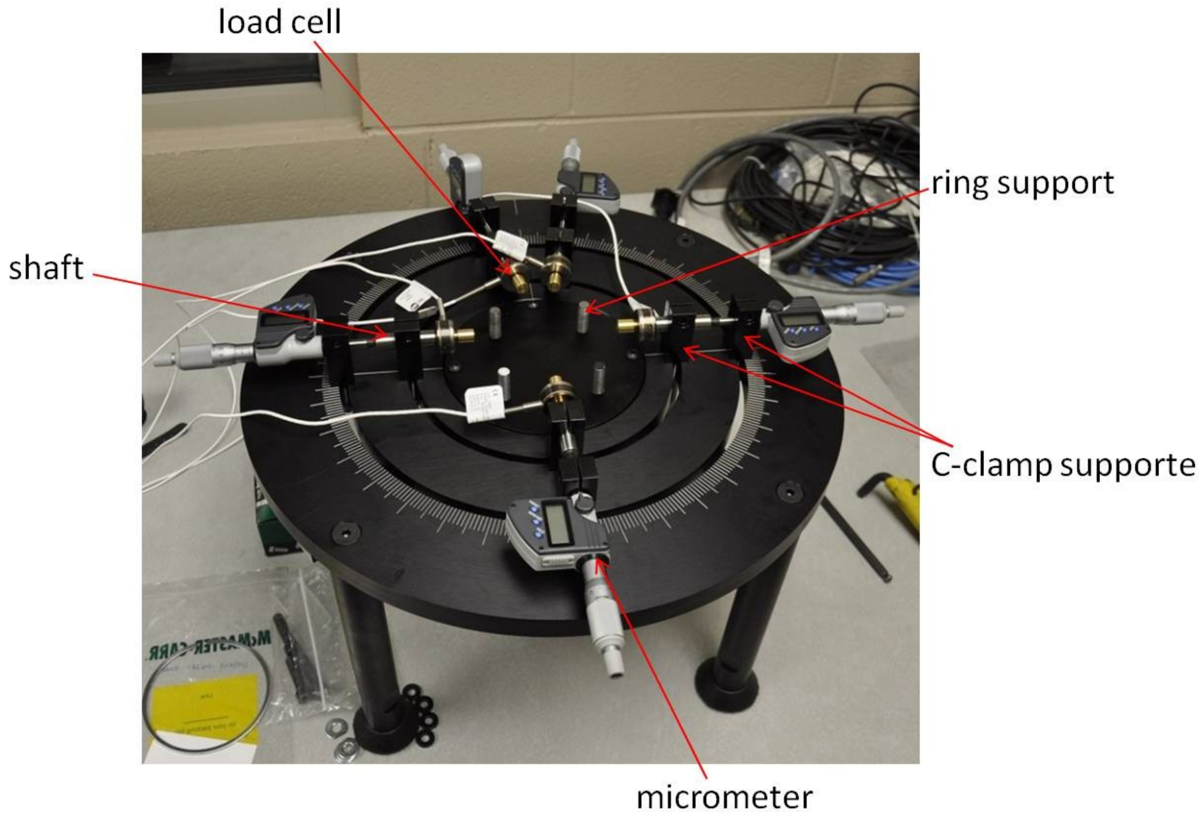

Figure 6-1 Ring pressure/force measurement rig

Miniature force transducers are used for measuring the force at the contact interfaces. The load cells are mounted onto metallic shafts, which are supported by their own C-clamp supporters. The C-clamps are not tightened such that the metallic shafts can slide with minimal friction between the shaft and the C-clamp interface. The radial movements of the load cells and the metallic shafts are constrained by the micrometers distributed circumferentially. These micrometers are also supported by the C-clamps. However, these C-clamps are tightened and the micrometers are not allowed to move in the radial direction. The ring supports are used to support the piston ring by holding the bottom of the ring. Two circumferential slots can be found which allow the load cells and the micrometers sliding along. Thus, the load cells can be located at different circumferential locations to measure the ring/cylinder bore contact forces at the desired locations. The output signals are recorded in the computer through a data acquisition system.

The load cells can be located at different radial location by adjusting the micrometers at the back of the load cells. This enables the test rig to account for variant cylinder bore diameters for different engine sizes. This is achieved by adjusting the load cells to align with a reference piston with known outer diameter (Figure 6-2). This load cell position is used as the reference position. Then, by further fine tuning of the micrometers, the desired cylinder bore inside diameter can be achieved.

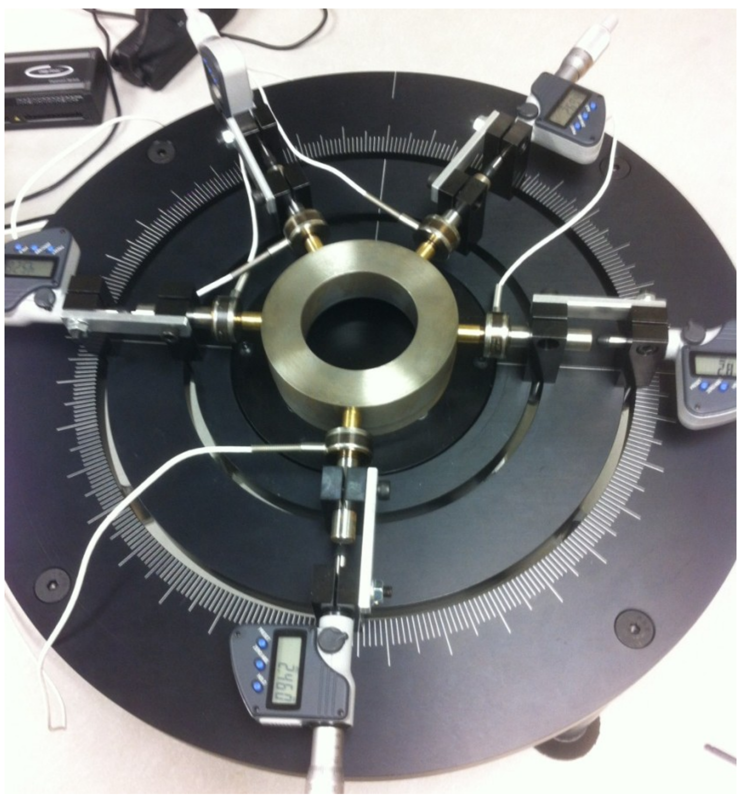

Figure 6-2 Ring test rig alignment

A sensitivity study was carried out for the ring contact force test rig to evaluate the performance of the rig. The ring/cylinder bore contact forces are measured five times. During each measurement, the contact forces are recorded twenty times with a frequency of 1 Hz. Since this is a static test, the measuring frequency is high enough to capture all variations occurring during the test. These twenty measurements are averaged after each test run. And the five averaged contact forces are used for sensitivity study. The averaged contact forces at different circumferential locations are shown in Figure 6-3.

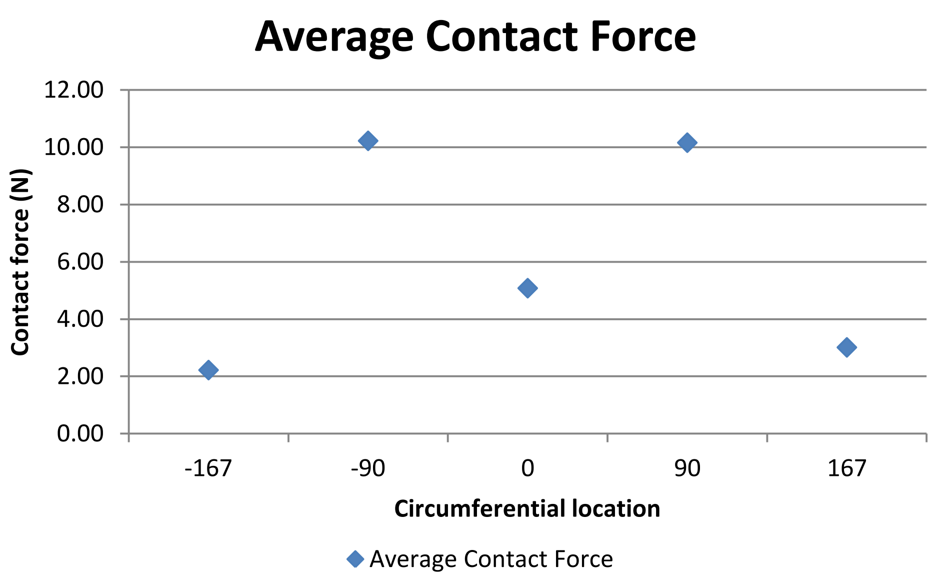

Figure 6-3 Measured contact force at different circumferential locations

From Figure 6-3, it clearly shows that the contact forces are the highest at 90° away from the ring back and lowest near the ring end gap (±167° away from the ring back). And the ring back contact force is in between. The analysis method mentioned above refers to the first level “Gage R&R” study used in some OEM’s. The “R&R” means repeatability and reproducibility. The second level “Gage R&R” requires dissembling and reassembling the experiment test rig each time taking the measurement data.

The contact forces at different load cell locations are then analyzed by calculating the normalized standard deviations as shown in Table 6-1.

Table 6-1 Normalized standard deviation of ring measurement rig

	-167°	-90°	0°	90°	167°
Std Deviation	0.48%	3.51%	7.09%	3.48%	1.44%

From the standard deviation values shown in Table 6-1, the experiment results show good consistency. This means the ring/cylinder bore contact force test rig is robust. The load cell location that shows the highest deviation is the one at 0° (at the ring back location). This is likely due to the fact that the two load cells that locate 90° away from the ring back introduce friction forces, which are almost in the direction of the normal force at the ring back. Thus, in each measurement the friction force behaves differently. As a result, the contact force at 0° shows higher variation, and also the highest standard deviation. This may be eliminated by installing bearings at the load cell contact surface.

A comparison between the measured contact forces and the model predicted contact forces are shown in Figure 6-4.

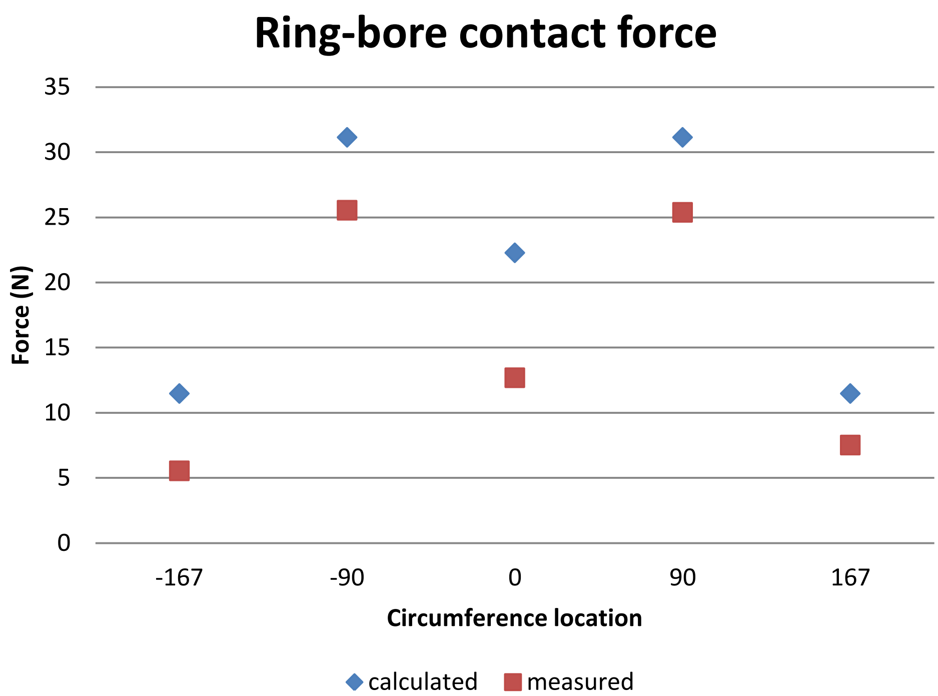

Figure 6-4 Measured and calculated contact forces

It was found from Figure 6-4 that the model predicted contact forces are higher than the measured forces at all five locations. However, they show the same contact force distribution. That is at ±90° the highest constraint forces are observed, at ±167° the constraint forces are the lowest.

The difference between the model predicted and measured absolute contact forces may be attribute to the following factors: first, ring's modulus of elasticity used in the model; second, the measured ring free shape, as it is a discrete description of the ring defining the ring radius at certain given locations; third, it was observed from the measurement that the ring may not contact with the load cells at their centers, thus the contact locations may slightly change as specified previously.

Another plot with the contact forces all normalized by the one at the ring back is shown in Figure 6-5.

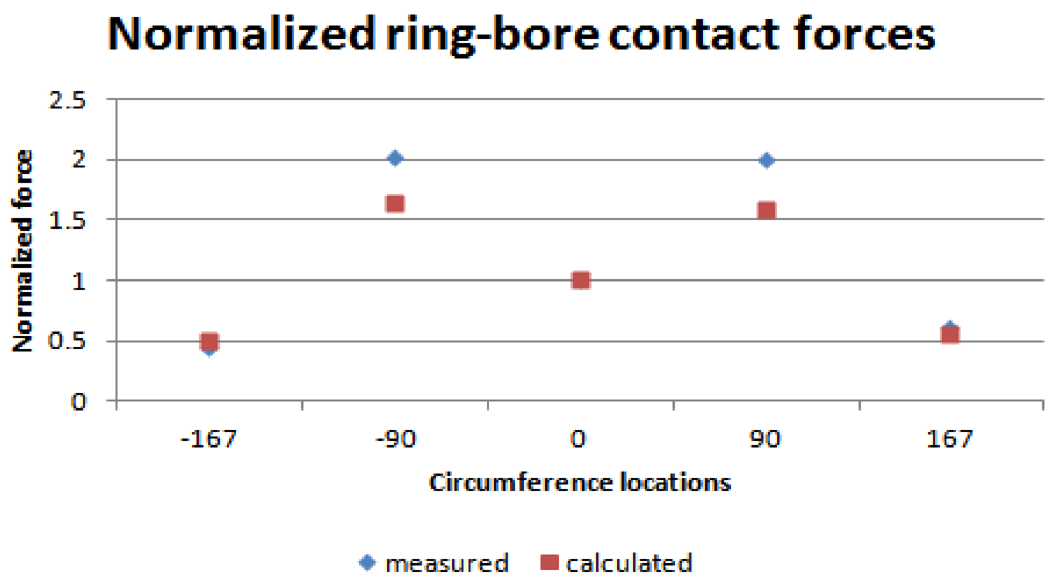

Figure 6-5 Normalized measured and calculated contact force

Great agreement is found between the measured and predicted normalized ring/cylinder bore contact forces. As a result, the FEA model is proved to predict the constraint force at the ring/cylinder wall interface. This provides details at the interface that can be adopted by other software for gas dynamics, friction and wear analysis, etc.

6.3 Piston Ring/Cylinder Bore Conformability Test

Another experiment conducted to validate the numerical ring/cylinder bore contact model is the ring/core conformability test. This is a straightforward method and the schematic diagram of this experiment is shown in Figure 6-6.

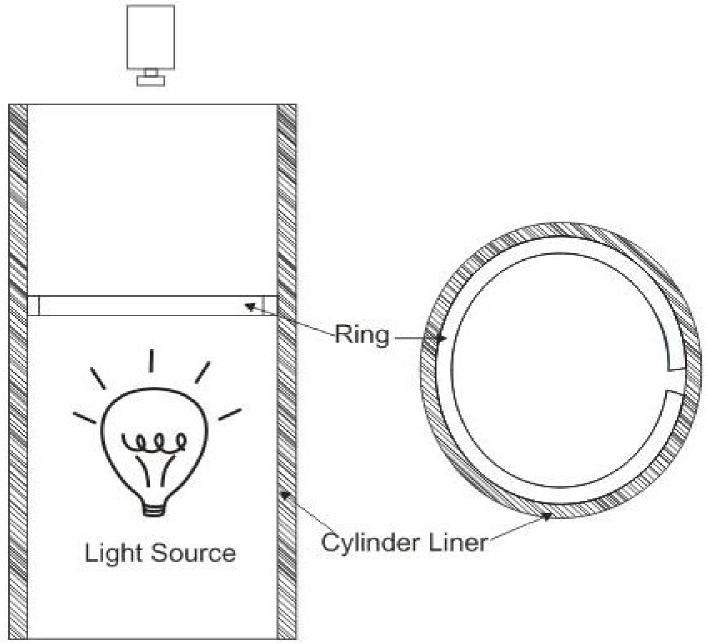

Figure 6-6 Ring "light-tightness" measurement

The experiment is conducted by installing the piston ring into the cylinder liner. In this case, the ring conforms to the cylinder bore. A light source is provided at one side of the ring and an observer is placed at the other side to detect light. If the ring well conforms to the cylinder bore, there should be no light; while if light is detected at any circumferential location, it means the ring separates with the bore at that location. This observation result is shown in Figure 6-7 with the same ring modeled in the previous chapters.

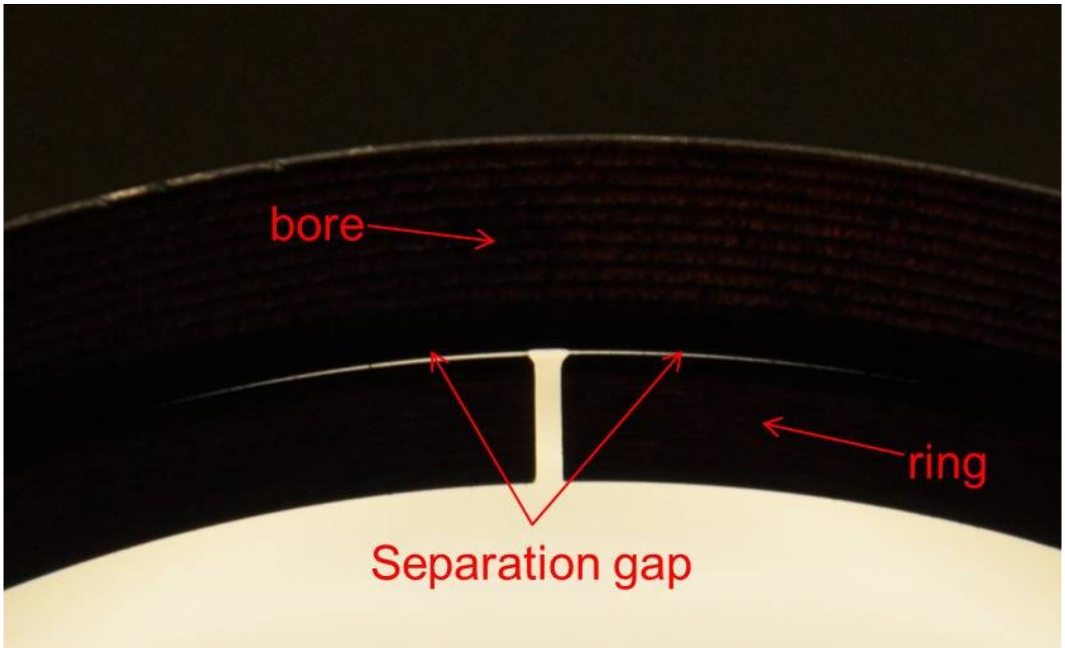

Figure 6-7 Ring “light-tightness” measurement result

This measurement observation showed that light was detected at the ring end gap up to about 15° away from the end gap in both directions. This means the ring separated from the cylinder wall near the ring tips. The light-tightness measurement (ISO6621 2) confirms the FEA result.

Chapter 7 SIMULATION ANALYSIS OF RING DYNAMICS AND TRIBOLOGICAL BEHAVIOR

7.1 Introduction

In this chapter, a commercial software package CASE is used to simulate the ring pack behavior. The focus is on the second ring dynamics due to different ring pack designs. In the second part of this chapter, the 3D ring behavior under dynamic load during an engine cycle is given. The ring deformation, dynamic twist angles, constraint loads are all calculated. At the end, the friction and lubrication behavior is analyzed with the consideration of the variation along the ring circumference.

7.2 Second Ring Flutter and Collapse Simulation with CASE

Analytical tools are widely used in design and troubleshooting process by the engine makers nowadays since it evaluates the design with high fidelity and much more time and cost effective than prototype. CASE is a code analyzing the cylinder-kit for four stroke IC engines. The cylinder-kit tribological behavior and engine loss associated with the cylinder-kit system can be analyzed. The example given in this section is a study on the second ring flutter and radial collapse for a heavy-duty diesel engine using CASE [79].

Second ring fluttering is the consequence of external force unbalance, especially between gas pressure force and inertial force. The other loads acting on the ring, including friction force, oil film squeezing force, etc, are relatively small in comparison [17]. It is noted that while the second ring friction is relatively low, the friction forces of the oil ring and the top ring during high cylinder pressures can be large. However, this study is only evaluating the forces on the second ring that cause it to flutter. Also, only the second ring flutter and collapse that occurs around top dead center (TDC) firing conditions is described in this study. This region is also considered the most important region for ring fluttering and collapse because of its significance on blowby and oil consumption.

At the start of the compression stroke (180 DEG), the second ring sits against the bottom flank of the piston groove. At this time the inertial force is holding the ring down as shown in Figure 7-1 for a general case. In Figure 7-1, negative direction denotes the downward direction.

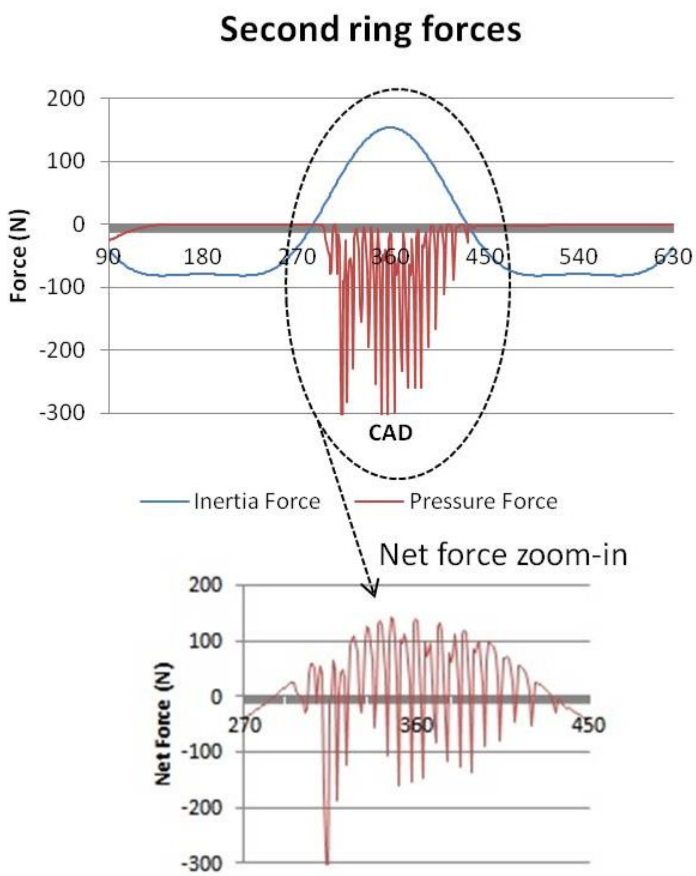

Figure 7-1 Second ring inertial force, gas pressure force and zoom-in net force

As the piston starts moving upward compressing the gases in the cylinder, the pressure in the cylinder will start building up. As a result, gases will leak past the top ring into the second land region and will start pressurizing the second land. The pressure buildup in the second land will be delayed from the pressure in the cylinder. The second land pressure will tend to hold the second ring down (Figure 7-1 and Figure 7-2 Stage I).

In the middle of the compression stroke (280 DEG), the inertial force acting on the ring will change directions. Prior to 280 DEG the inertial force holds the ring down. After this point the inertial force will push the ring upward. If it becomes higher than the downward pressure force acting on the ring, the ring will lift (Figure 7-2 Stage II).

Under these conditions, the ring moves upward to the top flank of the groove. As a result the ring creates a seal with the top side of the groove (Figure 7-2 Stage III). Gas pressure in the land above the second ring increases since gas is not allowed to flow around the side of the second ring. This gas pressure force may then surpass the ring inertial force which is holding the ring up and consequently push the ring back toward the groove bottom (Figure 7-2 Stage IV). Once the ring is pushed downward off the top side of the groove, the pressure that has built up above the ring will release around the ring sides. At this point, the pressure above and below the ring will equalize and there will be no net pressure force acting on the ring (Figure 7-2 Stage II). The major force that remains acting on the ring is the inertial force, which drives the ring back up to the top side of the ring groove.

Once the ring is back on the top side of the ring groove, the cycle starts again. Pressure builds up until it pushes the ring down. Pressures equalize which allows the inertia to push the ring back up. This continues to repeat and is called ring fluttering (Figure 7-2).

The fluttering will continue until some point at which the pressure can push the ring to the bottom side of the groove. This is often at about 450 CAD when the inertia force once again changes direction and pushes the second ring down (Figure 7-1).

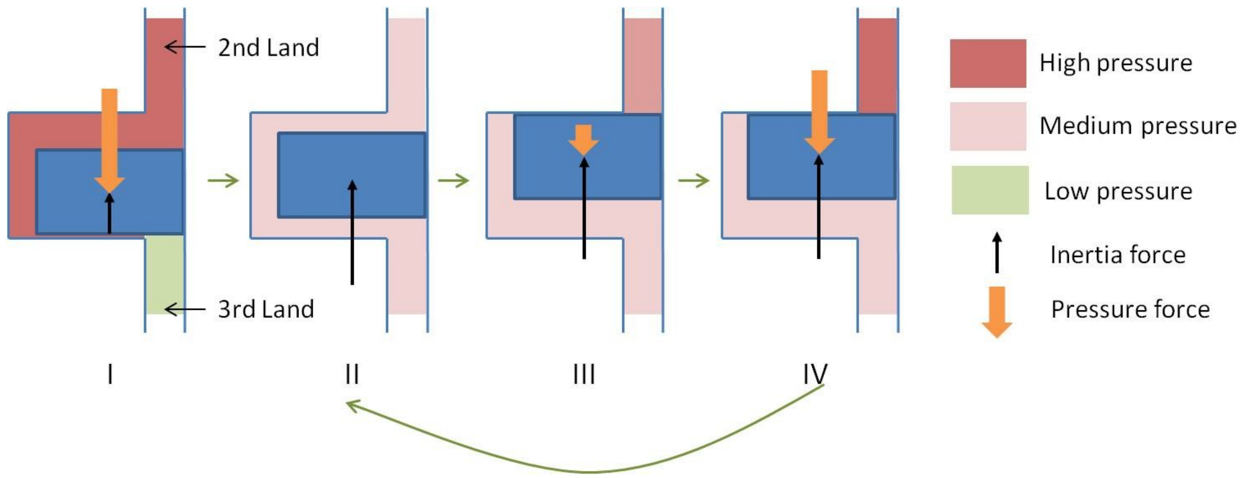

Figure 7-2 Second ring fluttering scenario

When the ring is on the top side of the ring groove, the pressure force not only pushes the ring downward, but it also acts on the front face of the ring pushing it radially inward (Figure 7-3 Stage II). If the gas pressure acting on the ring face exceeds the tension of the ring plus the gas pressure acting on the back of the ring, then the ring will collapse radially inward (Figure 7-3 Stage III). Once it collapses, the gases will escape past the ring face and equalize all around the ring (Figure 7-3 Stage IV). Once again, there will be no net gas pressure on the ring and the elastic tension of the ring will force the ring back out to the cylinder wall (Figure 7-3 Stage V). This cycle will repeat, causing an unstable collapse. Figure 7-3 is a pictorial explanation of this mechanism with a taper faced ring for illustration as most second rings for a diesel engine have a taper face. High pressure gases can infiltrate between the ring face and the cylinder wall if the ring face is not flooded with lubrication oil.

It will depend on the ring and piston design which of these two conditions occur: 1. Ring fluttering or 2. Ring collapse. It may even be possible that both conditions occur at the same time. In either case, the second ring is not sealing the gases and allows the gases to flow either around the ring (in the fluttering case) or past the ring face (in the ring collapse case). Because the second ring is not sealing gases in these two cases, high blowby could occur.

Fluttering or collapse of the second ring requires that the ring lifts to the top side of the ring groove and seals the gases. If inertia is not strong enough to overcome the gas pressure that is holding the ring down, the ring will remain seated on the bottom side of the ring groove. There will be no ring flutter nor ring collapse.

The potential for ring fluttering and/or ring collapse is influenced by the operating conditions of the engine. High intake manifold pressure may push more gas past the top ring. Thus the second land gas pressure is higher and may tend to hold the second ring down, preventing it from lifting. The ring inertial load increases quadratically with engine speed. High inertial force could make the second ring more susceptible to lifting. Besides the operation conditions, design parameters such as ring twist, and land clearance could also affect ring fluttering as they determine the area on which the gas pressures act and ultimately the forces acting on the ring. These influences will be discussed later in this study.

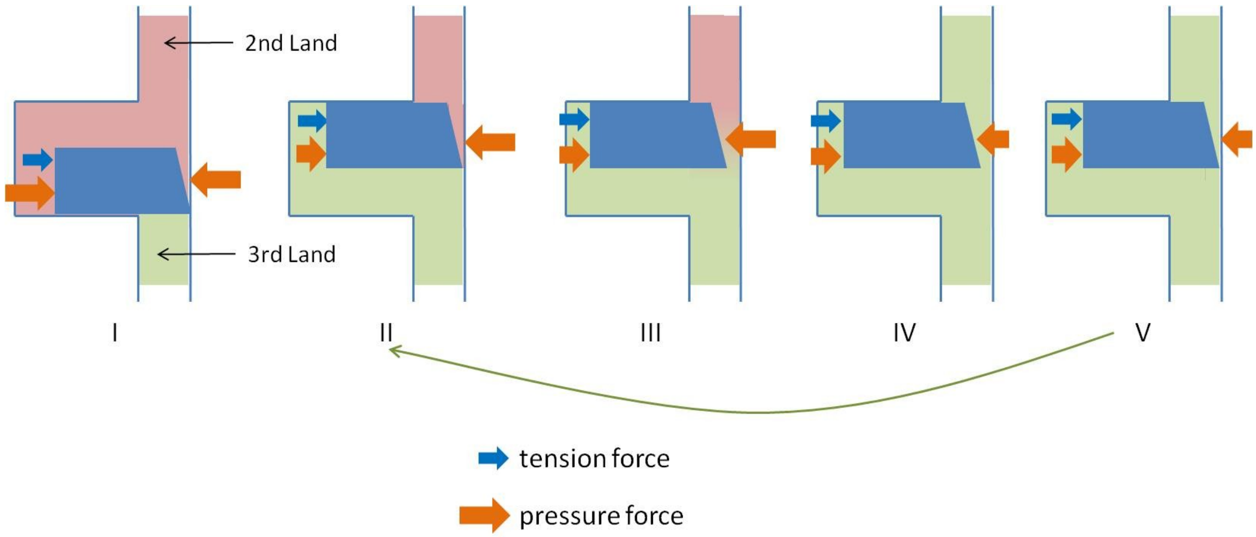

Figure 7-3 Second ring radial collapse scenario

The engine modeled in this study is a diesel engine. This work focuses on the full load rated power condition at 1900 RPM.

Two different ring pack cases are studied in this work, including ring static twist, and end gap size influences on second ring fluttering.

Two different ring pack cases are studied in this work, including ring static twist, and end gap size influences on second ring fluttering.

Case 1 uses a negative static twisted second ring. The key geometries of the ring pack are shown in Table 7-1.

Table 7-1 Ring pack configuration for Case 1

ring static twist	Negative
Top ring end gap	0.45 mm
second ring end gap	2.00 mm

With this configuration, the nominal engine blowby was found to be over 21 L/min/L-disp. The in-cylinder pressure, second land gas pressure as well as top ring and second ring in-groove motions are shown in Figure 7-4.

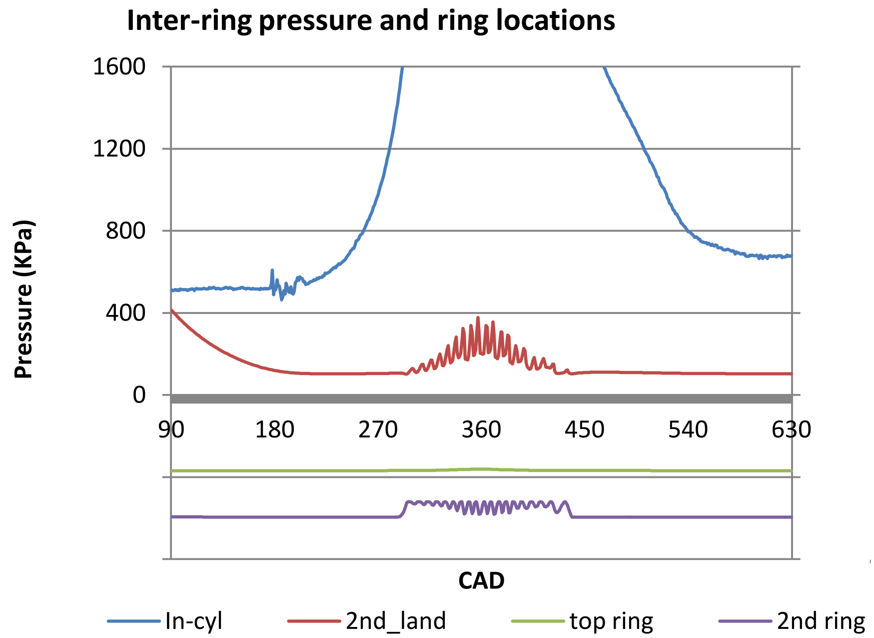

Figure 7-4 Inter-ring, second land gas pressure and ring in-groove locations

From Figure 7-4, it is obvious that the second ring lifts to the top side of the ring groove at about 270 DEG because of the inertial force acting on the ring. The second ring then flutters off the top side of the second ring groove. This fluttering continues until the inertial force of the ring changes direction at about 450 DEG and pushes the ring down.

It should be noted that the pressure above the second ring (i.e. the second land pressure) fluctuates with the ring fluttering. This shows how the pressure builds up, the ring is pushed down off the top side of the ring groove, pressure equalizes, inertia pushes the ring up, and the cycle repeats several times.

Also it can be seen that in general the second land pressure is very low. As a result, the pressure above the top ring (cylinder pressure) is always greater than the pressure below the top ring (second land pressure). This keeps the top ring seated on the bottom of the groove and there is never any reverse flow of gases back into the combustion chamber (blowback).

In this case, the second ring was fluttering. However, under the right conditions, the ring could have collapsed radially inward instead of flutter or could have collapsed and fluttered simultaneously.

Unlike Case 1, a positive static twisted second ring was adopted for Case 2. In order to prevent the second ring from lifting, the second ring end gap size is reduced by 50% in order to keep the second land gas pressure relatively high. This configuration is expected to allow more pressure to build up above the second ring such that the second ring does not lift nor flutter. These geometries are shown in Table 7-2.

Table 7-2 Ring pack configuration for Case 2

second ring static twist	Positive
Top ring end gap	0.45 mm
second ring end gap	1.00 mm

The in-cylinder pressure, second land gas pressure, top ring and second ring in-groove motions are plotted in Figure 7-5 for Case 2 and it is clear that second ring fluttering does not occur for this case. This is because the pressures above the second ring are high enough to prevent inertia from lifting the second ring. Since the ring remains bottom seated, as the second land pressure build up, it holds the second ring down and the ring does not flutter.

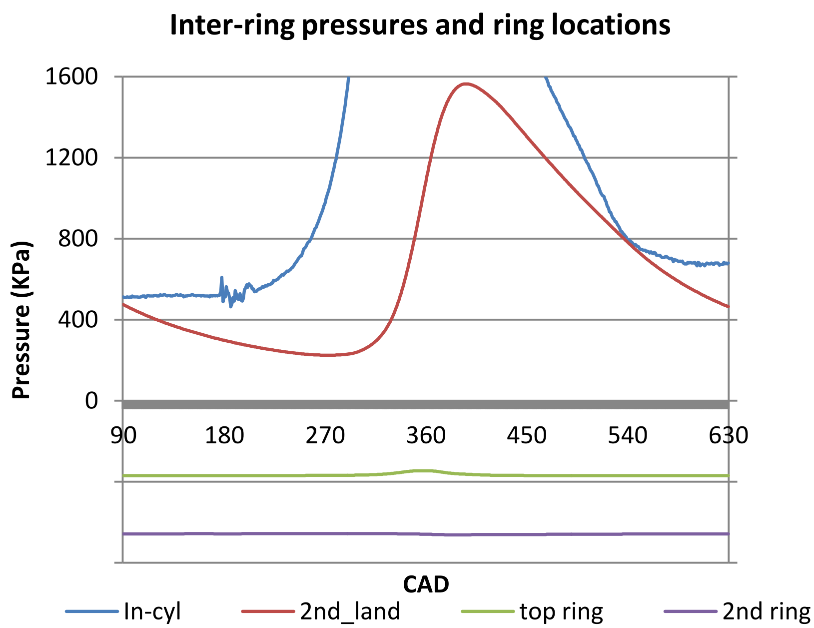

Figure 7-5 Inter-ring, second land pressures and ring in-groove locations

It was found that engine blowby for Case 2 is reduced by 15% compared to Case 1. This is because in Case 1 the second ring is not sealing the gases very efficiently and allowing the gases to flow around the ring as it flutters.

However, it should be noted that the second land pressure builds up higher than in Case 1. This is because the second ring gap is smaller and because it is positive twist. Both features allow pressure to build up quicker above the second ring holding it down and preventing inertial from lifting the ring. If the second ring does not lift before top dead center it will not flutter.

If the second land pressure becomes too high, there can be a time when the cylinder pressure falls below the second land pressure. This can lead to reverse flow of gases upward into the combustion chamber and possible lift of the top ring. This condition may be bad for oil consumption because the reverse gas flow may carry oil back into the combustion chamber increasing oil consumption.

Figure 7-6 shows a comparison of the second land pressures for Case 1 and 2. It can be seen that at 270 DEG the Case 2 second land pressure is higher than Case 1 pressure. It is high enough to hold the ring down and prevents the fluttering of the second ring for Case 2. Since Case 1 has second ring fluttering, the ring is not sealing the gases and the second land pressure is very low. Also it is erratic because of the gases flowing past the fluttering second ring.

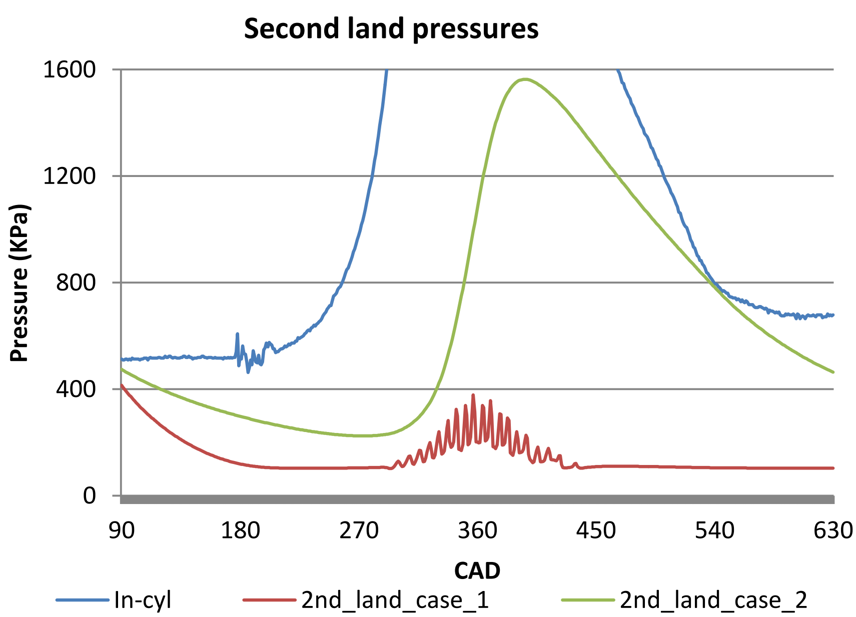

Figure 7-6 Second land pressure comparison

Because of the difference in ring in-groove motions and second land gas pressures, the instantaneous gas flow across the second ring is found significantly different for the two above cases. The instantaneous gas flows through the second ring end gap and ring sides are shown in

Figure 7-7 (a) and (b) respectively. It was found that the major gas flow across the second ring for Case 1 is the flow around the sides of the ring between the ring and groove (Figure 7-7 b). And high-level gas flow fluctuation occurs with the fluttering second ring case due to the opening and closing of this gas flow path around the ring sides.

The gas flow through the second ring end gap is relatively low for Case 1 compared to Case 2, due to the lower pressure above the second ring and also because the gases are escaping past the sides of the ring for Case 1. However, for Case 2, minimal gas travels around the sides of the ring as the ring seals against the bottom flank of the groove during the entire cycle. The only major gas flow path is through the ring end gap (Figure 7-a). And this gas flow through the ring end gap is stable and much higher than that for Case 1.

In Figure 7-7, positive gas flow is defined as downward flow, from the second land to the third land, or from the second groove into the third land. It has been found that the gas flow through ring end gap is higher for Case 2 and gas flow around the ring sides is significantly higher for Case 1. The resultant overall downward gas flow (blowby) for Case 2 is still lower than that for Case 1 in this study.

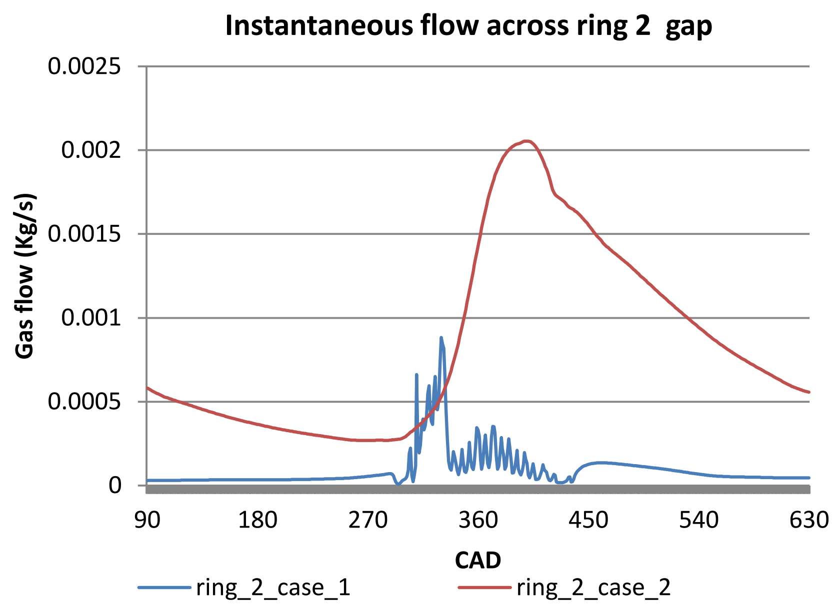

(a) Instantaneous gas flow across second ring end gap

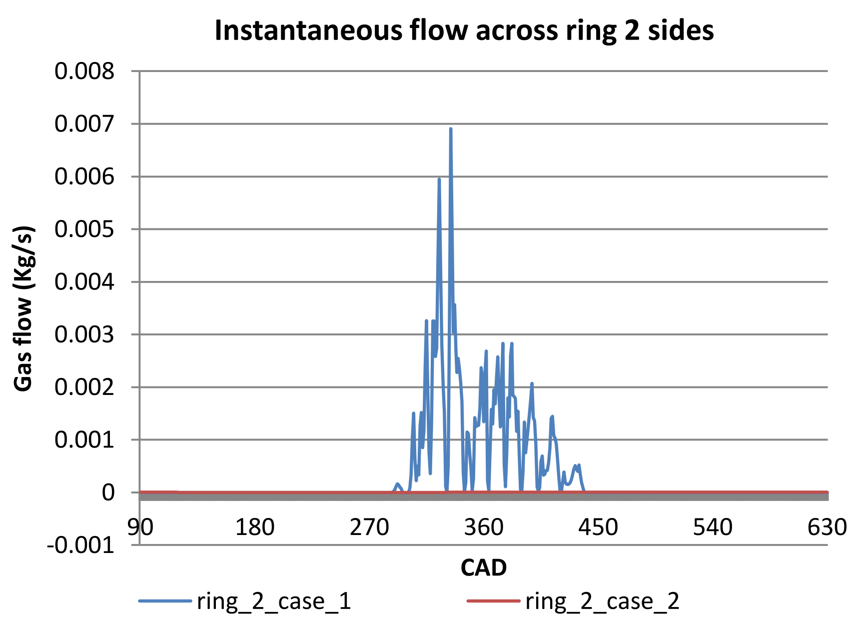

(b) Instantaneous gas flow across second ring sides

Figure 7-7 Instantaneous gas flow across second ring

As described above, the lift of the second ring and seating on the top side of the groove is a necessary precursor for the second ring to flutter or collapse. This is illustrated in the two cases cited in this study. In Case 1, the second ring lifts and then flutters off the top side of the ring groove. In Case 2, the second ring remains bottom seated. This can be explained by the different forces acting on the ring for these two cases.

As discussed in the previous section, Case 1, with a negative static twisted second ring, forms an outer edge sealing between the ring and groove bottom sides. This configuration allows gases to flow into the crevice between the ring and groove bottom sides. As a result, the net downward gas pressure force becomes very low and the ring is much easier to be lifted by the inertial force acting on the ring (Figure 7-8). On the contrary, Case 2 configuration with a positive second ring static twist seals the groove bottom at the inner bottom corner. The inner edge sealing prevents higher pressure gas moving beneath the ring. Thus, a higher gas pressure gradient across the ring results in a larger downward pressure force. The ring is then harder to be lifted by inertial force. Figure 7-8 is a simplistic illustration showing the gas pressure forces acting on the sides of the rings.

The top and second ring end gaps can also significantly affect second ring fluttering or collapse. The smaller second ring end gap in Case 2 blocks gases from flowing past the second ring. As a result, the pressure can build up quicker above the second ring. This higher pressure above the ring will help hold the ring down so that inertia cannot lift the second ring.

A larger top ring end gap can allow more gases to flow past the top ring also building up pressure in the second land region.

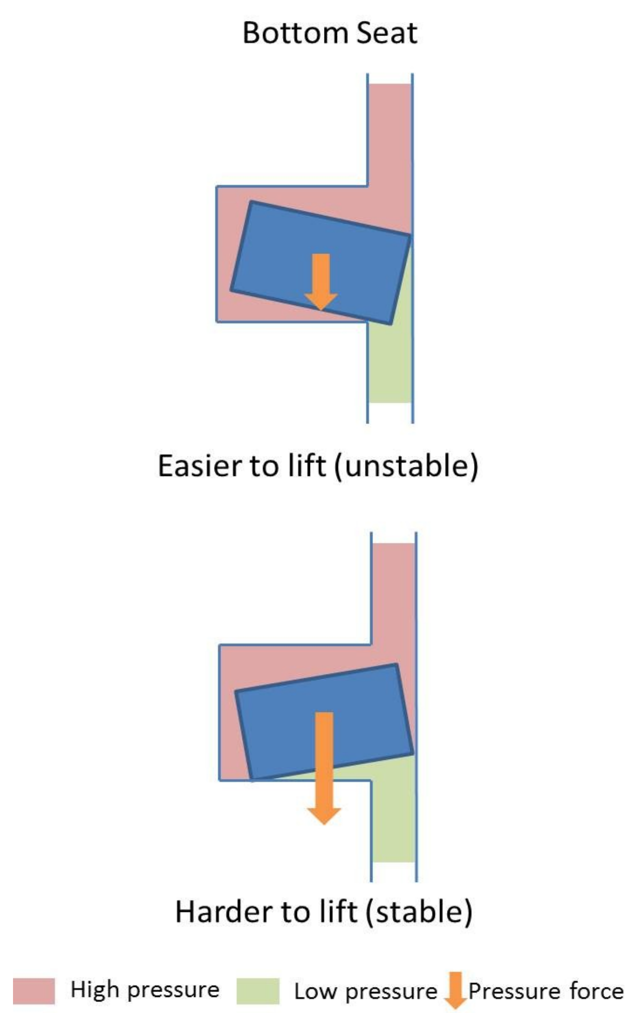

Figure 7-8 Ring bottom seating stability

Similarly, the ring top seating stability (Figure 7-9) can be interpreted similarly as for the bottom seating condition. However, it should be noted that since a negative twisted ring is easier to move down, it will be less likely to collapse. Conversely, the positive twisted ring will be more difficult to push down; therefore the ring will be more likely to collapse radially inward. In other words, the pressure to push the positive twist ring has to be higher to push the ring down off the top side of the groove. However, that high pressure is also acting on the ring front face trying to push the ring backwards off the cylinder wall. Therefore it is more likely that the pressure force pushing inward on the ring face can collapse the ring before the ring is pushed downward.

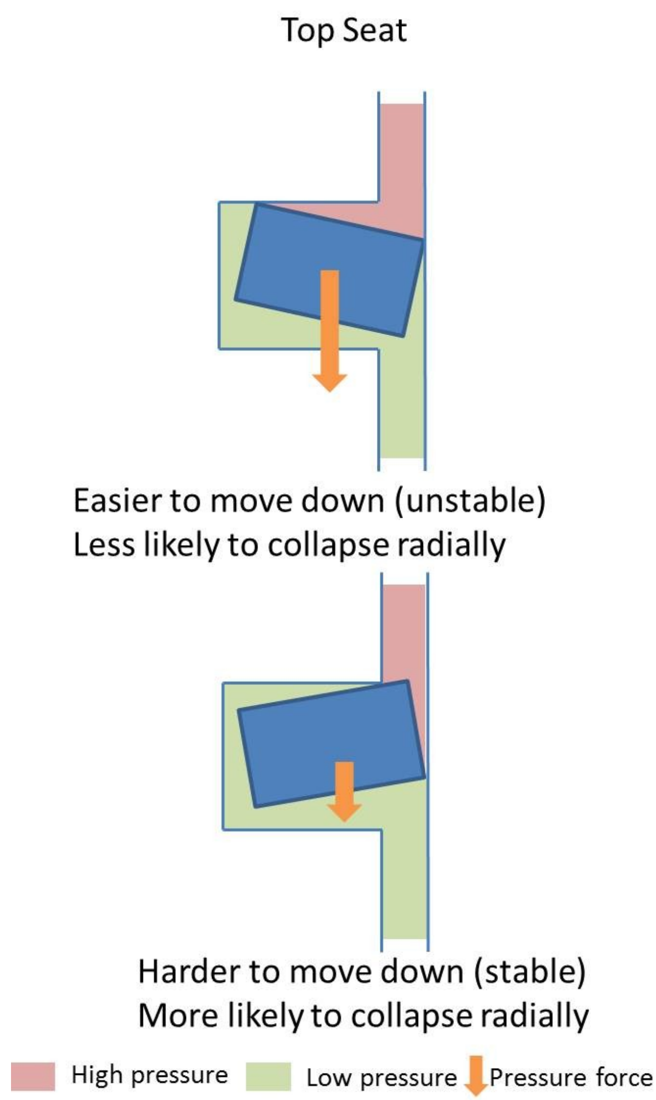

Figure 7-9 Ring top seating stability

Overall, the configuration with positive static twist and a small second ring gap tends to increase the pressure force holding the second ring down and promoting second ring in-groove stability. A cross-over point is likely to occur for this configuration as seen from Figure 7-5:

second land pressure is very close to in-cylinder pressure, yet it does not surpass the in-cylinder pressure. This positive twist ring is also more likely to collapse. Conversely, the configuration with negative static twist, and a large second ring gap will tend to allow the second ring to lift and subsequently flutter. However, ring radial collapse is less likely to occur.

A sensitivity study was conducted to learn the influence of top ring and second ring end gap sizes on second ring lift. As a result, the study was done using a positive static twist second ring. It may be easier for conditions to result in fluttering with negative twist rings, however, the basic fundamental reasons for the second ring to lift and flutter would be the same as a positive twist ring. The ring end gap sizes for the sensitivity study are shown in Table 7-3. It should be noted that the 0.15 mm top ring end gap in a diesel engine would probably not be possible because of end gap butting. However this was modeled to evaluate the theories of fluttering.

Table 7-3 Ring end gap size for sensitivity study

	Top ring (mm)	second ring (mm)
Small	0.15	0.5
Nominal	0.45	1.0
Large	0.75	2.0

Two phenomena were monitored for this sensitivity study: 1. second ring lift and 2. gas pressure cross-over point between the in-cylinder gas pressure and the second land pressure (Figure 7-10).

These two phenomena are important for the power cylinder system. Ring lift influences ring and gas dynamics, as discussed in the previous sections. The cross-over point indicates the start of a condition where the pressure between the top and second rings (second land) exceeds the in-cylinder pressure and can result in reverse blowby of gases into the combustion chamber. If the blowback gases contain oil, then it may contribute to oil consumption.

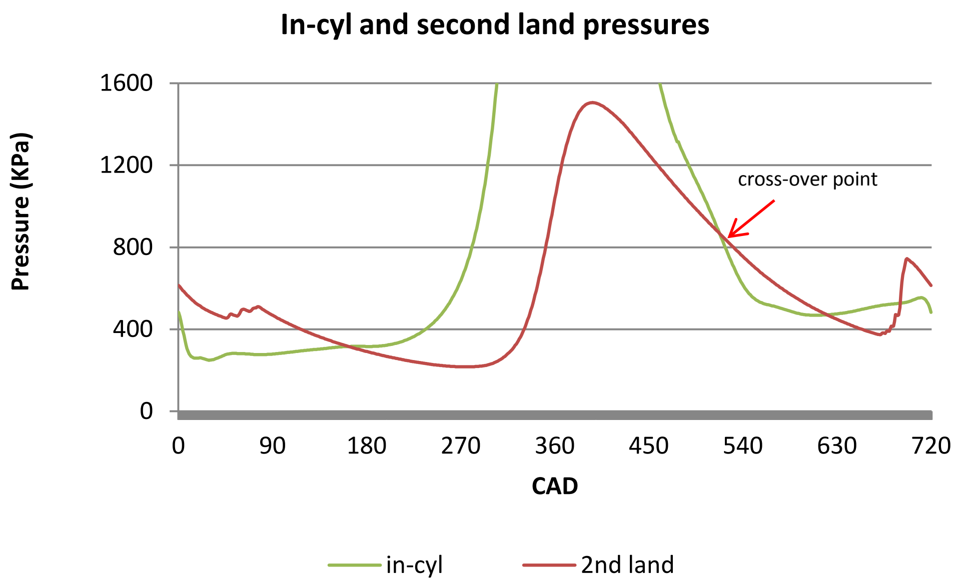

Figure 7-10 In-cylinder pressure and second land pressure with cross-over point

The engine blowby data for these cases are normalized by the Case 2 blowby discussed in the previous section and are shown in Table 7-4. In addition, the second ring lift and fluttering cases, and the cases where cross-over point occurs are indicated under the normalized blowby values in Table 7-4.

It was found that the second ring lift occurs when the top ring end gap is small and the second ring end gap is relatively large. This is because for this ring pack configuration, the second land gas pressure is low. Thus the ring inertia force can easily overcome the pressure force to lift the ring.

The cross-over point between the in-cylinder pressure and second land gas pressure is found for large top ring end gap and small second ring end gap cases. This cross-over point results from the fact that the second land gas pressure is higher and decreases with a lower rate than the in-cylinder pressure does. Reverse gas flow occurs during the cross-over region.

If the ring lifts or flutters, there is no cross-over point because the second land pressures are so low.

Table 7-4 Percentage engine blowby and the indication of second ring lift or cross-over point

Normalized engine blowby		Top ring end gap		
		Small	Nominal	Large
second ring end gap	Small	47.2% Stable	67.6% Cross-over	80.4% Cross-over
	Nominal	59.5% Lift	100.0% Stable	127.4% Cross-over
	Large	66.0% Lift	116.1% Stable	171.5% Stable

The inter-ring gas pressures and the ring in-groove locations for the ring lift case can be found in Figure 7-11 based on the small top ring end gap, large second ring end gap case. This clearly shows that the second ring stays against the groove top around TDC. The top ring still stays bottom seated near the firing TDC. This is very similar indication as the second ring is fluttering:

the second land pressure is very low and erratic. However, in this case, the second ring is collapsing instead of fluttering near the firing TDC. The pressure behind the second ring is very small because the ring is seated on the top side of the groove. Therefore the pressure is equal to the third land pressure. The radial force on the ring front face from lubrication oil hydrodynamic pressure generated when the ring is sliding along the liner and the infiltrated gas pressure if the ring is not fully flooded then become higher than the ring tension and back pressure force. This radial inward net force pushes the ring away from the cylinder bore (Figure 7-3). This hydrodynamic contact pressure is calculated by solving a Reynold's equation with gas pressures as boundary conditions. A direct gas flow path across the second ring is formed when the ring collapses. Figure 7-12 shows the instantaneous gas flow through the second ring end gap and the ring face. The gas flow spikes near TDC indicate the occurrences of ring collapse, as gas can also flow past the second ring through the ring face and cylinder bore clearance. This corresponds to the second land gas pressure fluctuation in Figure 7-11.

In this case, the forces on the ring face were sufficient to collapse the ring before the ring could be pushed axially downward.

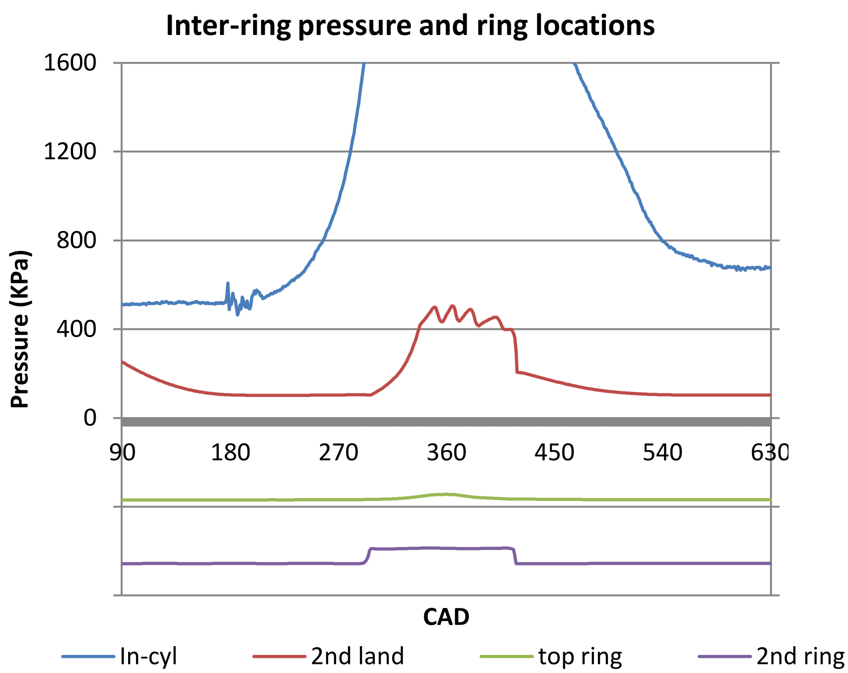

Figure 7-11 Inter-ring pressure and ring locations for second ring lift case

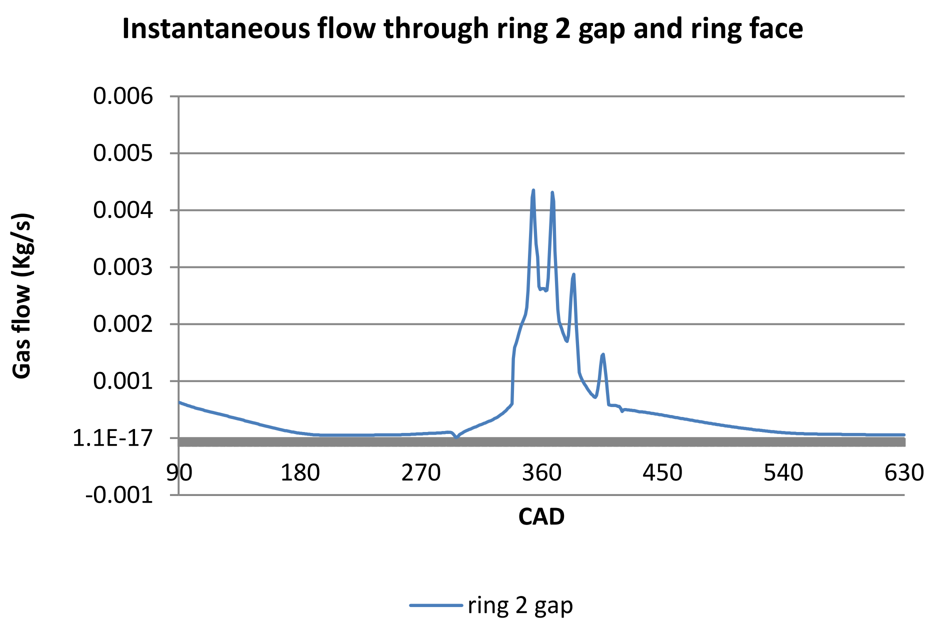

Figure 7-12 Instantaneous flow through second ring end gap and ring face

The in-cylinder gas pressure and second land pressure are shown in Figure 7-13 for the large top ring end gap, small second ring gap case for which a cross-over point is found. It is obvious that the second land gas pressure is higher than the in-cylinder gas pressure from about 420 DEG to 600 DEG. During this period, the in-cylinder gas pressure decreases faster than the second land pressure, and the gas in the second land can flow back into the combustion chamber. The top ring is lifted and seats against the top flank of the groove. Top ring fluttering does not occur which causes the second land gas pressure to remain higher than the in-cylinder pressure. The second ring stays bottom seated throughout the cycle. The reverse gas flow that occurs from about 430 DEG to 600 DEG through the top ring end gap as the top ring seats against the groove top side is shown in Figure 7-14. Along with this reverse gas flow, lubrication oil carried by the gas flow travels back into combustion chamber. Thus lubrication oil consumption may increase [14].

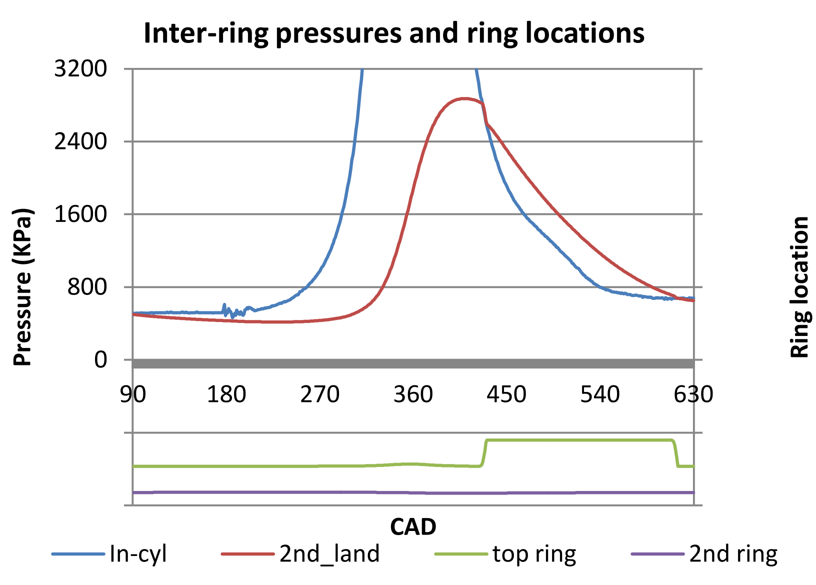

Figure 7-13 Inter-ring pressures and ring locations for second ring non-lift case

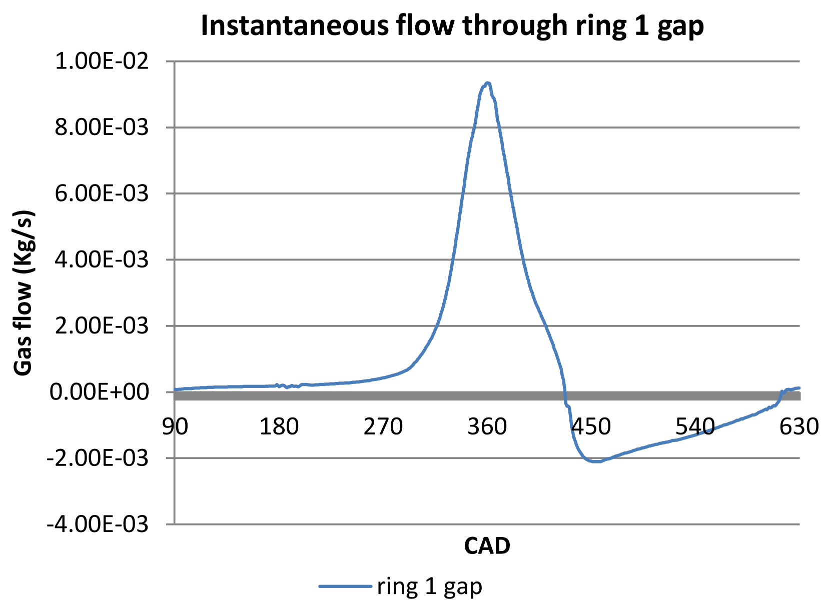

Figure 7-14 Instantaneous flow through top ring end gap for second ring non-lift case

Ring dynamics was discussed using the software *CASE* with an emphasis on the second ring fluttering and collapse for a modern diesel engine at full load high speed condition. From this study, the following conclusions can be made:

Second ring fluttering and collapse occur because the pressure above the ring is not sufficient to hold the ring down and the ring lifts because of the inertial force. Once the ring is seated on the top side of the groove, the pressure at the region above the ring will build up and push the ring down. Inertia will lift the ring back in an unstable or fluttering manner. Ring collapse can also occur when the lubrication oil hydrodynamic force and gas pressure force on the ring face surpass the ring tension and back pressure force as the ring stays top seated.

When the second ring flutters or collapses the blowby will generally be higher. This is because the ring does not seal the gases and the gases flow past the ring. While this can cause high blowby, the pressure in the second land will be very low. This will prevent reverse blowby and the top ring from lifting.

Conversely, when the second ring is stable, the pressure in the second land will be greater. It is possible that there is a condition with the cylinder pressure falling below the high second land pressure, resulting in reverse blowby and/or top ring lifting. This could be bad for oil consumption as the reverse flow may carry oil back into the combustion chamber.

Second ring flutter can be stopped by increasing the pressure forces acting on the second ring during the early part of the compression stroke. This can be done by controlling engine factors such as intake manifold pressure and engine speed. Also it is strongly affected by the top and second ring end gaps as shown in this study.

The static twist of the second ring will also have an effect on ring flutter and collapse. A negative static twist second ring will be more likely to flutter than a positive twist ring. However if the second ring lifts, the positive twist ring will be more likely to collapse than the negative twist ring.

The ring end gaps will have a significant effect on controlling the second ring fluttering. A large top ring gap will increase the pressure above the second ring. A small second ring gap will do the same. Higher pressure above the second ring will reduce the potential for ring flutter.

Second ring fluttering and ring collapse can have a significant effect on both engine blowby and oil consumption. Therefore it is very important to understand these phenomena and how to control them.

7.3 3D Ring Dynamic Simulation Analysis

In this section, the ring dynamics is analyzed with the consideration of 3D effect. Examples are given for a second compression scraper ring. In addition to the constraint loads from the cylinder liner and groove sides, the ring is also under dynamic load from ring inertia, pressure load from the piston lands and groove, and friction load at the ring face. The friction load is calculated as the product of the contact force from the previous CAD and the friction coefficient as specified by the user (0.01 in this study). The pressure load and inertial load are provided from the CASE simulation result for the ring. It is assumed that the pressure can only affect the ring dynamics. However, the ring dynamics and deformation do not affect to the gas flow and pressure distribution. At each CAD, the contact forces between the ring and cylinder liner, piston groove sides can be found, together with the ring deformation and twist angle along the ring circumference. The inter-ring gas pressures for the ring pack can be found in **Figure 7-15**.

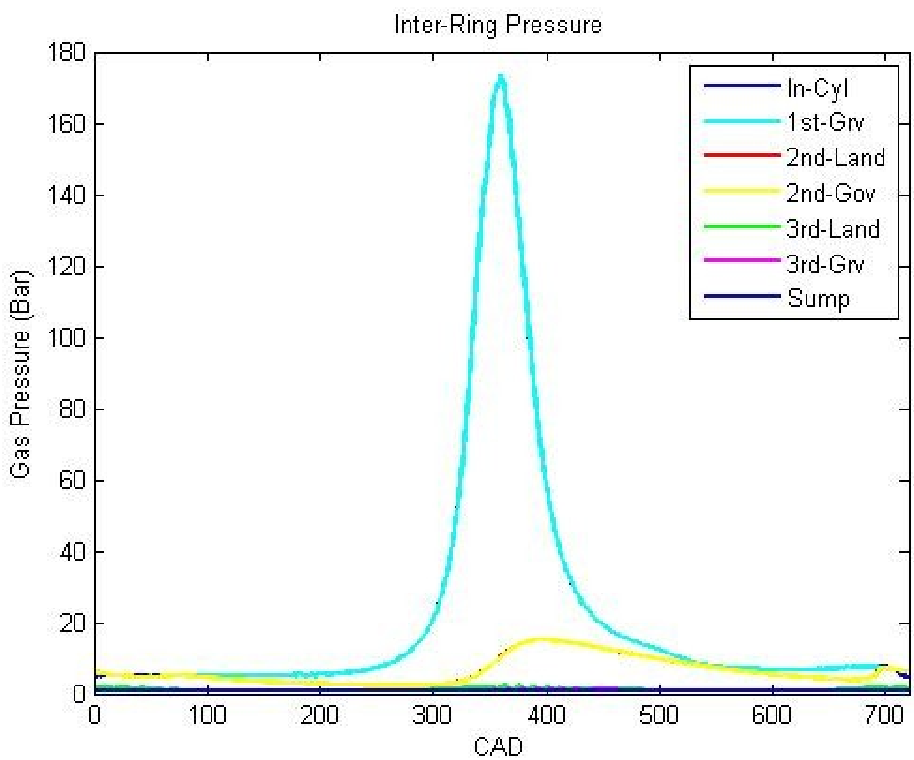

Figure 7-15 Inter-ring gas pressure

The focus of this study is the dynamics of the second ring. Thus, the pressure boundary for the second ring includes the gas pressures in the 2nd land, 2nd groove and 3rd land. The inter-ring gas pressures are predicted using CASE program.

The ring acceleration plot is shown in Figure 7-16.

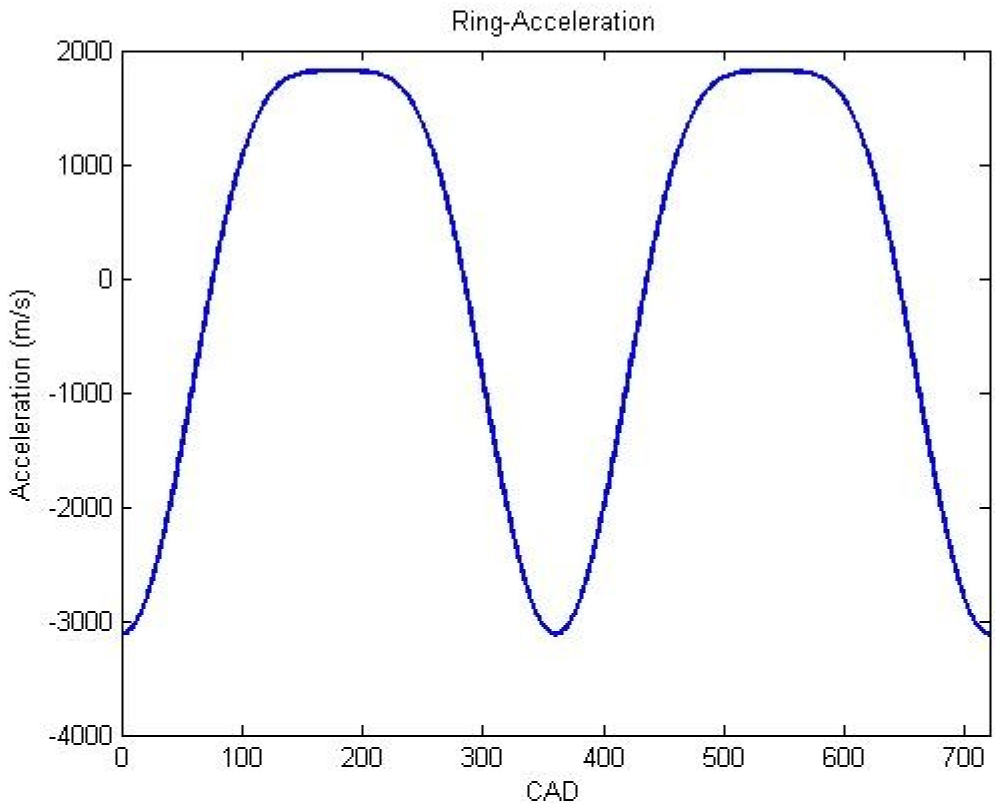

Figure 7-16 Ring acceleration

Figure 7-17 and Figure 7-18 show the ring twist angle along the ring circumference for half ring and the deformed ring shape respectively at 90 CAD. The ring deformation in the axial direction is amplified by 10 times.

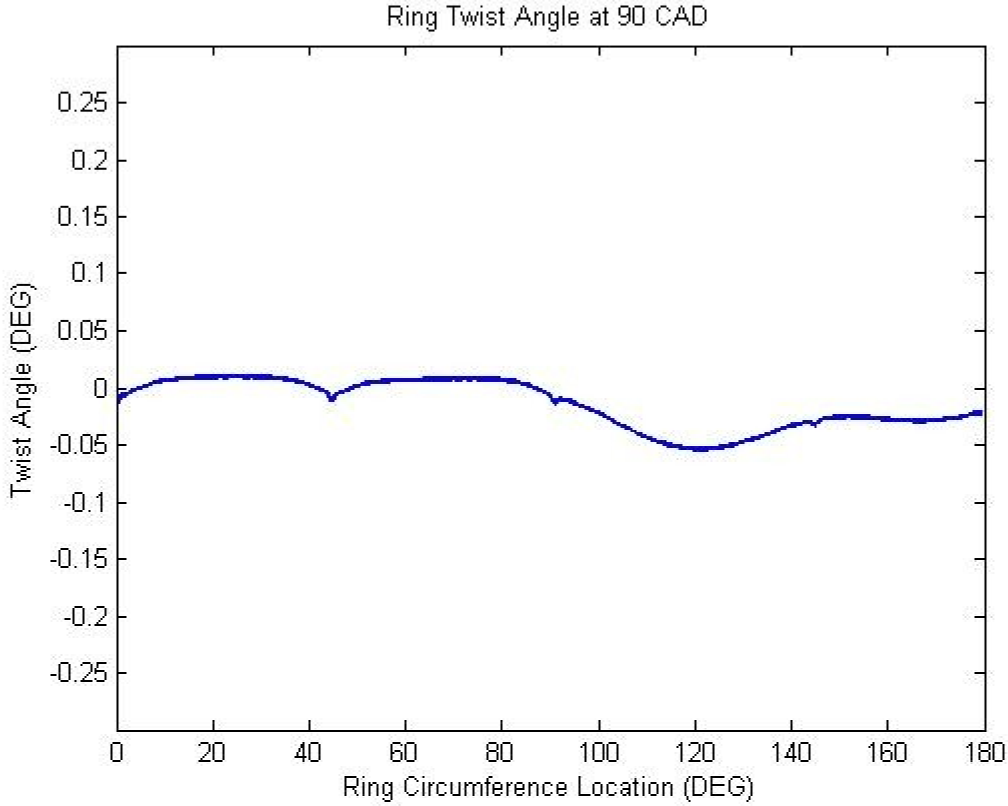

Figure 7-17 Ring twist angle at 90 CAD

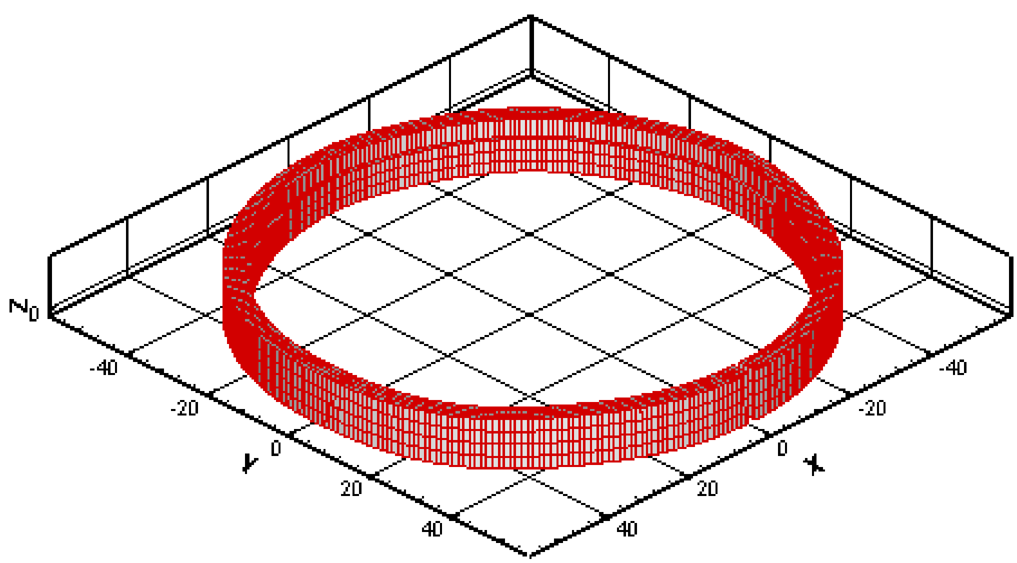

Figure 7-18 Deformed ring at 90 CAD

Table 7-5 lists the contact forces at the four potential contact points as shown in Figure 3-13.

Table 7-5 Contact forces in axial direction at 90 CAD

90 CAD (N)	Node 1	Node 2	Node 3	Node 4
0°	21.0	0.0	13.7	0.0
45°	47.1	0.0	21.7	0.0
90°	16.2	0.0	60.8	0.0
135°	0.0	0.0	74.2	0.0
180°	0.0	0.0	16.3	0.0

Figure 7-19 and Figure 7-20 show the ring twist angle along the ring circumference for half ring and the deformed ring shape respectively at 180 CAD. The ring deformation in the axial direction is amplified by 10 times.

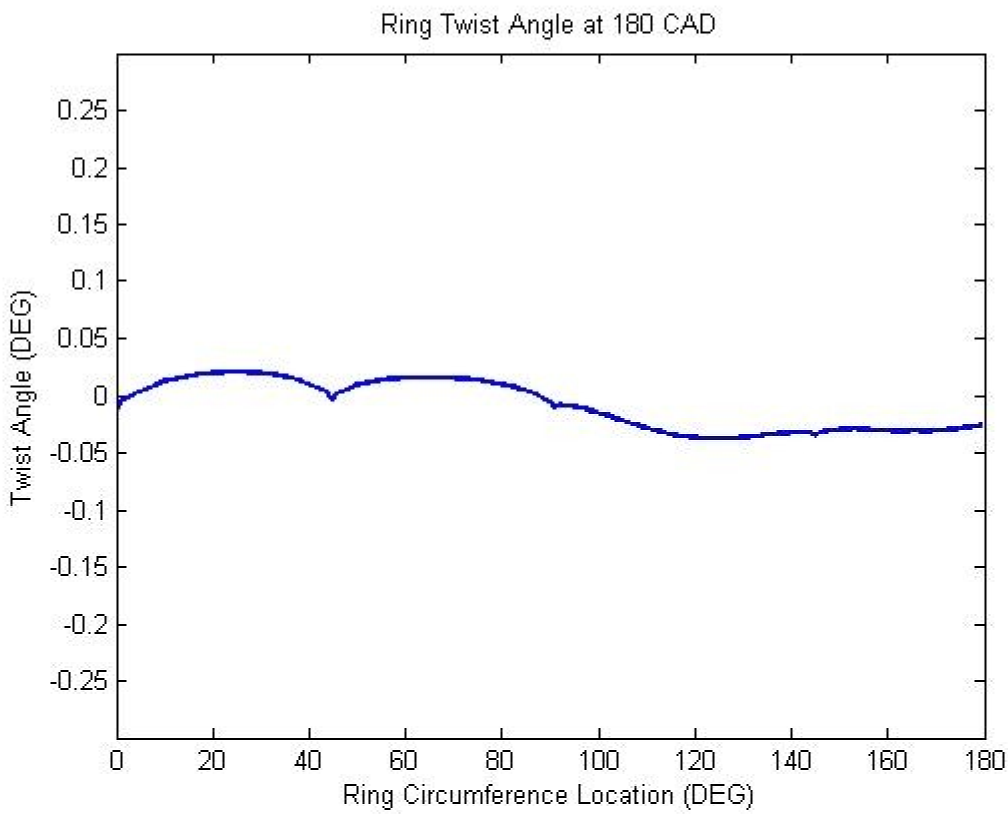

Figure 7-19 Ring twist angle at 180 CAD

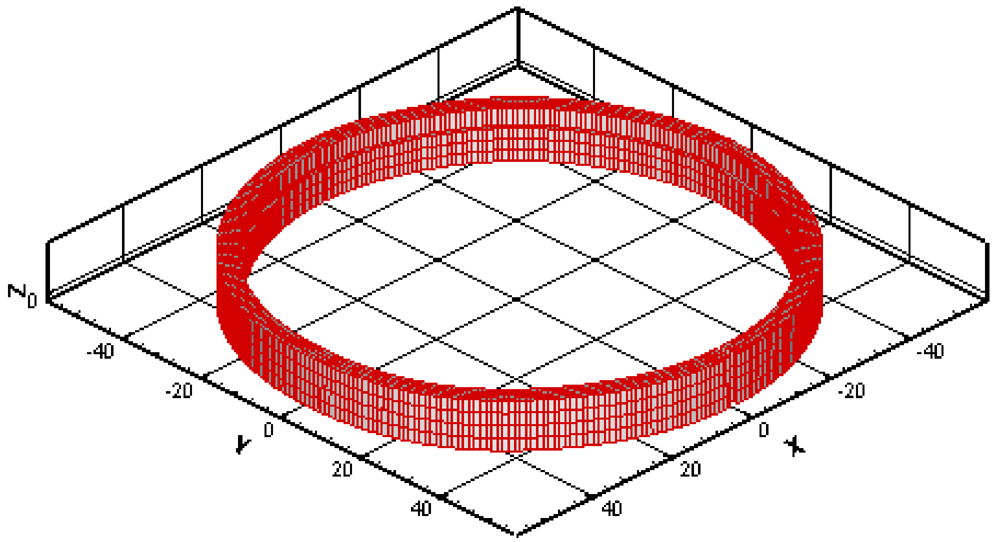

Figure 7-20 Deformed ring at 180 CAD

Table 7-6 lists the contact forces at the four potential contact points as shown in Figure 3-13.

Table 7-6 Contact forces in axial direction at 180 CAD

180 CAD (N)	Node 1	Node 2	Node 3	Node 4
0°	20.6	0.0	0.8	0.0
45°	43.1	0.0	0.0	0.0
90°	12.3	0.0	33.9	0.0
135°	0.0	0.0	45.2	0.0
180°	0.0	0.0	9.7	0.0

Figure 7-21and Figure7-22 show the ring twist angle along the ring circumference for half ring and the deformed ring shape respectively at 270 CAD. The ring deformation in the axial direction is amplified by 10 times.

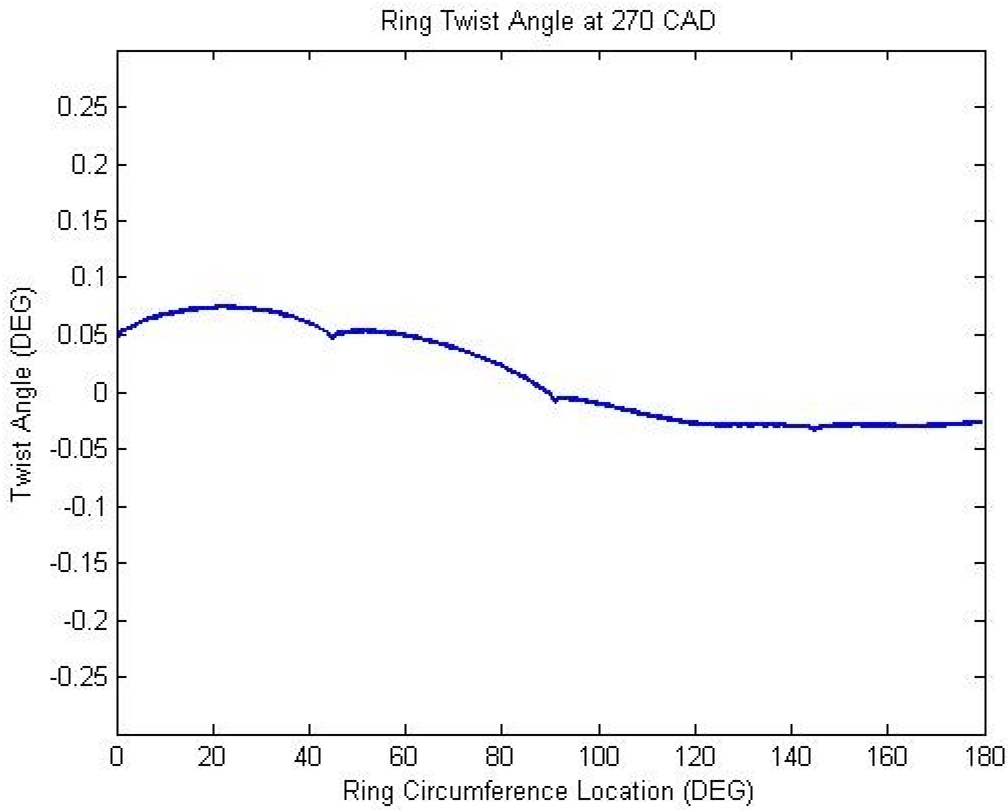

Figure 7-21 Ring twist angle at 270 CAD

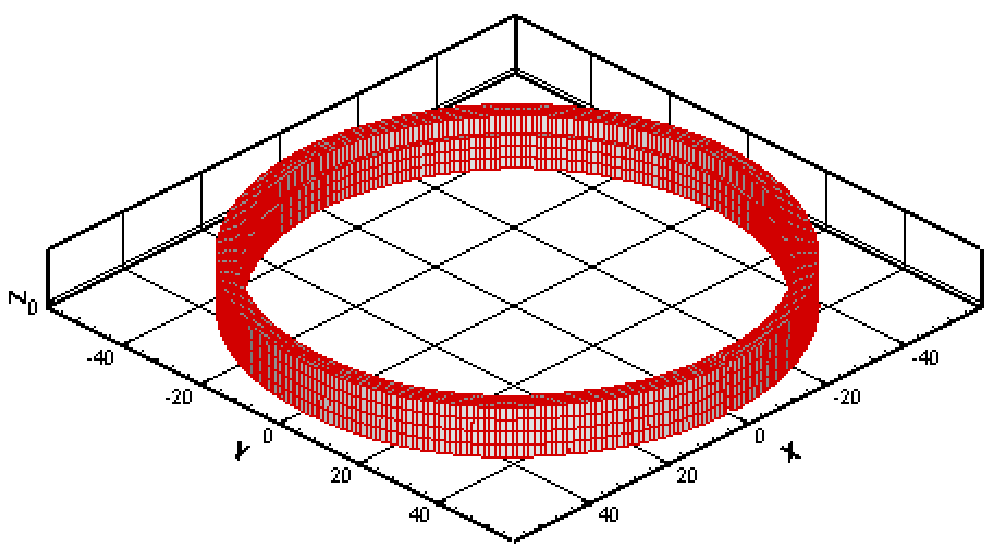

Figure7-22 Deformed ring at 270 CAD

Table 7-7 lists the contact forces at the four potential contact points as shown in Figure 3-13.

Table 7-7 Contact forces in axial direction at 270 CAD

270 CAD (N)	Node 1	Node 2	Node 3	Node 4
0°	15.4	0.0	0.0	0.0
45°	31.0	0.0	0.0	0.0
90°	17.0	0.0	17.0	0.0
135°	0.0	0.0	32.8	0.0
180°	0.0	0.0	6.7	0.0

Figure 7-23 and Figure 7-24 show the ring twist angle along the ring circumference for half ring and the deformed ring shape respectively at 360 CAD. The ring deformation in the axial direction is amplified by 10 times.

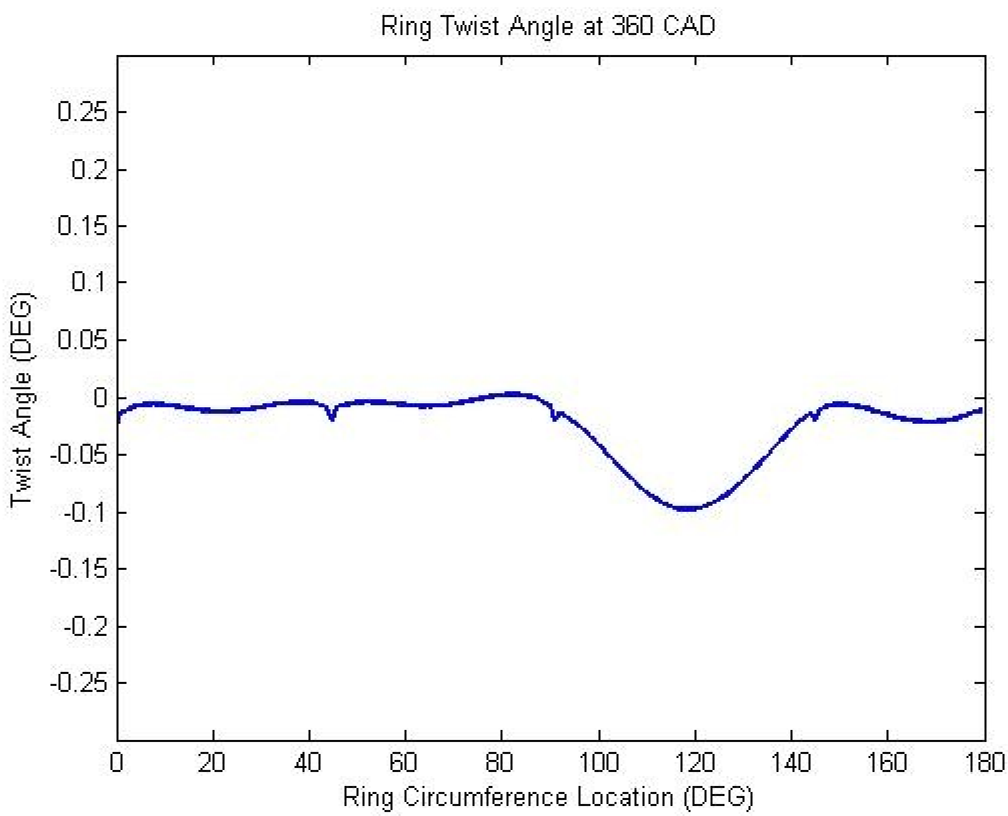

Figure 7-23 Ring twist angle at 360 CAD

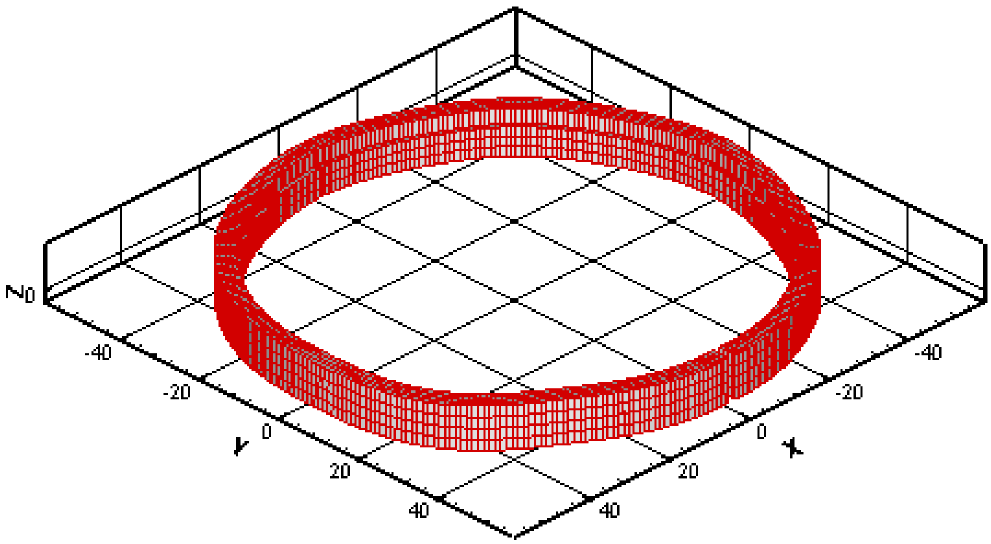

Figure 7-24 Deformed ring at 360 CAD

Table 7-8 lists the contact forces at the four potential contact points as shown in Figure 3-13.

Table 7-8 Contact forces in axial direction at 360 CAD

360 CAD (N)	Node 1	Node 2	Node 3	Node 4
0°	24.1	0.0	49.6	0.0
45°	52.8	0.0	90.0	0.0
90°	27.6	0.0	139.0	0.0
135°	1.5	0.0	157.6	0.0
180°	0.0	0.0	35.2	0.0

Figure 7-25 and Figure7-26 show the ring twist angle along the ring circumference for half ring and the deformed ring shape respectively at 450 CAD. The ring deformation in the axial direction is amplified by 10 times.

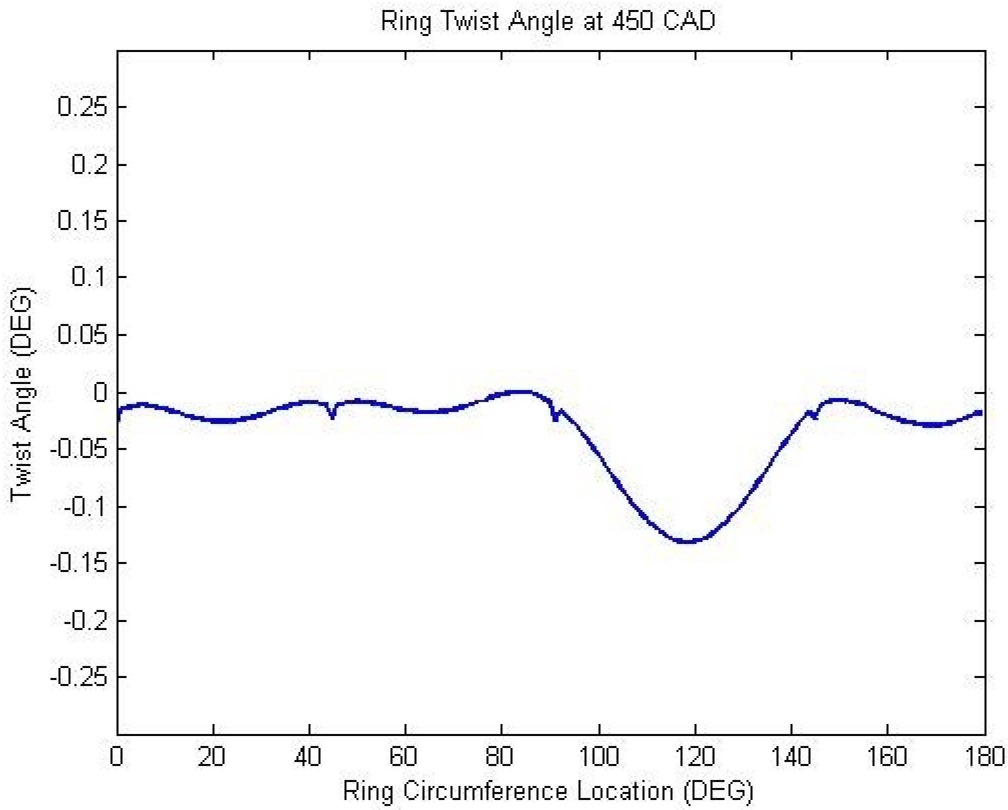

Figure 7-25 Ring twist angle at 450 CAD

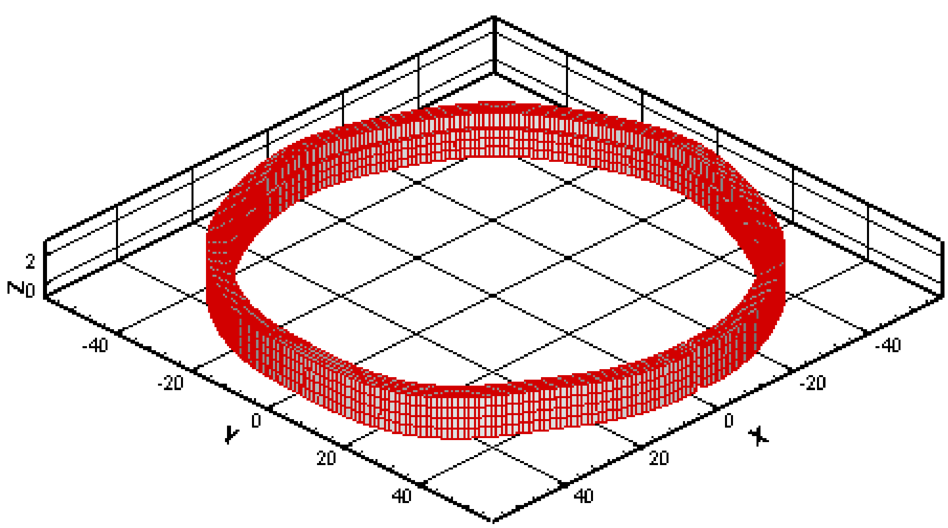

Figure7-26 Deformed ring at 450 CAD

Table 7-9 lists the contact forces at the four potential contact points as shown in Figure 3-13.

Table 7-9 Contact forces in axial direction at 450 CAD

450 CAD (N)	Node 1	Node 2	Node 3	Node 4
0°	26.2	0.0	70.7	0.0
45°	56.6	0.0	131.2	0.0
90°	33.3	0.0	186.4	0.0
135°	6.5	0.0	204.1	0.0
180°	0.0	0.0	46.4	0.0

Figure 7-27 and Figure 7-28 show the ring twist angle along the ring circumference for half ring and the deformed ring shape respectively at 540 CAD. The ring deformation in the axial direction is amplified by 10 times.

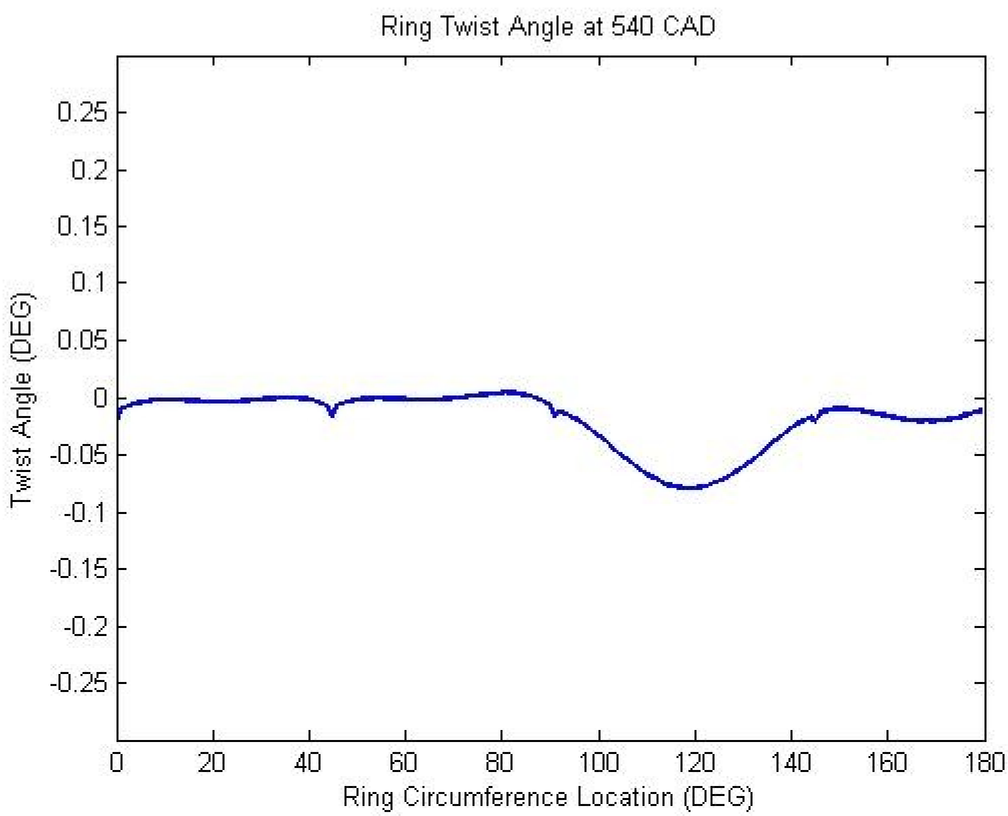

Figure 7-27 Ring twist angle at 540 CAD

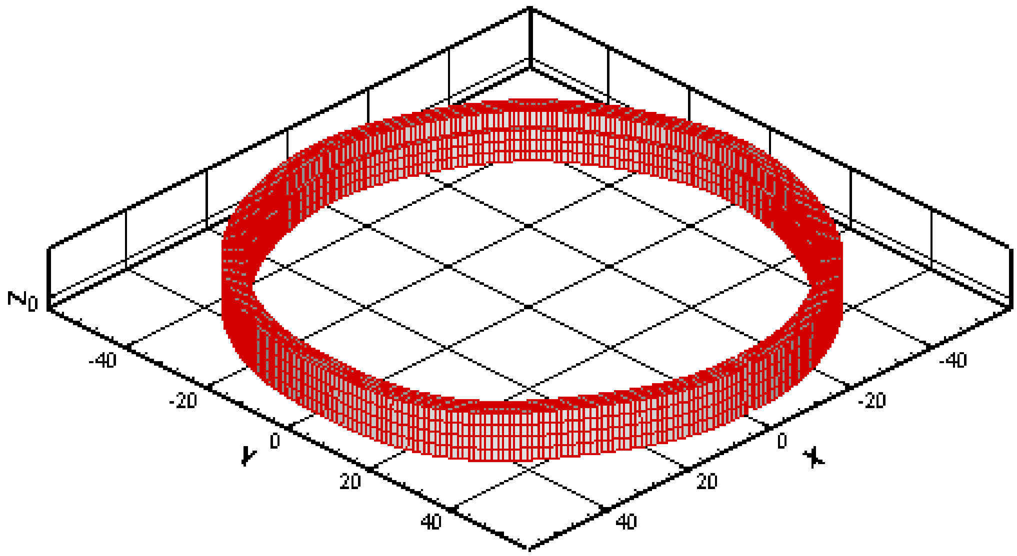

Figure 7-28 Deformed ring at 540 CAD

Table 7-10 lists the contact forces at the four potential contact points as shown in Figure 3-13.

Table 7-10 Contact forces in axial direction at 540 CAD

540 CAD (N)	Node 1	Node 2	Node 3	Node 4
0°	23.0	0.0	35.3	0.0
45°	50.7	0.0	63.3	0.0
90°	23.9	0.0	107.6	0.0
135°	0.0	0.0	125.6	0.0
180°	0.0	0.0	28.0	0.0

Figure 7-29 and Figure 7-30 show the ring twist angle along the ring circumference for half ring and the deformed ring shape respectively at 630 CAD. The ring deformation in the axial direction is amplified by 10 times.

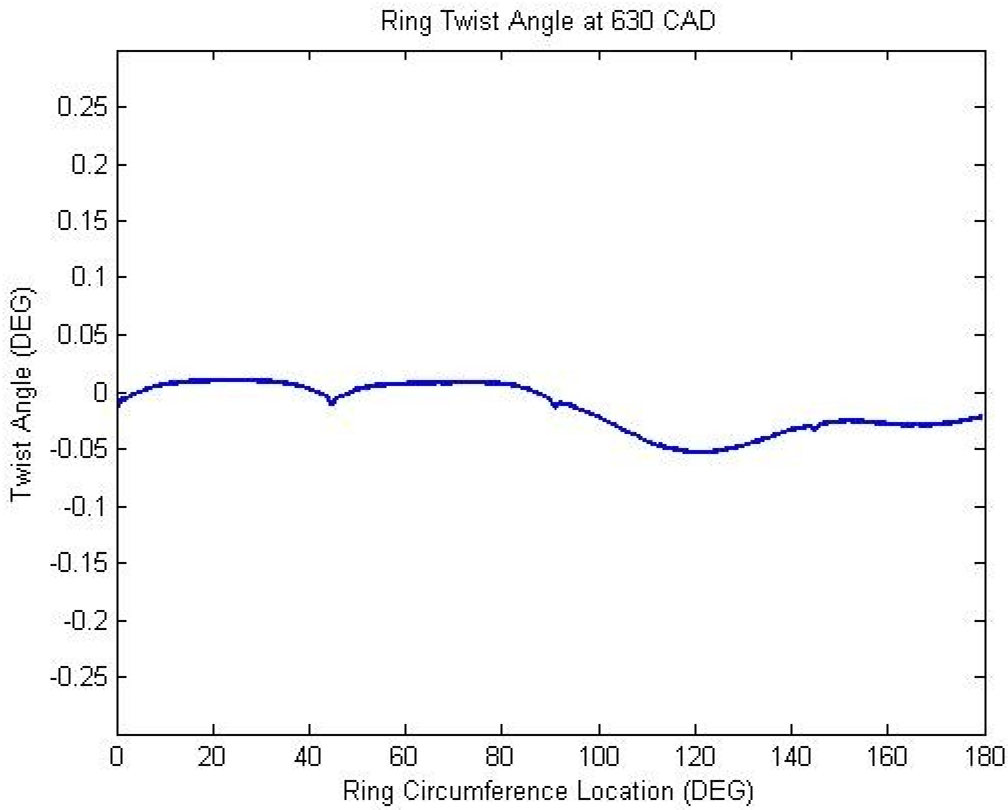

Figure 7-29 Ring twist angle at 630 CAD

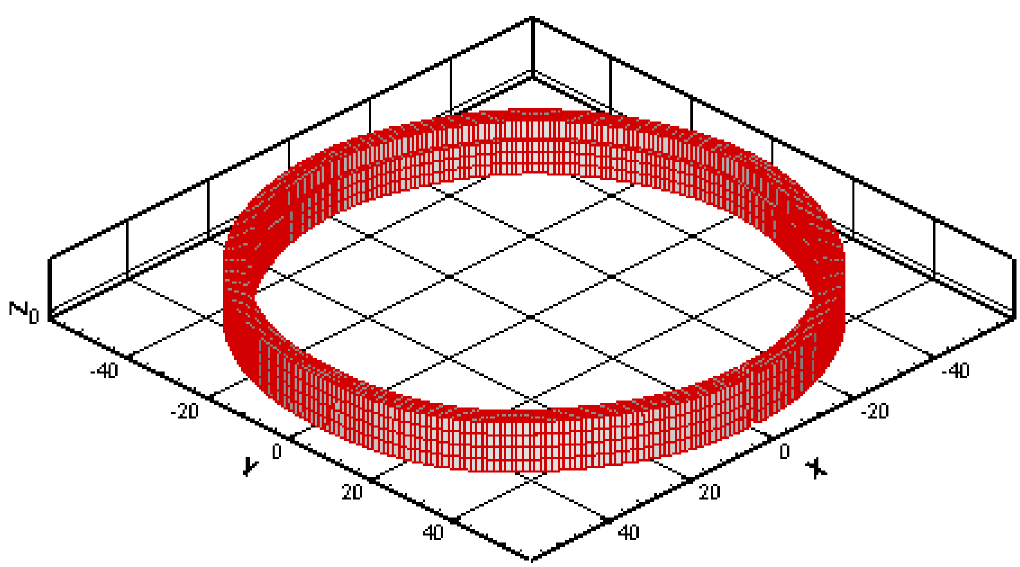

Figure 7-30 Deformed ring at 630 CAD

Table 7-11 lists the contact forces at the four potential contact points as shown in Figure 3-13.

Table 7-11 Contact forces in axial direction at 630 CAD

630 CAD (N)	Node 1	Node 2	Node 3	Node 4
0°	20.9	0.0	13.5	0.0
45°	40.7	0.0	20.6	0.0
90°	16.0	0.0	60.4	0.0
135°	0.0	0.0	73.3	0.0
180°	0.0	0.0	16.0	0.0

Figure 7-31 and Figure 7-32 show the ring twist angle along the ring circumference for half ring and the deformed ring shape respectively at 720 CAD. The ring deformation in the axial direction is amplified by 10 times.

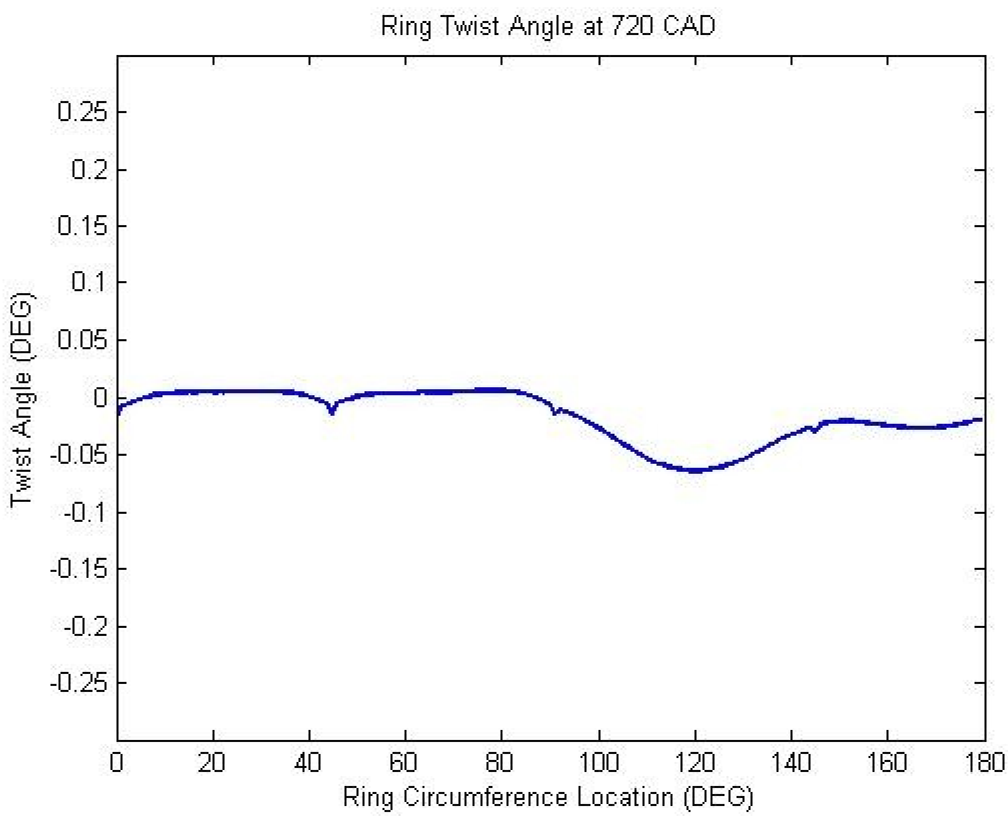

Figure 7-31 Ring twist angle at 720 CAD

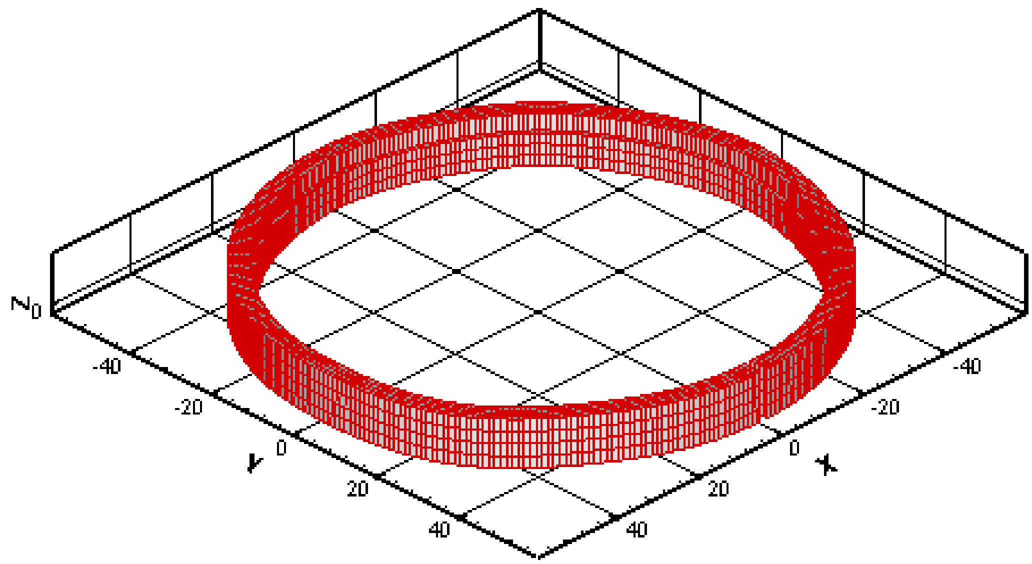

Figure 7-32 Deformed ring at 720 CAD

Table 7-12 lists the contact forces at the four potential contact points as shown in Figure 3-13.

Table 7-12 Contact forces in axial direction at 720 CAD

720 CAD (N)	Node 1	Node 2	Node 3	Node 4
0°	21.6	0.0	23.0	0.0
45°	48.2	0.0	38.9	0.0
90°	18.6	0.0	81.1	0.0
135°	0.0	0.0	95.5	0.0
180°	0.0	0.0	21.0	0.0

From Table 7-5 to Table 7-12, the contact force results clearly show that the ring stays bottom seated, since no contact forces are found at the ring top side at node 2 and node 4. However, the ring bottom side contact pattern varies from crank angle to crank angle depending on the pressure load and the inertial load.

In this study, the ring is constrained in 9 locations in both radial and axial directions. And due to the symmetric boundary condition about the ring back, the two parts of the ring have the same behavior regarding to the constraint forces, axial movement, twisting angle, etc. The radial and axial constraint forces over the engine cycle shown in Figure 7-15 for one half of the ring (5 locations) are plotted from Figure 7-33 to Figure 7-42. In these plots, the upper and lower nodes for the radial constraints refer to the nodes in Figure 3-8 and the nodes 1, 2, 3 and 4 for the axial constraints refer to those in Figure 3-13.

Figure 7-33 and Figure 7-34 show the radial constraint force and axial constraint force at the ring back (0 DEG) over a cycle respectively.

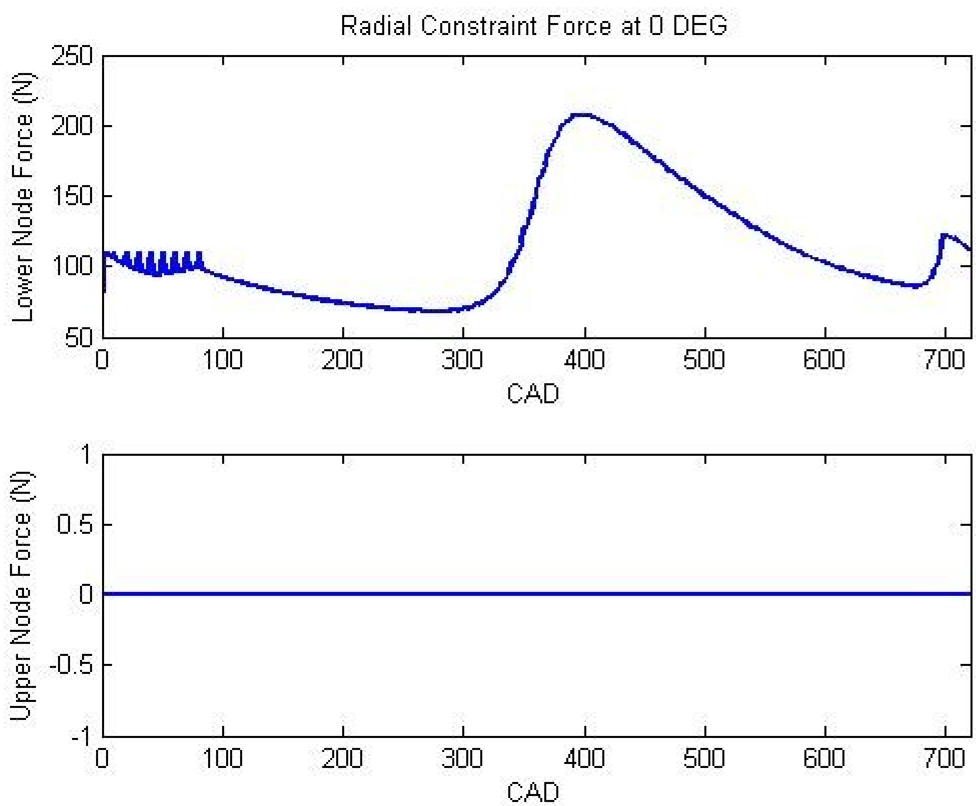

Figure 7-33 Radial Constraint Force at 0 DEG over a Cycle

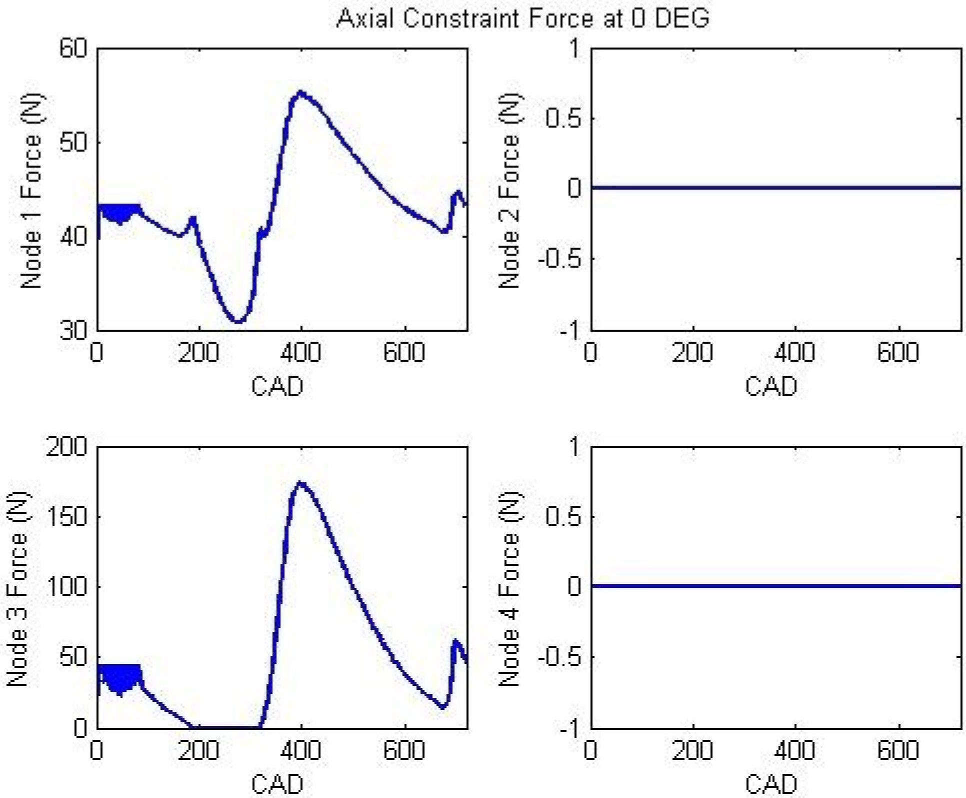

Figure 7-34 Axial Constraint Force at 0 DEG over a Cycle

Figure 7-35 and Figure 7-36 show the radial constraint force and axial constraint force at 45 DEG away from ring back over a cycle respectively.

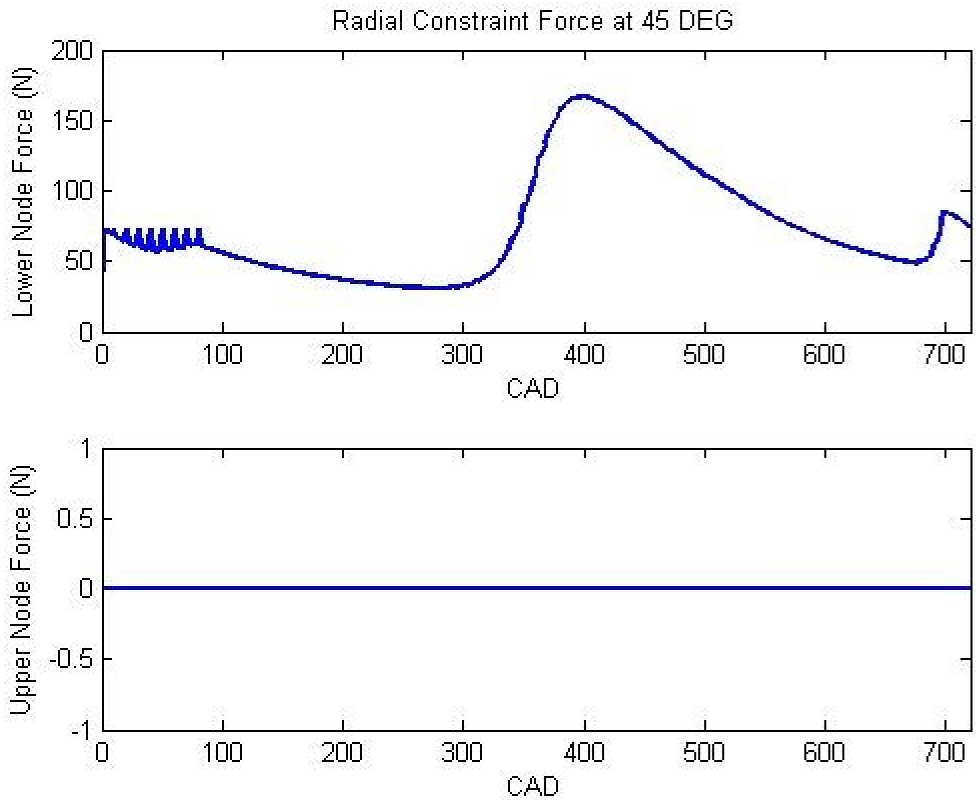

Figure 7-35 Radial Constraint Force at 45 DEG over a Cycle

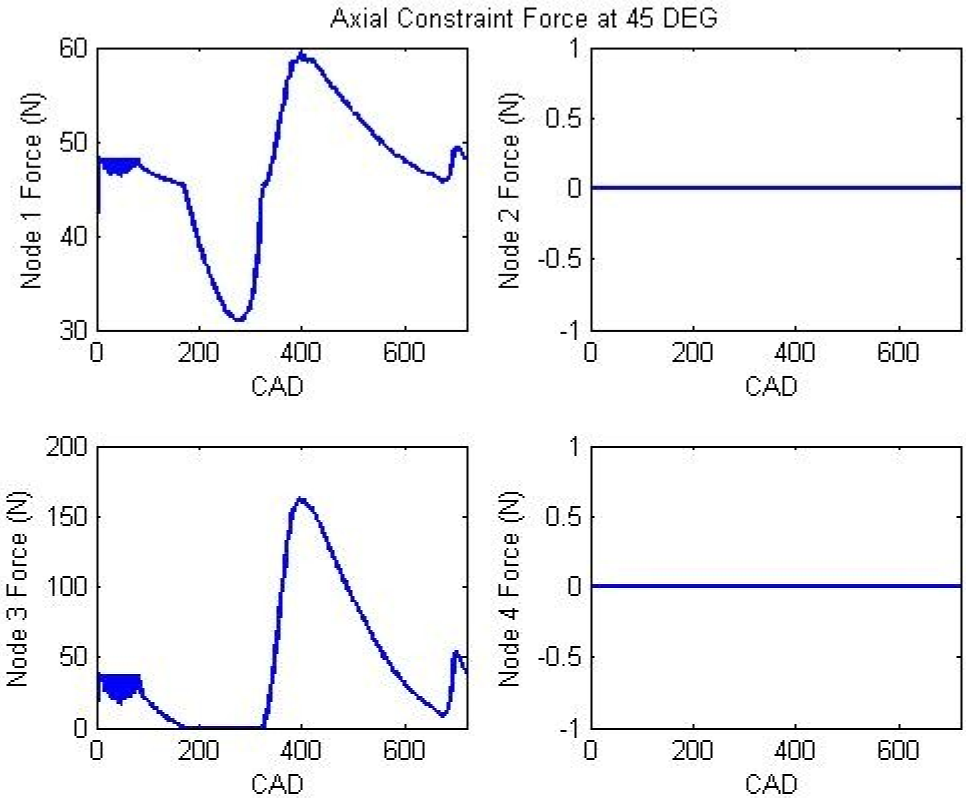

Figure 7-36 Axial Constraint Force at 45 DEG over a Cycle

Figure 7-37 and Figure 7-38 show the radial constraint force and axial constraint force at 90 DEG away from the ring back over a cycle respectively.

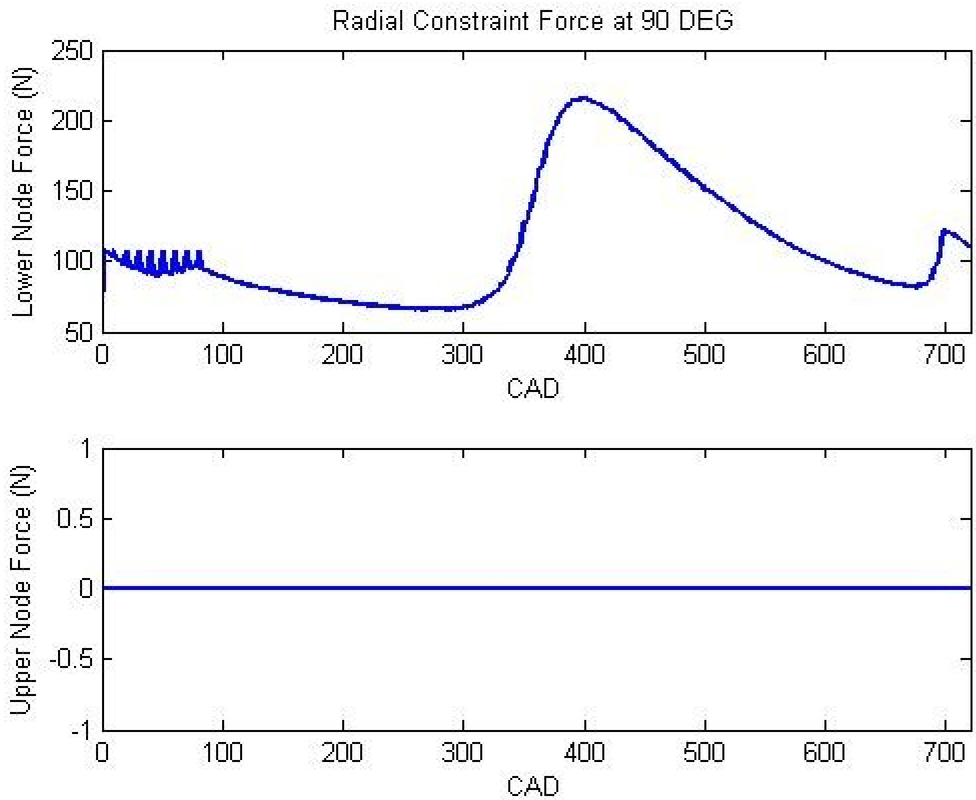

Figure 7-37 Radial Constraint Force at 90 DEG over a Cycle

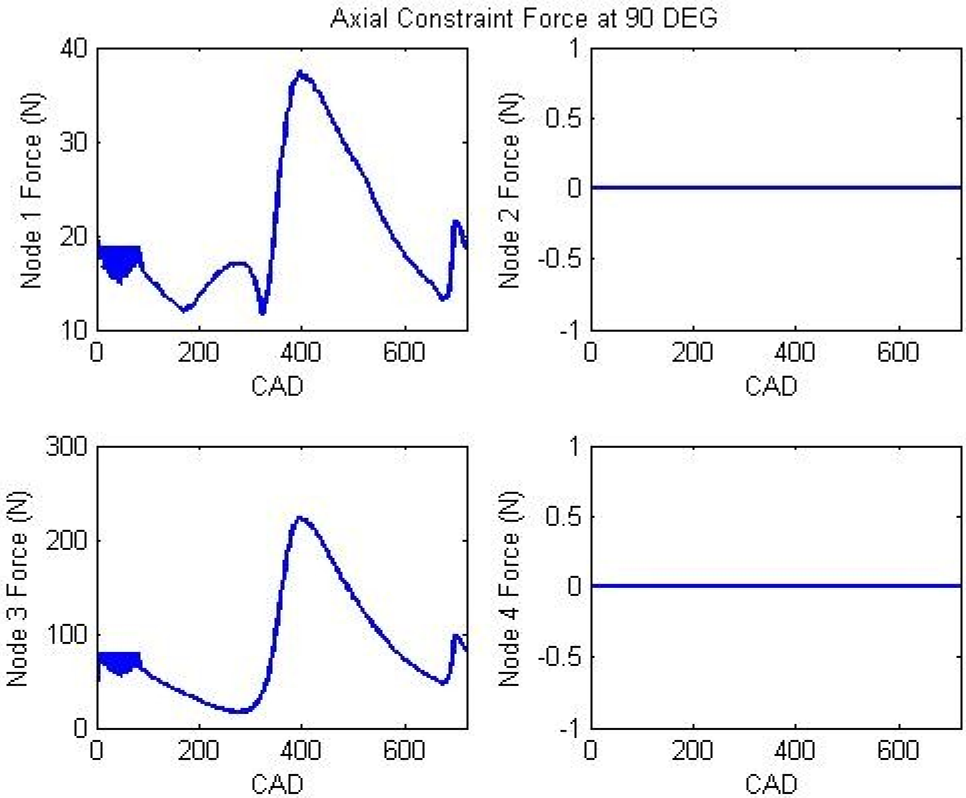

Figure 7-38 Axial Constraint Force at 90 DEG over a Cycle

Figure 7-39 and Figure 7-40 show the radial constraint force and axial constraint force at 135 DEG away from the ring back over a cycle respectively.

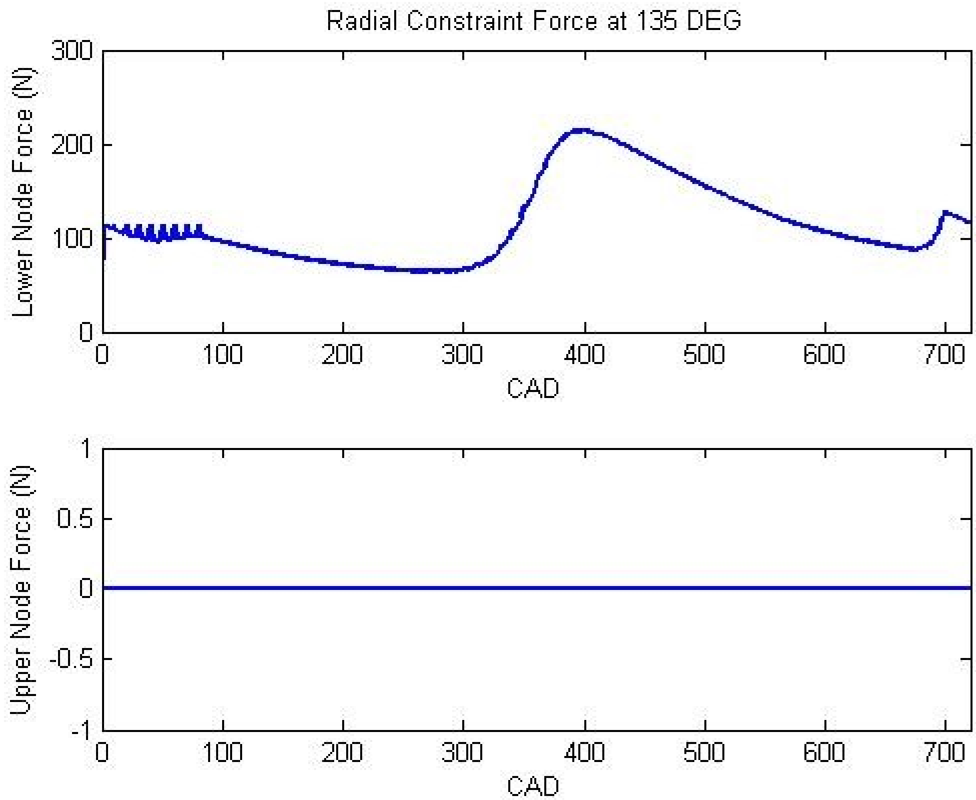

Figure 7-39 Radial Constraint Force at 135 DEG over a Cycle

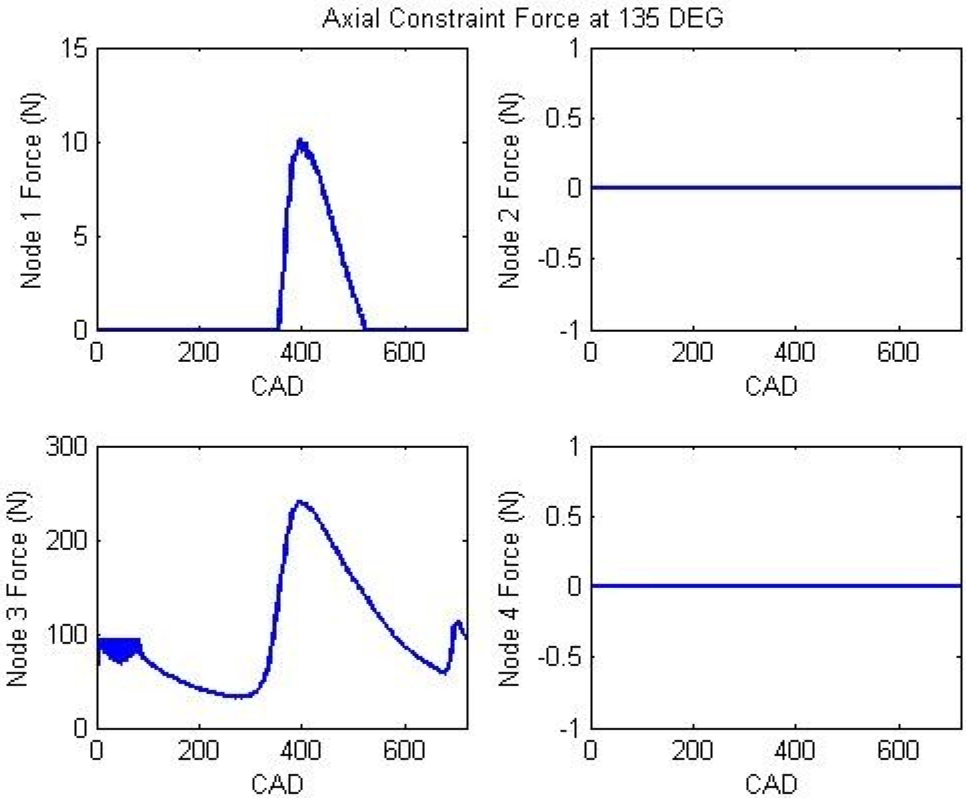

Figure 7-40 Axial Constraint Force at 135 DEG over a Cycle

Figure 7-41 and Figure 7-42 show the radial constraint force and axial constraint force at the ring end tip (near 180 DEG away from the ring back) over a cycle respectively.

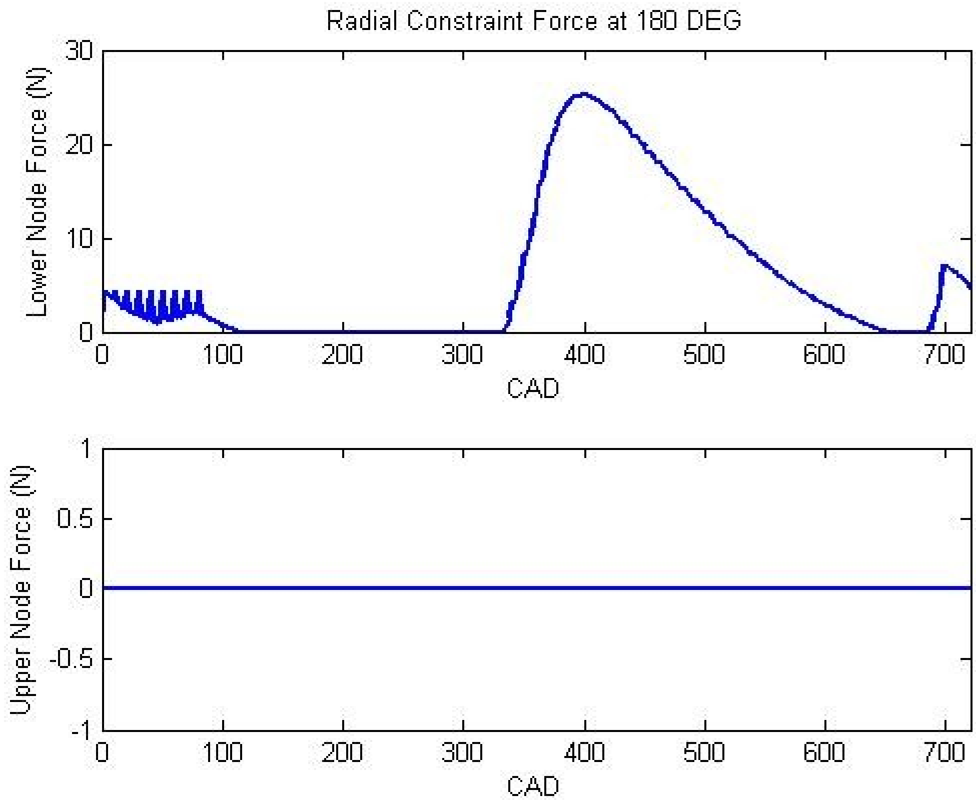

Figure 7-41 Radial Constraint Force at 180 DEG over a Cycle

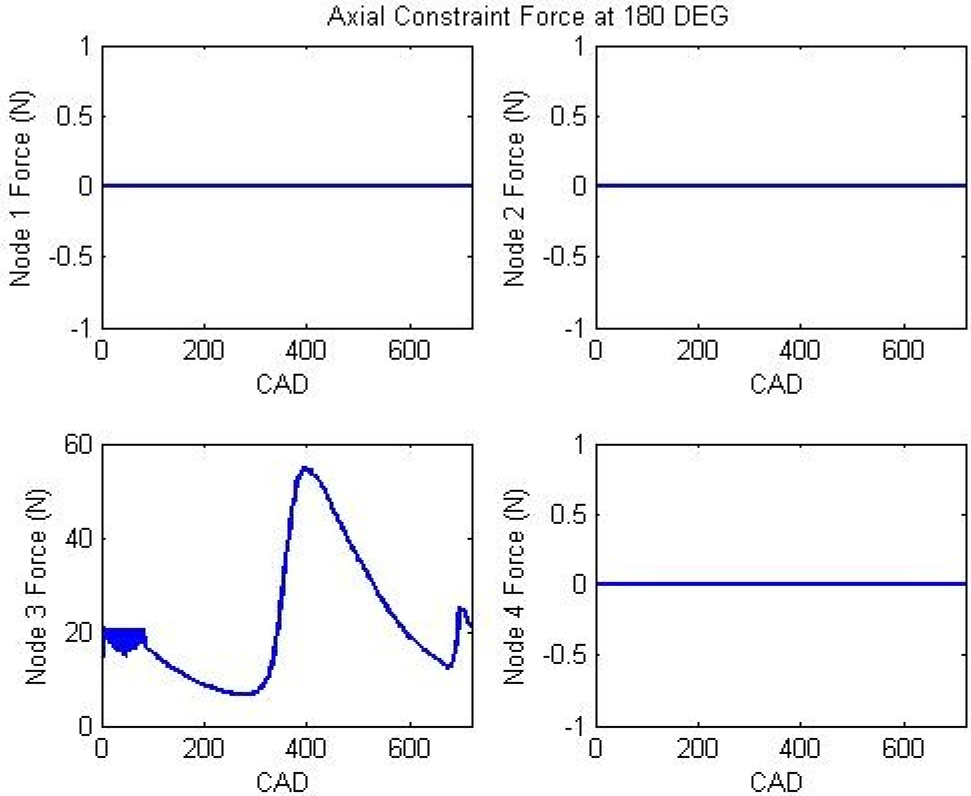

Figure 7-42 Axial Constraint Force at 180 DEG over a Cycle

The ring twist angle at each circumferential location along the ring circumference over a cycle is shown in Figure 7-43.

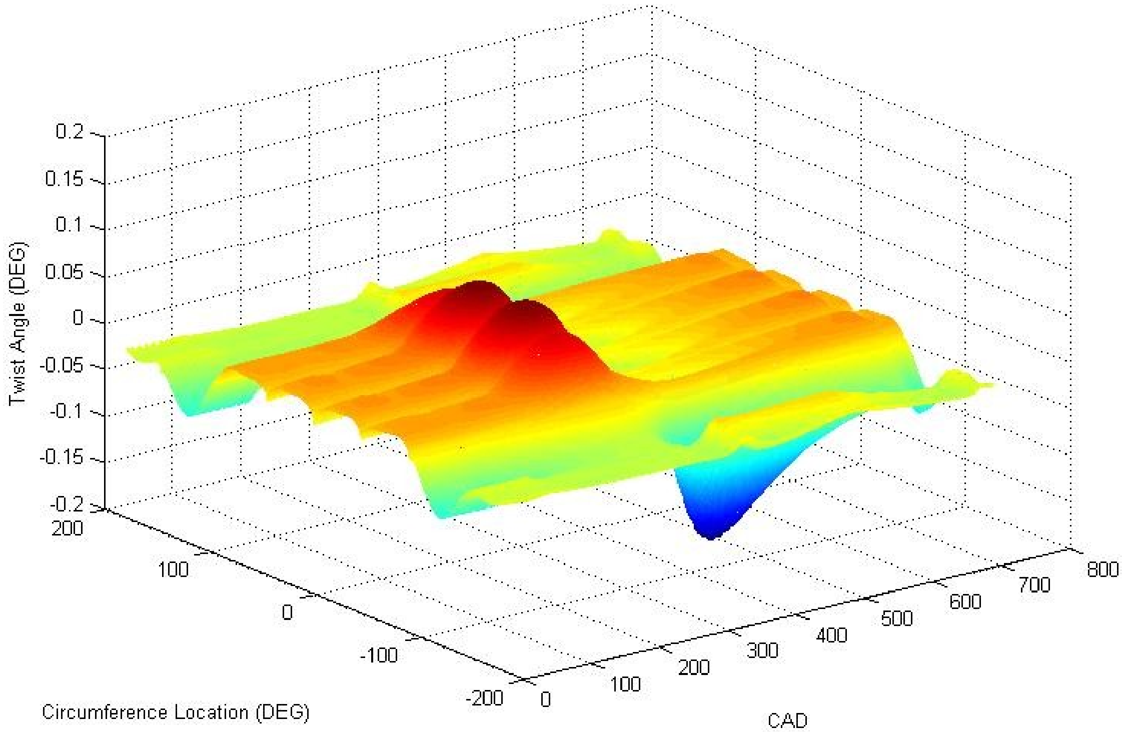

Figure 7-43 Ring Twist Angle over a Cycle

It is found from the ring twist angle plot that the ring twist varies from cross-section to cross-section and from crank angle to crank angle over the cycle. The ring undergoes the highest positive twist for the part less than ± 90° away from the ring back from about 250 CAD to 320 CAD due to the lower pressure load on the ring during that time. And the highest negative twist is found for the part about ± 120° away from the ring back from 360 CAD to 510 CAD.

Chapter 8 CONCLUSION AND RECOMMENDATION

8.1 Conclusion

In this dissertation, two major works have been accomplished: one is the further development of the cylinder-kit analysis tool, CASE-RING program; the other is the development of a three-dimensional piston ring model.

The ring lubrication model has been modified using the average Reynolds equation proposed by Patir and Cheng [69] considering the influence of surface roughness on hydrodynamic pressures. The contact between the ring face and the cylinder liner has been modified considering the cam-shape pressure distribution for the compression rings along their peripheries. This cam-shape profile in the ring face-cylinder liner interface can be obtained from the 3D ring analysis. Other minor modifications were also completed due to the request from the clients of CASE program.

A new 3D piston ring model has been developed. This model differs from the current 2D model as it calculates the variation in one more dimension: along the ring circumference. These variations include the ring axial movements, twist angles, contact pressure/force in the radial from the cylinder liner and axial directions from the groove sides. The model is used to evaluate the performance of the piston ring pack. Dynamic loadings, including the ring inertial load and the distributed pressure load, are also considered for dynamic analysis of the ring.

A numerical simulation was performed for a two-stroke engine piston top compression ring, predicting the piston ring contact and protrusion with the cylinder bridges and ports respectively. It was found the ring free shape is important in determining the ring contact pattern.

It was found that thermal load has significant influence on the ring performance. As the ring free shape with the temperature influence could change significantly, especially for the top compression ring, which is under the most severe thermal load condition. The thermal load influence needs to be considered in piston ring design.

Experiment measurements were conducted to verify the numerical model with two approaches. One approach was comparing the measured contact force with the predicted and good agreement was found. The other approach was using the light-tightness method and the separation gap near the ring end tips were verified by this experiment.

Ring twists and ring end gap sizes were found having a significant influence on the dynamics of the second compression ring, including the ring fluttering and the radial collapse. The key for eliminating the second ring fluttering and collapse is to hold the ring to stay bottom seated at around 90° before firing TDC when the ring inertial load changes its direction. As long as the second ring stays bottom seated at this specific location, the ring will not undergo the unstable motions.

The twist of the ring was also investigated using the 3D model and it was found for a scraper second ring, the ring twist varies from the ring back to the ring end tip. The variation in the ring twist can result in different pressure distribution boundary condition for the ring along the circumference as port of the ring may be exposed to the groove gas while some part may be exposed to the land gas.

8.2 Limitations and Recommendations

The limitations of this numerical model are identified in order to improve it in the future followed by the recommendations.

The 3D ring model is formulated from the minimum potential energy point of view and has been proven capable to predict the interactions between the ring and cylinder bore and the ring and piston groove sides. However, the boundary condition has been set such that the ring would not rotate in the circumferential direction. It works fine for the static condition and dynamic condition considering only the piston primary motion, which is along the cylinder axial direction. The piston second motions and the bore distortions, which are recognized as the cause of the ring rotation, have not been considered. In the future, these two influences need to be considered.

Another limitation of this model is that the gas pressures at each crank angle for the dynamic analysis are obtained from the 1D model and the gas pressure is identical around the ring circumference. In order to improve the accuracy of the model, the ring dynamics needs to be coupled with a 3D gas dynamic model in an iterative manner. This means not only the ring motion will be affected by the pressure distribution; the local gas pressures will also be influenced by the ring motion.

With the 3D interaction between the ring and cylinder bore, as well as between the ring and the groove sides, the friction and wear model can be improved accounting for the local tribological behavior. This needs to be accomplished in a progressive manner as the ring, groove, and cylinder liner need to be resurfaced after each wear stop. As it has been found from experiment, the piston rings wear show variation in the circumference direction. It will also be interesting to consider the 3D ring behavior in the lubrication oil film calculation since the oil film is significantly influenced by the ring twist. It will also be worth to take into consideration the different oil transportation mechanisms, including the oil throw-off, influence of engine blowback in addition to oil evaporation which is the only cause of oil consumption for the current model.

BIBLIOGRAPHY

BIBLIGRAPHY

[1] Panayi, A., Schock, H., Chui, B.-K., and Ejakov, M., 2006, "Parameterization and FEA Approach for the Assessment of Piston Characteristics," SAE International.

[2] 2007, "CASE-PISTON," Mid-Michigan Research.

[3] PLC, R., 2007, "PYSDYN."

[4] Wong, V. W., Tian, T., Lang, H., Ryan, J. P., Sekiya, Y., Kobayashi, Y., and Aoyama, S., 1994, "A Numerical Model of Piston Secondary Motion and Piston Slap in Partially Flooded Elastohydrodynamic Skirt Lubrication," SAE International.

[5] Keribar, R., and Dursunkaya, Z., 1992, "A Comprehensive Model of Piston Skirt Lubrication," SAE International.

[6] Kim, K.-s., Shah, P., Takiguchi, M., and Aoki, S., 2009, "Part 3: A Study of Friction and Lubrication Behavior for Gasoline Piston Skirt Profile Concepts," SAE International.

[7] Malagi, R. R., Kurbet, S. N., and Gowrishenkar, N., 2009, "Finite Element Study on Piston Assembly Dynamics Emphasis with Lubrication," The Automotive Research Association of India.

[8] Kageyama, H., Machida, S., Shimanuki, S., Suzuki, T., Ochiai, Y., and Oda, T., 2000, "Study of the Contact Pressures and Deformations of Piston Skirt in Gasoline Engine," SAE International.

[9] Patel, P., Mourelatos, Z. P., and Shah, P., 2007, "A Comprehensive Method for Piston Secondary Dynamics and Piston-Bore Contact," SAE International.

[10] Taylor, R. I., and Evans, P. G., 2004, "In-situ piston measurements," Proceedings of the Institution of Mechanical Engineers, Part J: Journal of Engineering Tribology, 218(3), pp. 185-200.

[11] De Petris, C., Giglio, V., and Police, G., 1994, "A Mathematical Model for the Calculation of Blow-by Flow and Oil Consumption Depending on Ring Pack Dynamic Part I: Gas Flows, Oil Scraping and Ring Pack Dynamic," SAE International.

[12] Dursunkaya, Z., Keribar, R., and Richardson, D. E., 1993, "Experimental and Numerical Investigation of Inter-Ring Gas Pressures and Blowby in a Diesel Engine," SAE International.

[13] Tian, T., Noordzij, L. B., Wong, V. W., and Heywood, J. B., 1998, "Modeling Piston-Ring Dynamics, Blowby, and Ring-Twist Effects," Journal of Engineering for Gas Turbines and Power, 120(4), pp. 843-854.

[14] Tian, T., 2002, "Dynamic behaviours of piston rings and their practical impact. Part 1: Ring flutter and ring collapse and their effects on gas flow and oil transport," Proceedings of the Institution of Mechanical Engineers, Part J: Journal of Engineering Tribology, 216(4), pp. 209-228.

[15] Tian, T., 2002, "Dynamic behaviours of piston rings and their practical impact. Part 2: Oil transport, friction and wear of ring/liner interface and the effects of piston and ring dynamics," Proceedings of the Institution of Mechanical Engineers, Part J: Journal of Engineering Tribology, 216(4), pp. 229-248.

[16] 2007, "CASE-RING," Mid-Michigan Research.

[17] Ejakov, M. A., Schock, H. J., Brombolich, L. J., Carlstrom, C. M. and Williams, R. L., "Simulation Analysis of Inter-Ring Gas Pressure and Ring Dynamics and Their Effect on Blow-by," Proc. 1997 Fall Technical Conference, ASME.

[18] Ejakov, M. A., Schock, H. J., and Brombolich, L. J., 1998, "Modeling of Ring Twist For an IC Engine," SAE International.

[19] Baker, C., Rahmani, R., Karagiannis, I., Theodossiades, S., Rahnejat, H., and Frendt, A., 2014, "Effect of Compression Ring Elastodynamics Behaviour upon Blowby and Power Loss," SAE International.

[20] Koszalka, G., and Niewczas, A., 2006, "The Influence of Compression Ring Clearances on the Blowby in a Diesel Engine," SAE International.

[21] Malagi, R. R., 2012, "Estimation of Blowby in Multi-cylinder Diesel Engine Using Finite Element Approach," SAE International.

[22] Liu, L., Tian, T., and Rabuté, R., 2003, "Development and Applications of an Analytical Tool for Piston Ring Design," SAE International.

[23] Liu, L., and Tian, T., 2005, "Implementation and Improvements of a Flow Continuity Algorithm in Modeling Ring/Liner Lubrication," SAE International.

[24] Liu, L., and Tian, T., 2005, "Modeling Piston Ring-Pack Lubrication With Consideration of Ring Structural Response," SAE International.

[25] Tomanik, E., and Bruno, R., 2012, "Calculation of Piston Ring Radial Pressure Distribution from its Measured Free Shape," SAE International.

[26] Tomanik, E., Sobrinho, R. M. S., and Zecchinelli, R., 1993, "Influence Of Top Ring End Gap Types At Blow-By Of Internal Combustion Engines," SAE International.

[27] Tomanik, E., 1996, "Piston Ring Conformability in a Distorted Bore," SAE International.

[28] Tomanik, E., and Nigro, F. E. B., 2001, "Piston Ring Pack and Cylinder Wear Modelling," SAE International.

[29] Tomanik, E., Zabeu, C. B., and de Almeida, G. M., 2003, "Abnormal Wear on Piston Top Groove," SAE International.

[30] Tomanik, E., 2009, "Improved Criterion for Ring Conformability Under Realistic Bore Deformation," SAE International.

[31] Ma, J., Ryan, T. W., Winter, J., and Dixon, R., 1996, "The Piston Ring Shape and Its Effects on Engine Performance," SAE International.

[32] Sun, D. C., 1991, "A Thermal Elastica Theory of Piston-Ring and Cylinder-Bore Contact," Journal of Applied Mechanics, 58(1), pp. 141-153.

[33] Tejada, A., and Padial, M., 1995, "Piston Ring Technology for Oil Consumption Blow-by Reduction in Otto Engine," SAE International.

[34] Chui, B.-K., 2001, "Computational analysis of piston ring wear and oil consumption for an internal combustion engine,"M. s., Michigan State University. Dept. of Mechanical Engineering.

[35] Chui, B.-K., 2005, "Elastohydrodynamic modeling and measurement of cylinder-kit assembly tribological performance,"Ph. D., Michigan State University. Dept. of Mechanical Engineering.

[36] De Petris, C., Giglio, V., and Police, G., 1997, "A Mathematical Model of the Evaporation of the Oil Film Deposed on the Cylinder Surface of IC Engines," SAE International.

[37] Dowson, D., Ruddy, B. L., and Economou, P. N., 1983, "The Elastohydrodynamic Lubrication of Piston Rings," Proceedings of the Royal Society of London. A. Mathematical and Physical Sciences, 386(1791), pp. 409-430.

[38] Picard, M., Baelden, C., Tian, T., Nishino, T., Arai, E., and Hidaka, H., 2014, "Oil Transport Cycle Model for Rotary Engine Oil Seals," SAE Int. J. Engines, 7(3).

[39] Richardson, D. E., and Borman, G. L., 1992, "Theoretical and Experimental Investigations of Oil Films for Application to Piston Ring Lubrication," SAE International.

[40] Schneider, E. W., Blossfeld, D. H., Lechman, D. C., Hill, R. F., Reising, R. F., and Brevick, J. E., 1993, "Effect of Cylinder Bore Out-of-Roundness on Piston Ring Rotation and Engine Oil Consumption," SAE International.

[41] Richardson, D. E., 2000, "Review of Power Cylinder Friction for Diesel Engines," Journal of Engineering for Gas Turbines and Power, 122(4), pp. 506-519.

[42] Heywood, J. B., 1988, Internal combustion engine fundamentals, McGraw-Hill, New York.

[43] Urabe, M., Takakura, T., Metoki, S., Yanagisawa, M., and Murata, H., 2014, "Mechanism of and Fuel Efficiency Improvement by Dimple Texturing on Liner Surface for Reduction of Friction between Piston Rings and Cylinder Bore," SAE International.

[44] Bird, L. E., and Gartside, R. M., 2002, "Measurement of Bore Distortion in a Firing Engine," SAE International.

[45] Ha, K.-P., Kim, J.-S., Cho, M.-R., and Oh, D. Y., 2002, "Development of Piston Friction Force Measurement System," SAE International.

[46] Law, T., MacMillan, D., Shayler, P. J., Kirk, G., Pegg, I., and Stark, R., 2012, "A New Floating-Liner Test Rig Design to Investigate Factors Influencing Piston-Liner Friction," SAE International.

[47] Liao, K., Chen, H., and Tian, T., 2012, "The Study of Friction between Piston Ring and Different Cylinder Liners using Floating Liner Engine - Part 1," SAE International.

[48] Nakayama, K., Tamaki, S., Miki, H., and Takiguchi, M., 2000, "The Effect of Crankshaft Offset on Piston Friction Force in a Gasoline Engine," SAE International.

[49] O'Rourke, B., Stanglmaier, R., and Radford, D., 2006, "Development of a Floating-Liner Engine for Improving the Mechanical Efficiency of High Performance Engines," SAE International.

[50] Koch, F., Geiger, U., and Hermsen, F.-G., 1996, "PIFFO - Piston Friction Force Measurements During Engine Operation," SAE International.

[51] Cheng, C., Wineland, R., Kharazmi, A., Schock, H., and Brombolich, L., "Three Dimensional Piston Ring-Cylinder Bore Contact Modeling," Proc. ASME ICEF 2014, ASME.

[52] Chan, S. K., and Tuba, I. S., 1971, "A finite element method for contact problems of solid bodies—Part I. Theory and validation," International Journal of Mechanical Sciences, 13(7), pp. 615-625.

[53] Belegundu, A. D., and Chandrupatla, T. R., 2011, Optimization concepts and applications in engineering, Cambridge University Press, New York.

[54] Mierbach, A., Dučk, G. E., and Newman, B. A., 1983, Heat Flow Through Piston Rings and Its Influence on Shape, Society of Automotive Engineers.

[55] Fish, J., and Belytschko, T., 2007, "A first course in finite elements," John Wiley & Sons Ltd.,, Chichester, England ; Hoboken, NJ, pp. xiv, 319 p., 318 p. of plates.

[56] Cook, R. D., 1994, Finite Element Modeling for Stress Analysis, John Wiley \\& Sons, Inc.

[57] Akalin, O., and Newaz, G. M., 1999, "Piston Ring-Cylinder Bore Friction Modeling in Mixed Lubrication Regime: Part I—Analytical Results," Journal of Tribology, 123(1), pp. 211-218.

[58] Arcoumanis, C., Ostovar, P., and Mortier, R., 1997, "Mixed Lubrication Modelling of Newtonian and Shear Thinning Liquids in a Piston-Ring Configuration," SAE International.

[59] Dearlove, J., and Cheng, W. K., 1995, "Simultaneous Piston Ring Friction and Oil Film Thickness Measurements in a Reciprocating Test Rig," SAE International.

[60] Madden, D., Kim, K., and Takiguchi, M., 2006, "Part 1: Piston Friction and Noise Study of Three Different Piston Architectures for an Automotive Gasoline Engine," SAE International.

[61] Mufti, R. A., and Priest, M., 2004, "Experimental Evaluation of Piston-Assembly Friction Under Motored and Fired Conditions in a Gasoline Engine," Journal of Tribology, 127(4), pp. 826-836.

[62] Sethu, C., Leustek, M. E., Bohac, S. V., Filipi, Z. S., and Assanis, D. N., 2007, "An Investigation in Measuring Crank Angle Resolved In-Cylinder Engine Friction Using Instantaneous IMEP Method," SAE International.

[63] Wakuri, Y., Hamatake, T., Soejima, M., and Kitahara, T., 1992, "Piston ring friction in internal combustion engines," Tribology International, 25(5), pp. 299-308.

[64] Schwaderlapp, M., Koch, D. I. F., and Dohmen, D. I. J., 2000, "Friction Reduction - the Engine's Mechanical Contribution to Saving Fuel," Society of Automotive Engineers of Korea.

[65] Schwaderlapp, M., Plettenberg, M., Tomazic, D., Schuermann, G., Ring, F., and Bowyer, S., 2014, "The Contribution of Engine Mechanics to Improved Fuel Economy," SAE Int. J. Engines, 7(3).

[66] Greenwood, J. A., and Williamson, J. B. P., 1966, "Contact of Nominally Flat Surfaces," Proceedings of the Royal Society of London. Series A. Mathematical and Physical Sciences, 295(1442), pp. 300-319.

[67] Greenwood, J. A., and Tripp, J. H., 1970, "The Contact of Two Nominally Flat Rough Surfaces," Proceedings of the Institution of Mechanical Engineers, 185(1), pp. 625-633.

[68] Hu, Y., Cheng, H. S., Arai, T., Kobayashi, Y., and Aoyama, S., 1994, "Numerical Simulation of Piston Ring in Mixed Lubrication—A Nonaxisymmetrical Analysis," Journal of Tribology, 116(3), pp. 470-478.

[69] Patir, N., and Cheng, H. S., 1978, "An Average Flow Model for Determining Effects of Three-Dimensional Roughness on Partial Hydrodynamic Lubrication," Journal of Tribology, 100(1), pp. 12-17.

[70] Chung, Y., Schock, H. J., and Brombolich, L. J., 1993, "Fire Ring Wear Analysis for a Piston Engine," SAE International.

[71] Gangopadhyay, A., 2000, "Development of a Piston Ring-Cylinder Bore Wear Model," SAE International.

[72] Mukras, S., Kim, N. H., Sawyer, W. G., Jackson, D. B., and Bergquist, L. W., 2009, "Numerical integration schemes and parallel computation for wear prediction using finite element method," Wear, 266(7–8), pp. 822-831.

[73] Põdra, P., and Andersson, S., 1997, "Wear simulation with the Winkler surface model," Wear, 207(1–2), pp. 79-85.

[74] Põdra, P., and Andersson, S., 1999, "Simulating sliding wear with finite element method," Tribology International, 32(2), pp. 71-81.

[75] Schneider, E. W., and Blossfeld, D. H., 2004, "Effect of Break-In and Operating Conditions on Piston Ring and Cylinder Bore Wear in Spark-Ignition Engines," SAE International.

[76] Tian, T., Rabute, R., Wong, V. W., and Heywood, J. B., 1997, "Effects of Piston-Ring Dynamics on Ring/Groove Wear and Oil Consumption in a Diesel Engine," SAE International.

[77] Archard, J. F., 1953, "Contact and Rubbing of Flat Surfaces," Journal of Applied Physics, 24(8), pp. 981-988.

[78] Poort, M., Cheng, C., Richardson, D., and Schock, H., "Piston Ring and Groove Side Wear Analysis for Diesel Engines," Proc. ASME ICEF 2014, ASME.

[79] Cheng, C., Richardson, D., and Schock, H., "The Dynamics of Second Ring Flutter and Collapse in Modern Diesel Engines," Proc. ASME ICEF 2014, ASME.